



저작자표시-비영리-변경금지 2.0 대한민국

이용자는 아래의 조건을 따르는 경우에 한하여 자유롭게

- 이 저작물을 복제, 배포, 전송, 전시, 공연 및 방송할 수 있습니다.

다음과 같은 조건을 따라야 합니다:



저작자표시. 귀하는 원저작자를 표시하여야 합니다.



비영리. 귀하는 이 저작물을 영리 목적으로 이용할 수 없습니다.



변경금지. 귀하는 이 저작물을 개작, 변형 또는 가공할 수 없습니다.

- 귀하는, 이 저작물의 재이용이나 배포의 경우, 이 저작물에 적용된 이용허락조건을 명확하게 나타내어야 합니다.
- 저작권자로부터 별도의 허가를 받으면 이러한 조건들은 적용되지 않습니다.

저작권법에 따른 이용자의 권리는 위의 내용에 의하여 영향을 받지 않습니다.

이것은 [이용허락규약\(Legal Code\)](#)을 이해하기 쉽게 요약한 것입니다.

[Disclaimer](#)

이학박사 학위논문

I and II. Evaluation of the atmospheric deposition
using dissolved components in rainwater and
mercury in Antarctic snow

III. Provenance and environmental change recorded
in authigenic beryllium and detrital hafnium isotopes
in marine sediment of the Bering Sea

I, II. 강수 내 용존 성분 및 남극 눈에 포함된 수은 농도
연구를 통한 대기 침적 평가

III. 자생성분 내 베릴륨 및 쇄설성분 내 하프늄 동위원소 비를
이용한 베링해 해저 퇴적물의 기원 및 퇴적 환경 변화 연구

2013 년 2 월

서울대학교 대학원

지구환경과학부

한 영 철

**I and II. Evaluation of the atmospheric deposition
using dissolved components in rainwater and
mercury in Antarctic snow**

**III. Provenance and environmental change recorded
in authigenic beryllium and detrital hafnium
isotopes in marine sediment of the Bering Sea**

Yeongcheol Han

**A dissertation submitted to in partial fulfillment of the
requirements for the degree of doctor of philosophy**

February 2013

**School of Earth and Environmental Sciences
Seoul National University**

I and II. Evaluation of the atmospheric deposition
using dissolved components in rainwater and
mercury in Antarctic snow

III. Provenance and environmental change recorded
in authigenic beryllium and detrital hafnium isotopes
in marine sediment of the Bering Sea

지도 교수 허 영 숙

이 논문을 이학박사 학위논문으로 제출함

2012 년 12 월

서울대학교 대학원

지구환경과학부

한 영 철

한영철의 이학박사 학위논문을 인준함

2013 년 2 월

위 원 장 _____ (인)

부위원장 _____ (인)

위 원 _____ (인)

위 원 _____ (인)

위 원 _____ (인)

ABSTRACT

This thesis views precipitation as a means that the Earth employs to record its change, because the precipitates reflect environmental conditions at the time of formation. It consists of six chapters that deal with compositions of precipitates forming in the atmosphere and ocean.

In Chapters 2 and 3, the composition of rainwater is investigated with a major focus on local conditions that should be considered when monitoring the rainwater composition. The studies were conducted at two sites located on remote and rural islands in Korea – the Baengnyeongdo Atmospheric Research Center (BARC, Chapter 2) and Gosan Station (Chapter 3). In BARC, temporal formation of a rain shadow depending on the wind conditions and natural and artificial topography resulted in meter-scale spatial variations in the rainwater composition. In Gosan Station, local aerosols were generated by strong winds from the cultivated ground of the island and introduced into the rain collector. These observations stressed that the contribution of the local factors to the rainwater composition should be carefully interpreted, especially at windy sites chosen for monitoring the regional background atmosphere.

In Chapters 4, 5 and 6, the total mercury concentration (Hg_T) is determined from surface snow (Chapter 4) and snow pits (Chapters 5 and 6) on the Antarctic Plateau to contribute to the understanding of the mercury

dynamics in inland Antarctica and the global mercury cycle. In spite of an active exchange of mercury between the atmosphere and surface snow during the austral sunlit period, supported by spatio-temporal variability of Hg_T in surface snow and emerging evidences from the atmospheric observation, only a small amount of mercury (a few $pg\ g^{-1}$) is sequestered in the Antarctic snowpack. The amplitude of seasonal and interannual variation in mercury sequestration appears to be controlled by the poleward transport of sea-salt.

In Chapter 7, authigenic $^{10}Be/{}^9Be$ ratio and detrital $^{176}Hf/{}^{177}Hf$ are determined from marine sediments on the Bowers Ridge in the Bering Sea spanning 32 – 40 ka. The former reflects the deep seawater composition at the time of deposition and the latter is a tracer for source provenance of the detrital particles. The $^{10}Be/{}^9Be$ about a half of the current ratio indicates either high biological productivity or increased riverine influx of 9Be and detrital particles at that time. The peak of $^{10}Be/{}^9Be$ at ~32 ka might be associated with the reduction of geomagnetic field and consequent enhancement of ^{10}Be production.

Keywords: dissolved ions, DOC, $\delta^{13}C$, Hg, $^{176}Hf/{}^{177}Hf$, $^{10}Be/{}^9Be$

Student Number: 2008-30823

Thesis supervisor: Prof. Youngsook Huh

Table of Contents

Abstract	i
Table of contents.....	iii
List of Figures	ix
List of Tables.....	xiii
Chapter 1. Introduction: Atmospheric and oceanic precipitation chronicling Earth's changes	xv
1.1. Atmospheric precipitation.....	xvii
1.2. Precipitation in seawater.....	xxii
Part I.	
Chapter 2. Rain sampler design and sampling strategy for major ions and dissolved organic carbon	1
2.1. Introduction	2
2.2. Rain sampler design	3
2.2.1. Bulk sampling	3
2.2.1.1. Dissolved major and trace elements	4
2.2.1.2. Dissolved organic carbon	5
2.2.2. Wet-only sampling.....	5
2.3. Preliminary study of meter-scale spatial variability of rainwater composition on the Seoul National University campus and at Gosan Station.....	6

2.4. Case study at BARC.....	7
2.4.1. Sampling location, collection and analysis	7
2.4.2. Meteorological information and air mass back trajectory analysis	9
2.4.3. Results.....	10
2.4.4. Discussion	12
2.4.4.1. Identification of major sources for rainwater constituents.....	12
2.4.4.2. Meter-scale spatial variation in the rainwater composition..	16
2.4.4.3. Contributions of bulk sampling to monitoring the rainwater composition	17
2.5. Summary	18
2.6. References	19

**Chapter 3. Assessing the impact of locally produced aerosol on the
rainwater composition at Gosan background site in East Asia
..... 34**

Abstract	35
3.1. Introduction	36
3.2. Method	39
3.2.1. Study area.....	39
3.2.2. Rainwater chemistry data base and meteorological data.....	39
3.2.3. Simultaneous rain sampling	40
3.3. Results and discussion.....	41
3.3.1. NO ₃ /Na ratio as a proxy for local influence	42

3.3.2. Meter-scale spatial variability of rainwater composition	44
3.3.3. Comparison to aerosol composition data	46
3.3.4. Significance of the local influence on the wet deposition flux ...	47
3.4. Conclusion.....	49
3.5. References	50

Part II.

Chapter 4. Quantification of total mercury in Antarctic surface

snow using ICP-SF-MS: spatial variation from the coast to

Dome Fuji 66

Abstract	67
4.1. Introduction	68
4.2. Experimental	70
4.3. Results and discussion.....	72
4.3.1. Mercury loss from dilute standard solutions	72
4.3.2. Hg _T of surface snow samples	74
4.3.3. Mercury loss in snow samples	74
4.3.4. Spatial variation of mercury from the coast inland	75
4.3.5. Low Hg _T in surface snow: low photo-oxidation or high photo- reduction?	77
4.3.6. Refractory mercury	80
4.4. Conclusion.....	81
4.5. References	82

4.6. Supplementary material.....	95
4.6.1. Instrumental setting and parameter optimization	95
4.6.2. Selection of isotope	95
4.6.3. Calibration and detection limit	96
4.6.4. Blank and washing time	97
4.6.5. References	98

Chapter 5. Records of mercury sequestration in the shallow snow

pits of Dome Fuji, Antarctica	103
Abstract	104
5.1. Introduction	105
5.2. Sample description and experimental methods	108
5.2.1. Sample description	108
5.2.2. Analytical procedures.....	109
5.2.3. Depth-to-age models	111
5.3. Results	112
5.4. Discussion	114
5.4.1. Photochemical impact on mercury concentration in Antarctic Plateau snow	114
5.4.2. Current understanding of seasonal to interannual variation in Hg sequestration	115
5.5. Conclusion.....	117
5.6. References	118

Chapter 6. Seasonal and interannual variation in mercury sequestration in Antarctica Plateau snowpack	130
Abstract	131
6.1. Introduction	132
6.2. Sample description and experimental methods	134
6.2.1. Sample description	134
6.2.2. Instrumentation	134
6.2.3. Reagents and blanks	136
6.2.4. Sample preparation	137
6.2.5. Depth-to-age model	137
6.3. Results	138
6.4. Discussion	139
6.5. Conclusion	144
6.6. References	145

Part III.

Chapter 7. High resolution authigenic $^{10}\text{Be}/^9\text{Be}$ and detrital $^{176}\text{Hf}/^{177}\text{Hf}$ records of marine sediment on Bowers Ridge during 32 – 40 ka	152
7.1. Introduction	153
7.2. Method	154
7.2.1. Sample description	154

7.2.2. Extraction of the authigenic fraction and determination of $^{10}\text{Be}/^9\text{Be}$ ratio	155
7.2.3. Dissolution of the detrital fraction and determination of $^{176}\text{Hf}/^{177}\text{Hf}$	156
7.3. Results and discussion.....	158
7.3.1. Rate of authigenic beryllium burial.....	159
7.3.2. Comparison with the present seawater beryllium	160
7.3.3. $^{10}\text{Be}/^9\text{Be}$ vs. paleo-geomagnetism	161
7.4. Conclusion.....	162
7.5. Appendix – Hafnium contents in authigenic fraction of marine sediment in the Bering Sea	162
7.6. References	164
국문초록	177

List of Figures

Chapter 2. Rain sampler design and sampling strategy for major ions and dissolved organic carbon

- Figure 2-1. (a) The manual bulk rain sampler for major and trace elements and (b) organic carbon. (c) The automatic wet-only sampler.23
- Figure 2-2. Preliminary results. (a) Seoul National University campus on July 3 2008 (b) Gosan Station on April 30, 200724
- Figure 2-3. Three sites (BR1, BR2 and BR3) within the Baengnyeongdo Atmospheric Research Center (BARC)25
- Figure 2-4. The precipitation and wind direction and speed for every 10 minutes during the rain sampling interval.....26
- Figure 2-5. Five-day air-mass back trajectories for individual samples....27
- Figure 2-6. Radar charts for ionic compositions of the BARC samples ...28
- Figure 2-7. The ratios between inorganic components. (a) $\text{nss-SO}_4/\text{Na}$ vs. NO_3/Na , (b) $(\text{NO}_3 + 2 \text{nss-SO}_4)$ vs. NH_4 , (c) $\text{NH}_4 / (\text{NO}_3 + 2 \text{nss-SO}_4)$ vs. $\text{NO}_3/\text{nss-SO}_4$29
- Figure 2-8. The relationship between the compositions of the dissolved organic carbon (DOC and $\delta^{13}\text{C}_{\text{DOC}}$) and inorganic constituents (nss-SO_4 and NO_3).30
- Figure 2-9. The variation of d value that means the degree to which each sampling site contributes to the spatial variation in the rainwater compositions.31

Chapter 3. Assessing the impact of locally produced aerosol on the rainwater composition at Gosan background site in East Asia

Figure 3-1. The location and outline of Gosan Station in Jeju Island, Korea.....	54
Figure 3-2. (a) The molar ratios of NO_3/Na , $\text{nss-SO}_4/\text{Na}$ and NH_4/Na averaged for each wind sector. (b) The frequencies of peaks for NO_3/Na , $\text{nss-SO}_4/\text{Na}$ and NH_4/Na ratios.....	55
Figure 3-3. The relationship between the NO_3/Na ratio and wind speeds	56
Figure 3-4. The frequency distribution map for trajectories computed for 43 NO_3/Na peaks.....	57
Figure 3-5. The molar ratios of $\text{NO}_3/\text{nss-SO}_4$, NO_3/NH_4 and $\text{nss-SO}_4/\text{NH}_4$ averaged for each wind sector.....	58
Figure 3-6. Wind diagram for GS22 and GS27 samples characterized by distinct wind direction.....	59
Figure 3-7. Plot of $\text{nss-SO}_4/\text{Na}$ vs. NO_3/Na molar ratios.....	60
Figure 3-8. The molar ratios of water-soluble ions in total suspended particulate for (a) NO_3/Na , $\text{nss-SO}_4/\text{Na}$, NH_4/Na and (b) $\text{NO}_3/\text{nss-SO}_4$, NO_3/NH_4 , $\text{nss-SO}_4/\text{NH}_4$, monitored at 3 m and 6 m heights on Gosan Station.	61
Figure 3-9. Model result for the quantification of the local influence	62
Figure 3-S1. Time series of NO_3/Na molar ratio with precipitation (mm) and wind directions and speeds from 1998 to 2004.....	64

Chapter 4. Quantification of total mercury in Antarctic surface snow using ICP-SF-MS: spatial variation from the coast to Dome Fuji

Figure 4-1. Sample location along the traverse from the Syowa station via Dome Fuji to the Turning Point and back.....	89
Figure 4-2. Mercury loss from 20 pg g ⁻¹ Hg standard solutions for (a) different container material and (b) different preservatives (0.5% (v/v) BrCl and 100 ng g ⁻¹ AuCl ₃).....	90
Figure 4-3. Total mercury concentrations of surface snow samples (SS1 series) collected along the traverse shown in Figure 4-1	91
Figure 4-4. The relationship between total mercury and altitude (m) and distance from sea ice (km) for SS1 series	92
Figure 4-5. Duplicate analyses of the surface snow samples (SS2 series) analyzed a month apart	93
Figure 4-S1. The error propagation with time when applying the loss rate of the 20p pg ⁻¹ solution	99

Chapter 5. Records of mercury sequestration in the shallow snow pits of Dome Fuji, Antarctica

Figure 5-1. The sampling locations.....	124
Figure 5-2. The profiles of total mercury concentration with sulfate and depth-to-age model	125
Figure 5-3. The box-whisker plot.....	125

Chapter 6. Seasonal and interannual variation in mercury sequestration in Antarctic Plateau snowpack

Figure 6-1. The sampling locations for the 2 m snow pit.	150
---	-----

Figure 6-2. (a) 3-month running average and linear regression line of Southern Annular Mode index (b) Total ozone column and surface UV-B flux at Syowa station, averaged for September – October. (c) Total and labile mercury concentrations in each 2.5 cm layer. (d) – (g) compositions for Na⁺, δ¹⁸O, Cl/Na and SO₄²⁻151

Chapter 7. High resolution authigenic ¹⁰Be/⁹Be and detrital ¹⁷⁶Hf/¹⁷⁷Hf records of marine sediment on Bowers Ridge during 32 – 40 ka

Figure 7-1. The sampling location Site U1341 with other coring sites during IODP expedition 323168

Figure 7-2. The profiles of (a) ¹⁰Be/⁹Be ratio, (b) ¹⁰Be and (c) ⁹Be concentrations, (d) NRM_{int}/χ as a paleointensity proxy, (e) magnetic susceptibility (χ), (f) intensity of natural remanent magnetism (NRM_{int}), (g) inclination of natural remanent magnetism, and (h) declination of natural remnant magnetism. 169

Figure 7-3. Compiled ¹⁰Be/⁹Be ratio of deep seawater in the North Pacific, Bering Sea and Arctic Ocean170

Figure 7-4. The vertical profiles of ⁹Be and ¹⁰Be concentrations and their ratios at three sites in the North Pacific including one site in the Bering Sea171

Figure 7-5. Simulated atmospheric deposition flux of ¹⁰Be on land or sea surface during 1998-2003172

Figure 7-6. New u-channel data for the intensity of natural remanent magnetism (NRM 20mT) and inclination of NRM173

List of Tables

Chapter 2. Rain sampler design and sampling strategy for major ions and dissolved organic carbon

Table 2-1. The dissolved major ion and organic carbon composition of rainwater samples at BARC in 2009.....	32
Table 2-2. The concentration of NO ₃ , nss-SO ₄ and Na and their ratios monitored at various sites on the Korea Peninsula	33

Chapter 3. Assessing the impact of locally produced aerosol on the rainwater composition at Gosan background site in East Asia

Table 3-1. Water-soluble ion concentrations of total suspended particulate in Gosan Station.....	63
--	----

Chapter 4. Quantification of total mercury in Antarctic surface snow using ICP-SF-MS: spatial variation from the coast to Dome Fuji

Table 4-1. Published total mercury concentrations (Hg _T) in Antarctic snow	94
Table 4-S1. Instrumental parameters for Element2.....	100
Table 4-S2. Sampling information and analytical results of SS1 sample set	101
Table 4-S3. Sampling locations and analytical results for SS2 samples set	102

Chapter 5. Records of mercury sequestration in the shallow snow pits of Dome Fuji, Antarctica

Table 5-1. Mercury sequestration rates estimated from Antarctic snowpack or ice core.....127

Table 5-1. Total mercury concentrations in each layer of Pit-A and Pit-B128

Chapter 6. Seasonal and interannual variation in mercury sequestration in Antarctic Plateau snowpack

Chapter 7. High resolution authigenic $^{10}\text{Be}/^9\text{Be}$ and detrital $^{176}\text{Hf}/^{177}\text{Hf}$ records of marine sediment on Bowers Ridge during 32 – 40 ka

Table 7-1. The column procedure for Hf separation174

Table 7-2. The contents (ng per g of bulk sediment) of Hf and various elements in authigenic fraction of Site U1345A core sediments, recovered by 0.2 M HNO_3 and mixed solution of acetic acid and hydroxylamine hydrochloride (HH).....175

Table 7-3. The improvement of authigenic hafnium extraction from sediment (2 g) by doubling the volume of the leachnig solution (0.2 M HNO_3) and by additional leaching step.....176

Chapter 1

Introduction: Atmospheric and oceanic precipitation
chronicling Earth's changes

The Earth changes. The Earth can be divided into several interconnected subsystems (i.e., atmosphere, biosphere, hydrosphere, cryosphere, and geosphere), and a perturbation in one of them is not localized but can propagate to other subsystems, and can even be returned as positive or negative feedback. For example, increasing disturbance derived from human activities, sometimes referred to as the anthroposphere, has impacted the entire Earth system and threatened human habitats. This has become a serious global concern, and great efforts are being made to understand and cope with the changing Earth.

The Earth chronicles the changes. This provides a basic and essential means for investigating how a perturbation affects the Earth system, reconstructing the past and predicting the future of the Earth system. For instance, precipitation is a fundamental tool for the Earth to record the changes. In the scientific meaning of the word, it has two different definitions – (1) the falling to earth of any form of water and (2) the process of forming a chemical precipitate. Both descriptions involve thermodynamic phase transitions, but they have differences in their initial and final phases – vapor and liquid/solid for definition (1) and liquid and solid for definition (2). The former process prevails in the atmosphere and the latter is dominantly found in the ocean, the largest reservoir of the hydrosphere. The Earth sacrifices the entropy to produce precipitates whose composition reflect the place and the time that they occur and hands the precipitates over to the

geoscientists. The precipitates in the atmosphere are generally transient records supposed to be monitored, but the cryosphere represents their natural archive to be retrieved. In the ocean, the authigenic minerals produced by biologic activities or by precipitation on the allogenic are also to be recovered from the seabed. This thesis deals with the chemical composition of the precipitates collected from the various subsystems of the Earth in efforts to contribute to the understating of how the subsystems interact and how the Earth accordingly changes.

1.1. Atmospheric precipitation

Atmospheric precipitation is the result of the condensation of water vapor and subsequent falling to Earth surface under gravity. Depending on the ambient temperature, this phenomenon usually results in rainfall or snowfall. They are important removal mechanisms of aerosols from the atmosphere, referred to as wet deposition that includes in-cloud and below-cloud scavenging depending on the height where it happens. Their composition is then not purely water but inherits the aerosol composition and is expected to provide valuable information as to the behavior of the aerosols, specifically their source, transport and deposition.

The rainwater composition has been monitored at a number of sites on the Earth surface for the last several decades. These researches have

focused on the atmospheric pollution, acid deposition, vapor source as water resource inventory, or wet deposition of aerosols. Recently, because rainfall acts as a natural sink for aerosols that have direct/indirect effects on radiative forcing, the wet deposition is particularly concerned with respect to the climate change. In this case, it is more relevant to pay attention to aerosols that spend a long time in the atmosphere, which would bring more interaction with the sunlight than do aerosols temporarily produced from the local region. For this reason, wet deposition is preferably monitored at rural sites that represent the regional background atmosphere receiving aerosols transported long-range and little local influence. However, for valuable evaluation of wet deposition at a regional scale, it is important to carefully assess various factors that can affect the rainwater composition at a local scale. This is additionally helpful for discriminating the aerosol sources and evaluating their individual loads to the atmosphere and corresponding climatic effects.

Part I presents the effort of detecting the local factors that affect the rainwater compositions. It includes the design of the rain collector for both inorganic and organic matter, a case study at the Baengnyeongdo Atmospheric Research Center (BARC) (Chapter 2), and evaluation of the local influence in the rainwater composition previously reported at Gosan Station, Jeju, Korea (Chapter 3). Both BARC and Gosan Station are rural sites expected to have relatively low influence from the locality and be

strategic sites for monitoring continental outflow. Chapter 2 deals with how to collect the rainwater. Both manual bulk collector and automatic wet-only collector are developed for the sampling of dissolved inorganic ions and dissolved organic carbons (DOC). A case study at BARC reveals the meter-scale variability of rainwater composition based on simultaneous rain sampling at multiple positions. It appears that temporary formation of a rain shadow depending on the wind conditions and natural and artificial topography make differences in the amount of precipitation among the rain collectors and hence the rainwater composition. This stresses the importance of the installation of the rain collector at a suitable location. Additionally, possible sources of the dissolved inorganic ions (nitrate, non-sea-salt sulfate and ammonium) and DOC are proposed based on their concentrations, ratios, and carbon isotope composition of DOC – fossil fuel combustion, marine biogenic emission and agricultural emission. Whereas an indirect local effect by the rain blocking is presented in Chapter 2, Chapter 3 highlights the direct effect of locally produced aerosols on the rainwater composition. In Gosan Station situated at the western tip of Jeju Island, eastern winds generate and deliver aerosols from the cultivated regions of the island's inland, and western winds supply marine aerosols to this site. Consequently, the rainwater composition has a portion that displays a wind directional variability. This portion is detected from a 14-year record of dissolved inorganic ion concentrations and quantified in order to evaluate the wet

deposition more representative of the regional background atmosphere.

The snowfall is an important process, especially in the polar regions, which forms and maintains the cryosphere. Whereas rainwater is immediately dissipated once it reaches the ground, polar snow over the continents (e.g., Greenland, Antarctica) is perennially preserved and fairly well preserves its constituents. This allows the thick polar snowpack (or ice) to represent a natural archive of the past atmospheric environment, which allows for the researches on the paleoclimate. In a different perspective, most constituents once deposited within snow are quasi-permanently sequestered within the snowpack. This means the cryosphere acts as their natural sink. Although the polar regions are the most pristine area on the Earth and the polar snow is very pure, the sequestration can potentially be a significant flux for certain materials in their global geochemical cycle.

In Part II, total mercury concentration (Hg_T) is analyzed from surface snow (Chapter 4) and snow pits (Chapter 5 and 6) obtained from the Antarctic Plateau. There have been intensive studies on the behavior of mercury in each subsystem of the Earth and its global cycle, but those in the Antarctic Plateau are not fully understood in spite of its large extent (~5 million km^3). The emerging studies of the mercury dynamics on the Antarctic Plateau point to active interaction between the atmosphere and surface snow. However, measurements of Hg_T in the snowpack are rarely achieved due to difficulties both in the sampling and analysis, whereas

atmospheric Hg is increasingly determined. Then, it is expected that Hg_T records in Part II contribute to the comprehensive understanding on the mercury dynamics in the Antarctic Plateau and its role in the global mercury cycle. This involves a particular issue of the impact of the photochemistry during the sunlit period on the Hg_T in the Antarctic snowpack.

Chapter 4 presents Hg_T of surface snow samples collected along a ~1500 km transect in east Queen Maud Land during the austral summer. It is low ($< 0.4 - 10.8 \text{ pg g}^{-1}$, $n=44$) without a signal of depositional enhancement accompanying photo-oxidation of atmospheric elemental mercury in austral summer and with the dynamic variation along the transect implying spatial and temporal heterogeneity in its source processes. In Chapter 5, Hg_T are determined from two snow pits taken every 5 cm down to 4 m at Dome Fuji. Only a few results display enhanced mercury sequestration during the sunlit period, which is, however, limited to pg g^{-1} level. Due to the low mercury contents in the Antarctic snow samples seen in Chapters 4 and 5, more precise determination of Hg_T is required to investigate the seasonal variation. Accordingly, the analytical method is refined, and the seasonal and interannual variation in mercury sequestration could be addressed in Chapter 6. It is shown that sea-salt plays a major role in Hg sequestration whose enhancement is detected at the onset of the sunlit periods. Then the gradual decrease of Hg sequestration over the last 24 years can be attributed to the reduction of the poleward transport of sea-salt.

1.2. Precipitation in seawater

Hydrogenous material generated by precipitation in seawater is thought to inherit the seawater composition where and when they are formed, so it has been widely applied to paleoceanographic and paleoclimate research. They can be produced directly from seawater or through biologic activities. For example, ferromanganese crusts and nodules form in oxidizing condition directly from seawater, which involve precipitation or accumulation of precipitates on the sea floor and pelagic sediment in areas of very low sedimentation rates. Under moderate sedimentation rates, ferromanganese coatings on sedimentary particles are more common products of authigenesis. The biogenic precipitates include carbonate shells of foraminifera, corals, and fossil fish debris and teeth, for which time-resolving analyses are particularly challenging.

Studies using marine sediment cores have an advantage in that the chemical variation over time can be continuously reconstructed with high resolution. They can provide information not only on cyclic variations in seawater composition in response to, for example, glacial-interglacial environment changes, but also on episodic and temporal events such as geomagnetic excursions. In Chapter 7 (Part III), seawater $^{10}\text{Be}/^9\text{Be}$ ratio during 32 – 40 ka are reconstructed by extracting authigenic fraction from

the sediment cores obtained on the Bowers Ridge during IODP (Integrated Ocean Drilling Program) Expedition 323 “Pliocene-Pleistocene paleoceanography and climate history of the Bering Sea”. In addition, $^{176}\text{Hf}/^{177}\text{Hf}$ ratio of the detrital particle is determined. The $^{10}\text{Be}/^9\text{Be}$ ratio in seawater is controlled by individual fluxes of ^{10}Be and ^9Be to the sea from their different sources. ^{10}Be is a cosmogenic nuclide produced mostly by spallation reaction induced by cosmic ray in the upper atmosphere and delivered to the sea through the hydrological cycle. On the other hand, ^9Be is dominantly supplied from the continents by riverine input as a weathering product. Therefore, it can be expected that their ratio varies with weathering intensity and geomagnetic intensity that modulate the influx of cosmic ray. Combined with the detrital $^{176}\text{Hf}/^{177}\text{Hf}$ ratio that provides information on the source and transport of the terrigenous particles, the variation in the $^{10}\text{Be}/^9\text{Be}$ ratio can be further elucidated.

PART I

Chapter 2

Rain sampler design and sampling strategy for major ions and dissolved organic carbon

2.1. Introduction

How to collect rain samples is an important issue, because the sampling strategy can significantly affect the rainwater composition. For example, “bulk sampling” represents the easiest way to collect rainwater. This method simply exposes an empty bottle to rain often coupled with a funnel to widen the sampler mouth. The sampler is continuously exposed to the atmosphere and thus is subject to additional dry deposition of aerosol during non-raining period, unless it is installed and retrieved at the beginning and end of rainfall event. On the other hand, “wet-only sampling” adopts an electric circuit that receives a signal from the rain sensor and accordingly opens or closes the lid of the sampler. This method can reduce unintended dry deposition and sample evaporation from the container when the rain stops temporarily or completely and conserve the initial composition of rainwater.

Beside bulk *vs.* wet-only sampling, various factors associated with the sampling strategy can influence the rainwater composition: material of the sampling device, sampler cleanness, sampling location and its height from the ground, and sample transport and storage until chemical analyses. Therefore, it is required to optimize the sampling strategy including the sampler design and sampling position depending on the constituent of interest. Rain samplers targeting dissolved inorganic and organic components were individually designed. As a case study, these samplers were applied for simultaneous sampling at multiple positions in the Baengnyeongdo Atmospheric Research

Center (BARC), in order to observe meter-scale spatial variability of rainwater composition. This would be helpful for elucidating the local factors that influence rainwater composition and selecting an appropriate site for the long-term monitoring. Additionally, based on the inorganic and organic composition of the rainwater, it was attempted to identify their sources at BARC. This is proposed as a preliminary guideline for interpreting the rainwater composition at this station.

The potential climatic and environmental impacts of organic aerosols are well addressed in Jacobson *et al.* (2000). For example, they make up a large part of atmospheric fine particles (Kanakidou *et al.*, 2005), which can scatter or absorb solar radiation, affect the lifetime and optical property of clouds and hence are important for radiative budget. Rainfall is an important removal mechanism for atmospheric organic carbon with a flux of 400 TgC yr⁻¹, accounting for about 6% of the emission from fossil fuel combustion (Willey *et al.*, 2000; Avery *et al.*, 2006). In this study, the concentration and isotopic ratio of dissolved organic carbon in rainwater at BARC are relevant as a case study outlining the method due to the paucity of samples.

2.2. Rain sampler design

2.2.1. Bulk sampling

Bulk sampler is simple and convenient, and once installed, no particular effort is required to maintain it. In this study, three types of bulk

sampler are designed for collecting (1) dissolved major ions (i.e., Na^+ , K^+ , Ca^{2+} , Mg^{2+} , NH_4^+ , Cl^- , SO_4^{2-} , NO_3^-), (2) trace elements, and (3) dissolved organic carbon (DOC).

2.2.1.1. Dissolved major and trace elements

The rainwater sample for major and trace elements is collected in a pre-cleaned HDPE (high density polyethylene) bottle (125 mL wide mouth, Nalgene) through LDPE (low density polyethylene) funnel (51 mm dia., Nalgene) (Fig. 2-1a). The funnel, having a truncated cone-shaped stem, is tightly connected to a bottle cap through ~10 mm hole drilled at the center, so raindrops only pass through the funnel into the bottle. The sampling bottle for major cations (Na^+ , K^+ , Ca^{2+} , Mg^{2+} , NH_4^+) and trace elements is acid-cleaned as follows: A new bottle is rinsed with deionized water (DI water, Puris Esse-UP water system with additional metal filter, miraeST) several times, wiped with a cleanroom wiper within dilute detergent solution (L900, Nalgene), and soaked overnight in the detergent solution. After rinsing thoroughly with DI water, the bottle is filled with 1M HCl (HP-100H grade, Eco-research) and heated overnight in an oven at 60°C. It is thoroughly rinsed and filled with DI water and heated overnight at 60°C. Finally, the bottle is rinsed and dried in a clean bench equipped with ULPA filter. For major anion (Cl^- , SO_4^{2-} , NO_3^-) sampler the acid-cleaning step is skipped in order to avoid potential input of chloride from HCl. The pre-cleaned HDPE bottles are prepared for single use, but the funnels are reused after cleaning following the described procedures above. For outdoor installation of the sampler, 1 to 2-m-long polyvinyl

chloride (PVC) pipe jointed with PVC reducing socket is used (Fig 2-1a). The reducing socket is heated and reformed to enable the sampler bottle to be tightly inserted.

2.2.1.2. Dissolved organic carbon

Bottles and funnels made of glass are used for the DOC sampling. The glass bottle (2 L, Daihan Scientific) is firmly connected with the funnel (30 cm diameter, Pyrex glass, Samsung Scientific) through open top screw cap and silicon septa (GL45, Schott-Duran) (Fig. 2-1b). To eliminate pre-existing carbon and its compounds from the bottle and funnel, they are soaked overnight in 10% (wt.) NaOH solution and rinsed five times with DI water. Then, they are immersed and shaken in 0.1 M HCl bath and rinsed again with DI water. After heating in an oven at 150°C, they are fully wrapped with aluminum foil to prevent further contamination until use. The cap and septa are cleaned using DI water. To install the sampler in the field and protect the glassware against damage, a stainless steel jacket is prepared (Fig. 2-1b).

2.2.2. Wet-only sampling

An automatic wet-only rain sampler was manufactured in collaboration with Weathertech (Fig. 2-1c). It consists of four parts – the sensor, gauge, control circuit and sampler. The rain sensor detects a change of resistance (impedance) on its surface. When raindrops fall on the sensor surface, the resistance is dropped. According to the signal from the sensor, the control circuit makes the lids of the gauge and sampler to open and start rain

collection. When rainwater collected in the rain gauge reaches a preset level (one of 125 (default), 155, 185, and 215 mL), it is discharged and the sampler platform rotates to the next position. All eight containers can be placed on the sampler platform, which allows sequential sampling so that one can observe variation in the rainwater composition during a continuous rain event. The Teflon-coated funnel of the sampler part has a diameter of 20 cm. Then, a 125 mL container is capable of collecting 4 mm of precipitation. The sample container (HDPE) was prepared the same as the bulk sampler. The wet-only sampler is initially aimed at targeting dissolved inorganic components, but it is compatible for the sampling of DOC by substitution of the current funnel into a pre-combusted metallic one (or glass funnel) and of the sample container into pre-cleaned glassware.

2.3. Preliminary study of meter-scale spatial variability of rainwater composition on the Seoul National University campus and at Gosan Station

The campus of the Seoul National University (SNU, 37.459°N, 126.950°E, ~100 m above mean sea level, amsl) is located on the slopes of the Gwanak Mountain (629 m amsl) in Seoul. The bulk samplers were installed at five different locations on the rooftops of three buildings within 100 m (Fig. 2-2a), on 3 July 2008. The rainwater was filtered through 0.2 μm cellulose acetate membrane filters and analyzed for the major anions using an ion

chromatograph (ICS-2000, Dionex) at the SNU laboratory. All results agreed within 9% (relative standard deviation, RSD) for every anion species (Fig. 2-2a), lower than typical analytical uncertainty (<10%). This implies that the influence of the sampler devices themselves or local surroundings was negligible during the rain event.

The Gosan station is located at the western tip of Jeju Island, Korea and regarded as an ideal site for monitoring the background atmosphere in East Asia. On April 30, 2007, rainwater was simultaneously collected from two different locations at this site; on the rooftop of an observatory (4 - 5 m height) and at ground level (1 - 2 m height) ~50 m away from the building (Fig. 2-2b). The pH and conductivity were significantly higher for the rooftop sample than for the ground sample (Fig. 2-2b), suggesting significant meter-scale spatial variability of rainwater composition. The spatial variability in the Gosan station will be further discussed in chapter 3.

2.4. Case study at BARC

2.4.1. Sample location, collection and analyses

Baengnyeong Island (~52 km² area, <10,000 residents) is located in the Yellow Sea, ~20 km to the west of the Korea Peninsula and ~200 km east of the Shandong Peninsula, China (Fig. 2-3). The forests (both coniferous and broad-leaved) and farmland make up ~60% and ~30% of the total area, respectively. About half the agricultural land is cultivated with

rice, and barley, wheat, buckwheat, potato, sweet potato and red pepper are also widely grown. The BARC (37.966°N, 124.630°E, 120 m amsl) building is situated on a hillside and the closest seashore is ~700 m to the north and ~10 km to the east. Various atmospheric monitoring equipment and analytical instruments are installed inside and outside (on the terrace) of the building.

Three sampling sites were chosen all within 30 m: Site BR1 on the north side of the third floor terrace of the BARC building, Site BR2 on the second floor terrace and Site BR3 on flat ground behind the building at similar height as BR2. At each site, two manual bulk samplers for major ions and DOC were set 1 m above the terrace or ground surface (Fig. 2-3). Four rain events were sampled on July 8, 11, 13 and 17 of 2009. All four events were torrential, so the sample bottles (~2 L) had to be changed in the middle of the event. These replacement bottles were treated as separate samples (Table 2-1), and thus, eight samples were collected at each site. The sample ID is designated as “0708A-BR1” that indicates the first sample bottle (A) collected on July 8 at BR1 site. The second bottle uses “B”. The samplers were installed fast as the rain began and recovered when it ceased, which approximated wet-only sampling. However, for 0714B and 0717B samples, the sampler recovery was delayed due to strong winds (Fig. 2-4), and they should be considered as bulk samples.

After retrieved, the samples for major ions were stored frozen. An aliquot (<20 mL) from the DOC sample was set aside and used to determine pH and conductivity (PC-300, Oakton). The remaining DOC samples were filtered through 0.7 µm glass fiber filters (GF/F) pre-combusted at >450°C for

at least 5 hours into pre-cleaned glass bottles ($2 \times 1\text{L}$). The bottles were wrapped with aluminum foil and frozen until further analyses. Each filter was contained in a petridish and sealed with Parafilm.

In the laboratory at BARC, the samples for major ions were melted, filtered through $0.2 \mu\text{m}$ cellulose acetate membrane filters and analyzed using ion chromatography (ICS-2000, Dionex). The BCR-CRM 408 solution, which was used to check the accuracy, gave results within 10% of the certified concentrations. In the laboratory at SNU, the DOC samples were melted and aliquoted into 40 mL amber glass vials (I-CHEM, S246-0040) and sent to G. G. Hatch Stable Isotope Laboratory at Ottawa University, Canada for the analyses of concentration and stable carbon isotope ratio ($\delta^{13}\text{C}$) of DOC. The DOC content was determined using a TIC-TOC analyzer (OI Analytical model 1030), and $\delta^{13}\text{C}_{\text{DOC}}$ was analyzed using stable isotope ratio mass spectrometer (Finnigan MAT DeltaPlus). The precisions were 2% (2σ) for DOC and 0.2‰ (2σ) for $\delta^{13}\text{C}_{\text{DOC}}$.

2.4.2. Meteorological information and air mass back trajectory analysis

The precipitation (mm) and wind direction (degree) and speed (m s^{-1}) during the rain sampling interval recorded every 10 minutes by an automatic weather station (AWS) were obtained from the Korea Meteorological Administration web site (<http://www.kma.go.kr>) (Fig. 2-4). The air mass back trajectory analysis was conducted with the NOAA/HYSPLIT (National Oceanic and Atmospheric Administration/Hybrid Single-Particle Lagrangian Integrated Trajectory) model using meteorological data from NCEP/GDAS

(National Centers for Environmental Prediction/Global Data Assimilation System) (Draxler and Rolph, 2012). Five-day back trajectories of air mass with the starting heights each at 100, 500 and 1500 m above ground level were computed at 10 minute intervals during the rain sampling periods. Then, multiple trajectories for each sample were illustrated on a map by means of the frequency of two-dimensional intersection between map grid cell (1×1 degree) and the trajectories projected on the map. The projection is performed for the trajectories laid between 0 and 500 m (1st and 3rd columns in Fig. 2-5) and between 0 m and model top (10 km above ground level; 2nd and 4th columns in Fig. 2-5), respectively, in order to discern relative contribution of air mass that once encountered the surface.

2.4.3. Results

The major ion concentrations, TZ^+ ($[Na^+]+[K^+]+2[Ca^{2+}]+2[Mg^{2+}]+[NH_4^+]$), TZ^- ($[F^-]+[Cl^-]+[NO_3^-]+2[SO_4^{2-}]$), pH and conductivity data are shown in Table 2-1. pH and conductivity were 4.24 – 6.03 and 3.07 – 12.25 μS , respectively. The bulk samples (0713B and 0717B) displayed exceptionally high conductivities of 81.6 - 580 μS , perhaps due to additional dry deposition. By assuming that all sodium in the samples is marine origin, the contribution of sea salt is calculated using the sea water composition of $SO_4/Na = 0.06028$, $Ca/Na = 0.02161$, $Cl/Na = 1.164$, $Mg/Na = 0.1127$ and $K/Na = 0.02177$ (all ratios are molar ratio unless otherwise noted) (Hara *et al.*, 2011; Pilson, 1998). It is estimated that 10 - 84% of total ion contents ($TZ^+ + TZ^-$) originated from sea salt (Table 2-1). In the successive samples of the four

rain events, the relative contribution of sea salt is higher in the second bottles than the first bottles. This can be attributed to the below-cloud aerosol scavenging and wind-blown sea salt. The below-cloud scavenging refers to an aerosol washout process by rainfall and is more efficient at the earlier stage of the precipitation. Then, this is responsible for higher concentration of non-sea salt (nss) components (e.g., NH_4^+ , NO_3^- and nss-SO_4^{2-}) in the first bottles (0708A and 0711A) compared to the second bottles (0708A and 0711B) (Fig. 2-6). The winds are commonly stronger during the intervals for the second bottles, especially for the bulk samples, than for the first bottles (Fig 2-4). The bulk samples are dominated by sea salt input (65 – 84%) in spite that they contain large nss components than other samples (Table 2-1). This indicates that sea salt is the predominant components for major ions subject to wind-driven production, transport and dry or wet deposition. This is consistent in the wet-only sample pairs, in which relative fractions and absolute concentrations of sea salt as are higher in the second bottles with stronger wind speeds (Fig. 2-6; Table 2-1).

The DOC content ranged between 30 and 110 μM (Table 2-1), comparable to the results from Seoul ($\sim 77 \pm 31 \mu\text{M}$, volume-weighted mean in July 2010; Yan and Kim, 2012). The DOC contents are positively correlated with nss-SO_4 and NO_3 with slopes of 0.10 ($\text{nss-SO}_4/\text{DOC}$) and 0.15 (NO_3/DOC), respectively (Fig. 2-8a and b). These values are lower than the results in Seoul (0.28 and 0.30, 2009. 10 – 2010. 9; Yan and Kim, 2012), possibly due to seasonal variation in these values or remoteness of BARC with low local emissions of nss-sulfate and nitrate. Like nss-SO_4 and NO_3 ,

DOC shows the effect of the below-cloud scavenging with the higher contents in the first bottles than in the second bottles within the successive sample pairs (Fig. 2-8a and b). The coherence between the organic and nss-inorganic compositions may indicate the presence of common sources. $\delta^{13}\text{C}_{\text{DOC}}$ varied from -24.1‰ to -22.6‰ except for an anomalous result (-33.45‰ in 0713B). These values are close to the aerosol composition at the Gosan Station, Jeju Island during the summer (-24 – -23 ‰, Jul – Sep in 2001; Kawamura *et al.*, 2004).

2.4.4. Discussion

2.4.4.1. Identification of major sources for rainwater constituents

Four types of major sources for dissolved ions are expected at BARC – sea salt, fossil fuel combustion, agriculture and marine biogenic emission. The relative contribution of sea salt and nss components can be illustrated by plotting $\text{nss-SO}_4/\text{Na}$ vs. NO_3/Na ratios (Figure 2-7a): sea salt lowers those ratios and nss components increase them. This statement can be verified by previous studies carried out at various sites on the Korean Peninsula (Kim *et al.*, 2006; Kang *et al.*, 2003; Lee *et al.*, 2000). When compiled on a plot, the coastal sites display lower ratios around the origin whereas inland sites have higher ratios, in response to the relative contribution of sea salt versus anthropogenic sources of nss-SO_4 and NO_3 . Interestingly, all points appear to fall on a linear line with a slope of ~ 1 , suggesting the regional background composition of rainwater on the Korea Peninsula to be $\text{nss-SO}_4/\text{NO}_3 \sim 1$ during the investigated period. The majority of the BARC samples are plotted

near the origin, reflecting that sea salt is the primary component. Some elevated ratios plot around the points for the inland sites lying on the 1:1 line, but 0711A and two of 0708A exhibit nitrate excess.

Although combustion of fossil fuel accounts for the largest source of atmospheric NO_x and SO_2 in East Asia (Luangjame *et al.*, 2011) and the world (Denman *et al.*, 2007), the correlation between $(\text{NO}_3 + 2 \text{ nss-SO}_4)$ and NH_4 (Fig. 2-7b) provide an insight for another source of these nss-species – the agricultural activities. This is supported by the facts that (1) agriculture is the most significant source of NH_3 in the atmosphere (Luangjame *et al.*, 2011) and (2) The general formula of a probable source that can be induced from the correlation is $(\text{NH}_4)_3(\text{NO}_3)(\text{SO}_4)$ (Fig. 2-7b), and ammonium sulfate and ammonium nitrate are common constituents of fertilizers. The samples having excess nitrate (0711A and 0708A; Fig. 2-7a) have the largest NH_4 and plot close to the 1:1 equiline in Fig. 2-7b. This reflects that the agricultural source are somewhat enriched in nitrate (or NO_x) compared to sulfate (or SO_2).

Fig 2-7c, drawn by combining Fig2-7a and b, allows for better discrimination of the agricultural contribution from two other major sources of nss components – fossil fuel combustion and marine biogenic emission. The agricultural impact is characterized by $\text{NO}_3/\text{nss-SO}_4$ ratio (x-axis) higher than its regional background composition of ~ 1 (Fig. 2-7a) and by $\text{NH}_4/(\text{NO}_3+2 \text{ nss-SO}_4)$ ratio (y-axis) close to ~ 1 (Fig. 2-7b). In contrast, combustion of fossil fuel generates more NO_x and SO_2 than NH_3 and hence lower the $\text{NH}_4/(\text{NO}_3+2 \text{ nss-SO}_4)$ ratio. The $\text{NO}_3/\text{nss-SO}_4$ ratio can vary widely depending on fuel type. It is lowered by use of crude oil or coal and raised by

utilizing desulfurized fuel (e.g., gasoline and diesel). Rainwater composition in East Asia monitored by EANET during 2005 – 2009 showed that $\text{NO}_3/\text{nss-SO}_4$ was below 1.0 at 27 out of the 45 sites monitored and was especially low in China (0.3 - 1.0), Vietnam (0.5 - 0.6), Russia (0.5 - 1.0) and Mongolia (~0.8) (Hara *et al.*, 2011) due to combustion of fossil fuel. Therefore, fossil fuel combustion is more likely to lower the $\text{NO}_3/\text{nss-SO}_4$ ratio below the background composition (~1) in East Asia. Oceanic emission of dimethylsulfide (DMS, $\text{C}_2\text{H}_6\text{S}$) is globally the second largest source of sulfur-containing compounds in the atmosphere (24 TgS yr^{-1} ; Penner *et al.*, 2001). DMS is a precursor that can be converted to sulfate by a series of oxidation reactions. The biogenic emission from the sea is also a considerable source for NH_3 in the atmosphere (8.2 TgN yr^{-1}), whereas its contribution to NO_x is thought to be negligible (Denman *et al.*, 2007). Then, marine biogenic emission would lead to decrease of both $\text{NO}_3/\text{nss-SO}_4$ and $\text{NH}_4/(\text{NO}_3+2 \text{ nss-SO}_4)$ ratios in rainwater. Overall, agricultural source represents relatively elevated ratios of both $\text{NO}_3/\text{nss-SO}_4$ and $\text{NH}_4/(\text{NO}_3+2 \text{ nss-SO}_4)$ compared to the products of fossil fuel combustion and marine biogenic emission (Fig 2-7c). Therefore, by using these two ratios, relative contribution of agricultural can be discriminated from the other two sources.

The coherence between the dissolved compositions of organic carbon (DOC concentrations and $\delta^{13}\text{C}_{\text{DOC}}$) and inorganic components (nss-SO_4 and NO_3) is helpful to further elucidate their sources. The correlation between DOC and nss-SO_4 (Fig. 2-8a) is preserved when normalized by NO_3 (Fig. 2-8c). The DOC/NO_3 ratio like $\text{nss-SO}_4/\text{NO}_3$ ratio can discriminate

between agricultural impact (lower DOC/NO₃) and contribution of fossil fuel combustion or marine biogenic emission (higher DOC/NO₃) (Fig. 2-8c). Further discrimination can be achieved with $\delta^{13}\text{C}_{\text{DOC}}$. Generally, $\delta^{13}\text{C}_{\text{DOC}}$ of marine biogenic emission (~-21‰; Williams and Gordon, 1970) is heavier than that of fossil fuel combustion (-26 – -30‰) and terrestrial biogenic emission (~-26‰; Avery *et al.*, 2006; Andres *et al.*, 1996). By combining the $\delta^{13}\text{C}_{\text{DOC}}$ with nss-SO₄/NO₃ ratio (Fig. 2-8d) or DOC/NO₃ ratio (Fig. 2-8e), the dissolved composition of the rain samples can be explained by these three sources. The compositions of 0713A and 0717A are characterized by the background nss-SO₄/NO₃ ratio (~1) and heavy $\delta^{13}\text{C}_{\text{DOC}}$ with relatively abundant marine biogenic input (Fig. 2-8d). This is consistent with the results of air mass back trajectory analyses, which shows transports of air mass from the ocean with little interaction with the surface (Fig. 2-5i, j, m and n). In the consecutive sample pairs (0708A-0708B, 0711A-0711B), interestingly, the second samples exhibit larger contribution from fossil fuel with higher nss-SO₄/NO₃ ratio and lighter isotopic composition, whereas the first samples lie close to marine biogenic and agricultural sources (Fig. 2-8d). Change in air mass pathway is not the cause of the compositional transition, because the first and second samples have similar back trajectories (Fig. 2-5a to h). One possible explanation is that wash-out is an efficient removal mechanism for marine biogenic and agricultural aerosols but aerosols from fossil fuel emission persist during the rainfall.

The intersecting points of three lines that envelop all data points in Fig. 2-8e would approximate the compositions of the three endmembers.

These points have $\delta^{13}\text{C}_{\text{DOC}}$ of -22‰ for marine biogenic source slightly lighter and -25‰ and -24‰ for fossil fuel and agricultural sources heavier than the previously suggest ranges. This would be due to limited date points in this study or the regional sources having distinct isotopic composition. The endmember compositions are required to be further refined for the regional sources in East Asia, which would be helpful for the quantitative apportionment of the sources.

2.4.4.2. Meter-scale spatial variation in the rainwater composition

The relative standard deviation (RSD) of the simultaneous samples (BR1, BR2 and BR3) can be an index of the spatial variation in the rainwater composition. RSD was calculated for individual ions, which varied widely from 3% (Ca^{2+} of 0711B) to 94% (Ca^{2+} of 0708B). The impact of sampling position on the spatial variance was inconsistent. The degree to which each sampling site contributes to the spatial variance (d) is evaluated using the following equation:

$$d_i = \sum_x \frac{|X_i - \bar{X}|}{\bar{X}}$$

where X_i is the concentration each ion species (Na^+ , K^+ , Ca^{2+} , Mg^{2+} , NH_4^+ , Cl^- , NO_3^- , SO_4^{2-}) at sampling site i (BR1, BR2, BR3) and \bar{X} is the average over the three sites for each ion. A great d value indicates large deviation from the spatial mean (large RSD) and thus spatial distinction. Fig. 2-9 shows the d values of each sampling site for individual sample sets. They are relatively high for rain events 0708B and 0713A and low for 0711B. Such spatial

disagreement (large d value) and its instability (fluctuation of d value) mark the presence of local factors and their erratic influence on the rainwater composition. In the BARC samples, the local influence would be primarily the rain blocking effect. The rain blocking is caused by buildings or natural relief that form temporal rain shadow depending on the wind condition and can affect the amount of precipitation received. Site BR2 is located on the second floor and has an elevation similar to the ground site BR3. However, the blocking effect of the upper story of the building resulted in the lowest precipitation at BR2 in most cases (Table 2-1). In addition to the indirect influence of rain blocking, aerosols stirred up locally by the wind can directly affect the rainwater composition as seen in the bulk samples. Site BR3 is apt to be affected by the locally produced aerosols due to its proximity to the ground surface, an earthen platform for AWS. Taking these into consideration, BR1 is thought to be the best site for the long-term rainwater monitoring in BARC. This is also supported by the cumulative d values, which are lower for BR1 ($\sum d_{BR1} = 0.94$) than for BR2 ($\sum d_{BR2} = 1.23$) and BR3 ($\sum d_{BR3} = 1.14$).

2.4.4.3. Contributions of bulk sampling to monitoring the rainwater composition

Compared to the wet-only sampling, bulk sampling is liable to change the composition of wet deposition with additional dry deposition as seen in the results. However, it still provides useful guidelines for monitoring the rainwater composition. First, the bulk sampling captures raindrops from

the very beginning of a rain event, which can be missed in the wet-only sampling due to a delay in activation of the rain sensor. The raindrops at the beginning of a rain event is shown to contain ionic contents up to 50 times higher than the average of the total rainfall owing to aerosol wash-out effect (Lim *et al.*, 1991), which can be a significant fraction of the total wet deposition. Second, if the sources of the local aerosols are consistent at a sampling site, bulk sampling can collect more locally produced aerosols so that one can easily trace the local sources and assess their influences. For long-term monitoring, the local effect should be monitored anyhow, because it can matter even in wet-only sampling especially when a rain event accompanies strong wind (Losno *et al.*, 1998). Overall, the bulk sampling can collect both the raindrops at the beginning of a rain event and locally produced aerosols. Then bulk sampling would result in the evaluation of wet deposition higher than that of wet-only sampling. However, the former fraction is a part of wet deposition, and the latter can be useful for tracing the local sources. Therefore, it can be expected that bulk sampling complements wet-only sampling when commencing long-term monitoring.

2.5. Summary

This chapter demonstrates the basic strategy of the rain sample collection with a case study at BARC. Manual rain samplers individually optimized for dissolved inorganic constituents and DOC were prepared and

applied for simultaneous sampling at three different sites at BARC in order to determine probable sources of the dissolved components and suggest a suitable site for the long-term monitoring of rainwater composition. The dissolved components could be explained by contributions from agricultural, marine biogenic and fossil fuel sources. The meter-scale spatial variation points to local factors that affect the rainwater composition, which can be mainly attributed to the formation of temporal rain shadow and input of locally produced aerosols depending on the local wind condition. Among three sites, Site BR1 is expected to be the most representative site adequate for the long-term monitoring at BARC station. However, the local influence at this site should be further assessed through a monitoring program.

2.6. References

- Andres, R.J., Marland, G., Fung, I., Matthews, E., 1996. A $1^{\circ} \times 1^{\circ}$ distribution of carbon dioxide emissions from fossil fuel consumption and cement manufacture, 1950-1990. *Global Biogeochemical Cycles*, 10(3), 419-429.
- Avery, G., Willey, J., Kieber, R., 2006. Carbon isotopic characterization of dissolved organic carbon in rainwater: Terrestrial and marine influences. *Atmospheric Environment*, 40(39), 7539-7545.
- Denman, K.L., Brasseur, G., Chidthaisong, A., Ciais, P., Cox, P.M., Dickinson, R.E., Hauglustaine, D., Heinze, C., Holland, E., Jacob, D., 2007.

Couplings between changes in the climate system and biogeochemistry. In: *Climate change 2007: The Physical Science Basis. Contribution of Working Group I to the Fourth Assessment Report of the Intergovernmental Panel on Climate Change* [Solomon, S. *et al.*(eds.)]. Cambridge University Press, Cambridge, United Kingdom and New York, NY, USA.

Draxler, R.R. and Rolph, G.D., 2012. HYSPLIT (HYbrid Single-Particle Lagrangian Integrated Trajectory) Model access via NOAA ARL READY Website (<http://ready.arl.noaa.gov/HYSPLIT.php>). NOAA Air Resources Laboratory, Silver Spring, MD, USA.

Hara, H., Shiozaki, T., 2011. Wet Deposition in East Asia. In: *The Second Periodic Report on the State of Acid Deposition in East Asia. Part I: Regional Assessment*. [Akimoto, H. *et al.*(eds.)]. Niigata-shi, Japan: Asia Center for Air Pollution Research.

Jacobson, M.C., Hansson, H.C., Noone, K.J., Charlson, R.J., 2000. Organic atmospheric aerosols: Review and state of the science. *Reviews of Geophysics*. 38(2), 267-294.

Kanakidou, M., Seinfeld, J., Pandis, S., Barnes, I., Dentener, F., Facchini, M., Van Dingenen, R., Ervens, B., Nenes, A., Nielsen, C., 2005. Organic aerosol and global climate modelling: a review. *Atmospheric Chemistry and Physics* 5(4), 1053-1123.

Kang, C.-H., Kim, W.-H., Lee, W., 2003. Chemical composition characteristics of precipitation at two sites in Jeju Island. *Bulletin of the Korean Chemical Society*, 24(3), 363-368.

- Kawamura, K., Kobayashi, M., Tsubonuma, N., Mochida, M., Watanabe, T. & Lee, M., 2004. Organic and inorganic compositions of marine aerosols from East Asia: Seasonal variations of water-soluble dicarboxylic acids, major ions, total carbon and nitrogen, and stable C and N isotopic composition. *The Geochemical Society Special Publications*, 9, 243-265.
- Kim, S.-B.K., Choi, B.-C.C., Oh, S.-Y.O., Kim, S.K., Kang, G.-U., 2006. Acidity and Chemical Composition of Precipitation at Background Area of the Korean Peninsula (Anmyeon, Uljin, Gosan). *Korean Society for Atmospheric Environment*, 22(1), 15-24.
- Lee, B.K., Hong, S.H., Lee, D.S., 2000. Chemical composition of precipitation and wet deposition of major ions on the Korean peninsula. *Atmospheric Environment*, 34(4), 563-575.
- Losno, R., Colin, J.L., Spokes, L., Jickells, T., Schulz, M., Rebers, A., Leermakers, M., Meuleman, C., Baeyens, W., 1998. Non-rain deposition significantly modifies rain samples at a coastal site. *Atmospheric Environment*, 32(20), 3445-3455.
- Luangjame, J., Sutamihardja, R.T.M., Majid, N.M., Sato, J., Yamashita, K., 2011. Introduction. In: *The Second Periodic Report on the State of Acid Deposition in East Asia. Part I: Regional Assessment*. [Akimoto, H. *et al.*(eds.)]. Niigata-shi, Japan: Asia Center for Air Pollution Research.
- Penner, J., Andreae, M., Annegarn, H., Barrie, L., Feichter, J., Hegg, D., Jayaraman, A., Leaitch, R., Murphy, D., Nganga, J., Pitari, G., 2001.

Aerosols, their Direct and Indirect Effects. In: *Climate Change 2001: The Scientific Basis. Contribution of Working Group I to the Third Assessment Report of the Intergovernmental Panel on Climate Change* [Houghton, J.T. *et al.*(eds.)]. Cambridge University Press, Cambridge, United Kingdom and New York, NY, USA.

Pilson, M.E.Q., 1998. *An Introduction to the Chemistry of the Sea*. Prentice Hall, New Jersey, USA, 431 pp.

Willey, J.D., Kieber, R.J., Eyman, M.S., Avery Jr, G.B., 2000. Rainwater dissolved organic carbon: Concentrations and global flux. *Global Biogeochemical Cycles* 14(1), 139-148.

Williams, P.M., Gordon, L.I., 1970. Carbon-13: carbon-12 ratios in dissolved and particulate organic matter in the sea. *Deep Sea Research and Oceanographic Abstracts*, 17(1), 19-27.

Yan, G., Kim, G., 2012. Dissolved organic carbon in the precipitation of Seoul, Korea: Implications for global wet depositional flux of fossil-fuel derived organic carbon. *Atmospheric Environment*, 59, 117-124.

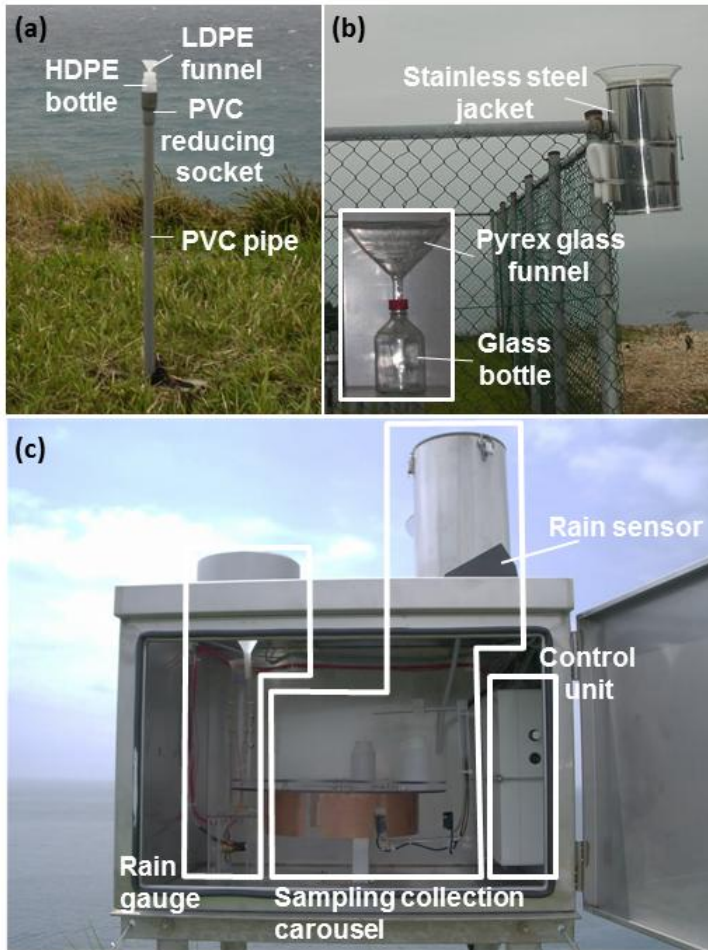


Figure 2-1. (a) The manual bulk rain sampler for major and trace elements and (b) organic carbon. (c) The automatic wet-only sampler.

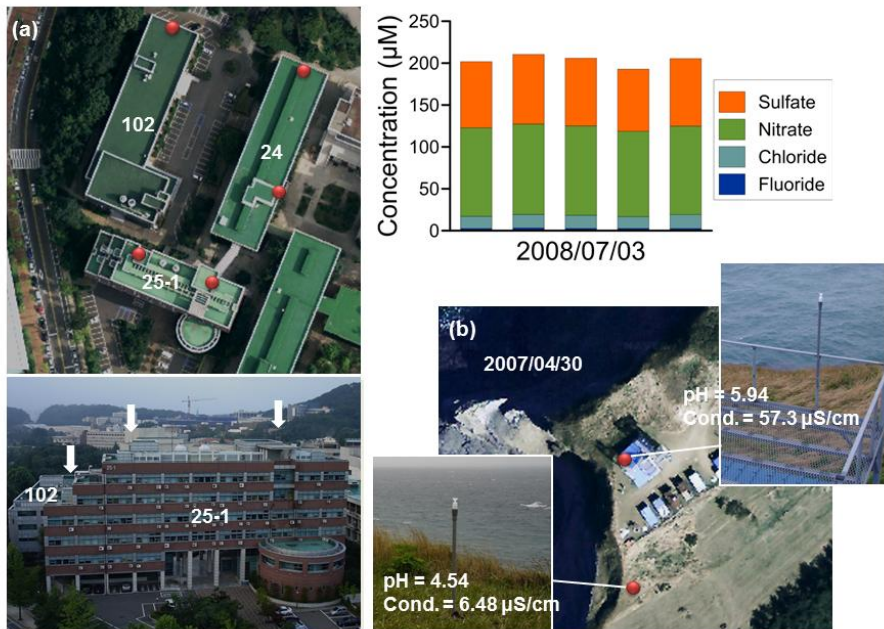


Figure 2-2. Preliminary results. (a) Anion composition of bulk rain samples collected on July 3 2008 at 5 different sites (red dots) at the Seoul National University campus sample. Building numbers are in white. In the bottom picture, 3 out of 5 sites are indicated by white arrows. Two sites on Building #24 are located behind Building #25-1. (b) The pH and conductivity (Cond.) of samples collected at two sites at Gosan Station on April 30, 2007.



Figure 2-3. Three sites (BR1, BR2 and BR3) within the Baengnyeongdo Atmospheric Research Center (BARC). BR3 is located in the backyard of the building. The white arrows indicate the location of bulk rain samplers.

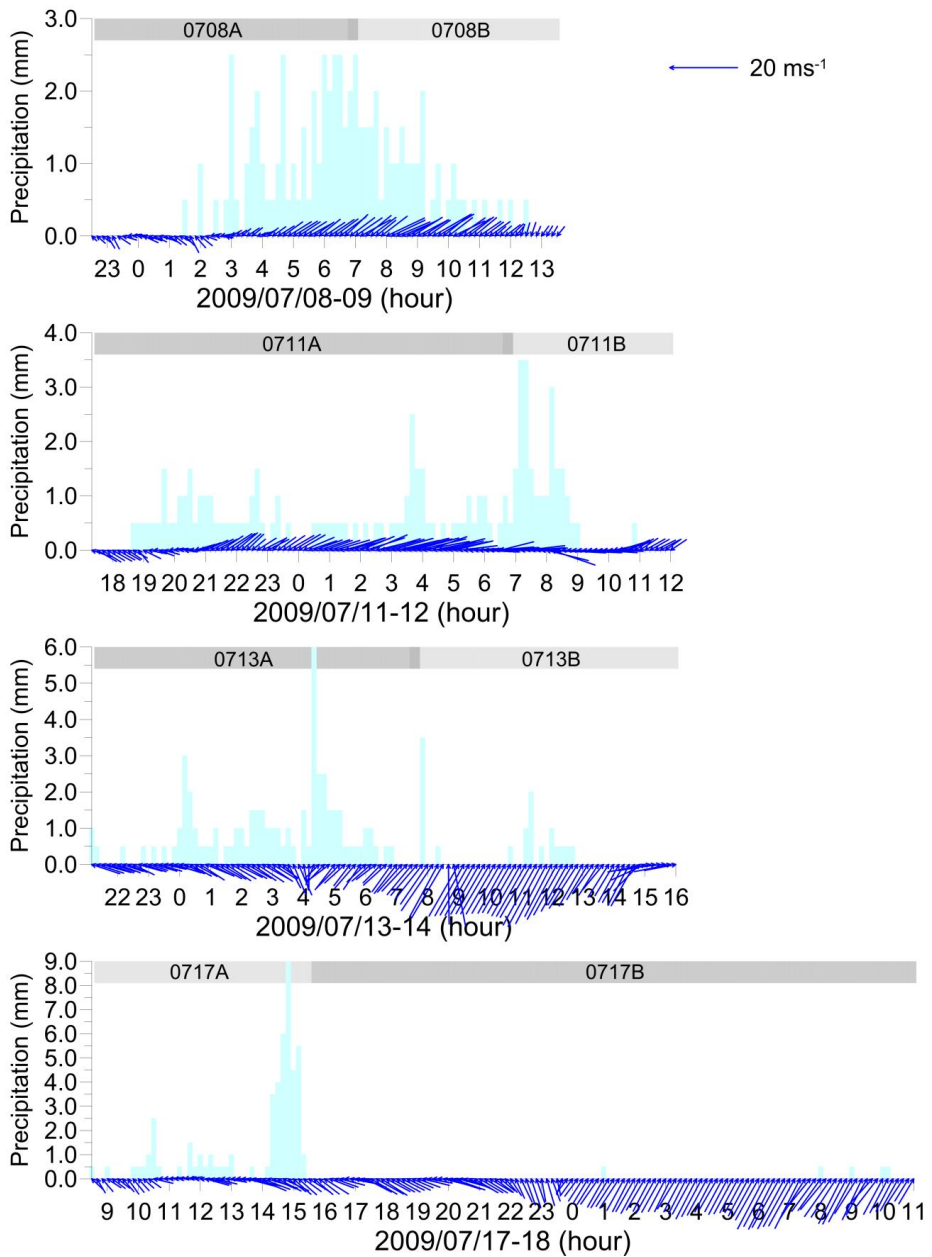


Figure 2-4. The precipitation (vertical bars) and wind direction and speed (blue arrows) for every 10 minutes during the rain sampling interval. The sampling duration for individual samples are denoted by horizontal bars – pale color for daytime samples and dark color for nighttime samples.

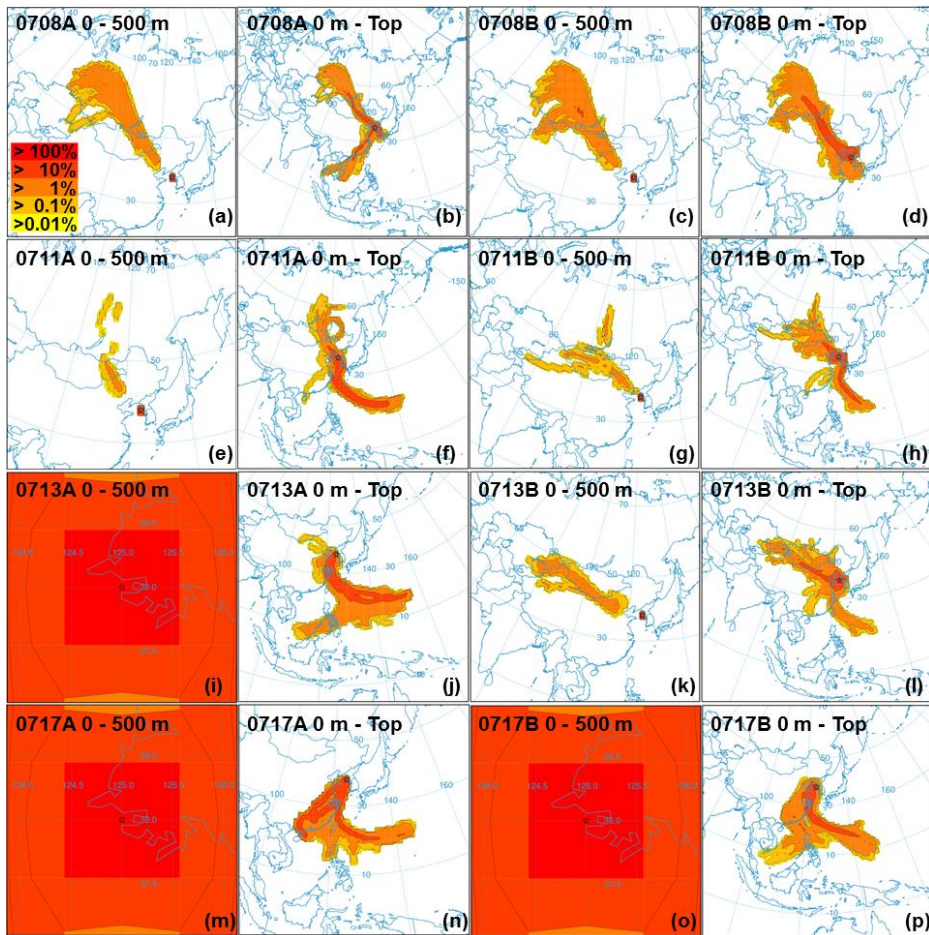


Figure 2-5. Five-day air-mass back trajectories for individual samples. The back trajectories calculated at 100, 500 and 1500 m above ground level are integrated from 0 to 500 m (1st and 3rd columns) and from 0 m to model top (10 km; 2nd and 4th columns) and depicted in the frequency distribution maps.

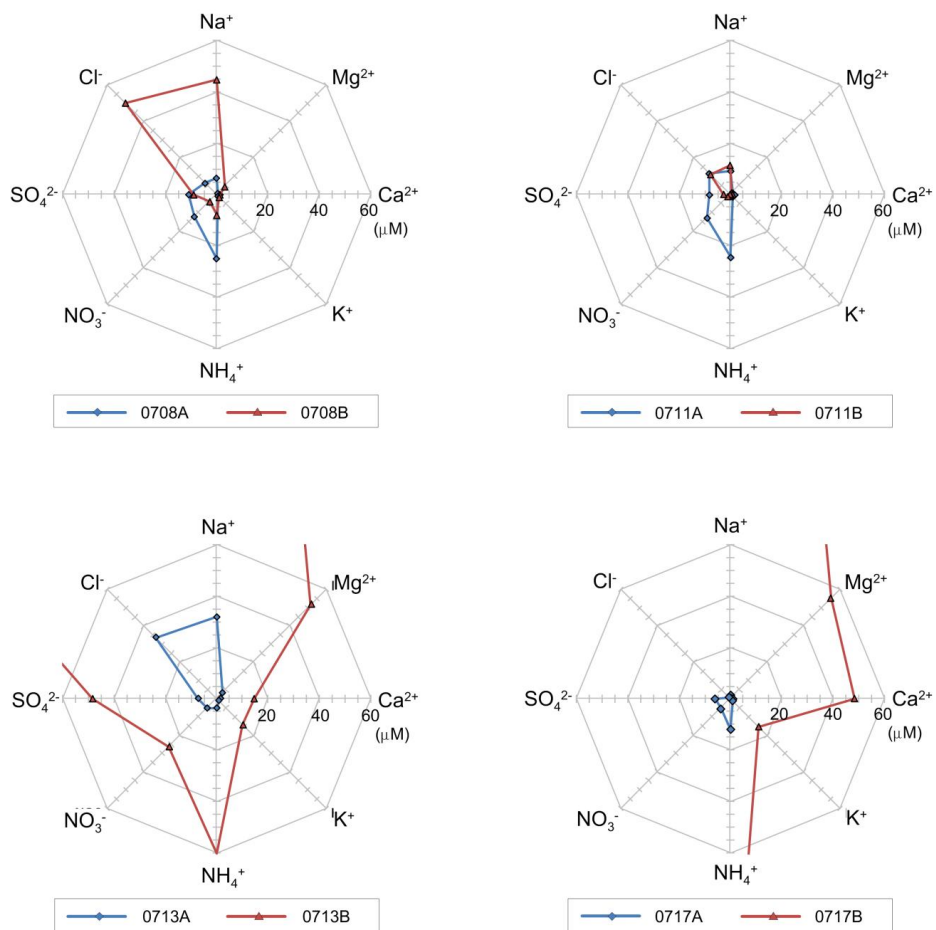


Figure 2-6. Radar charts for ionic compositions of the BARC samples. The blue diamond and red triangle indicate the first and second bottles, respectively, consecutively sampled in the continuous rain events. Some ions of the bulk samples (0713B and 0717B) are too high to be plotted. Each point is the mean of the three sites (BR1, BR2 and BR3).

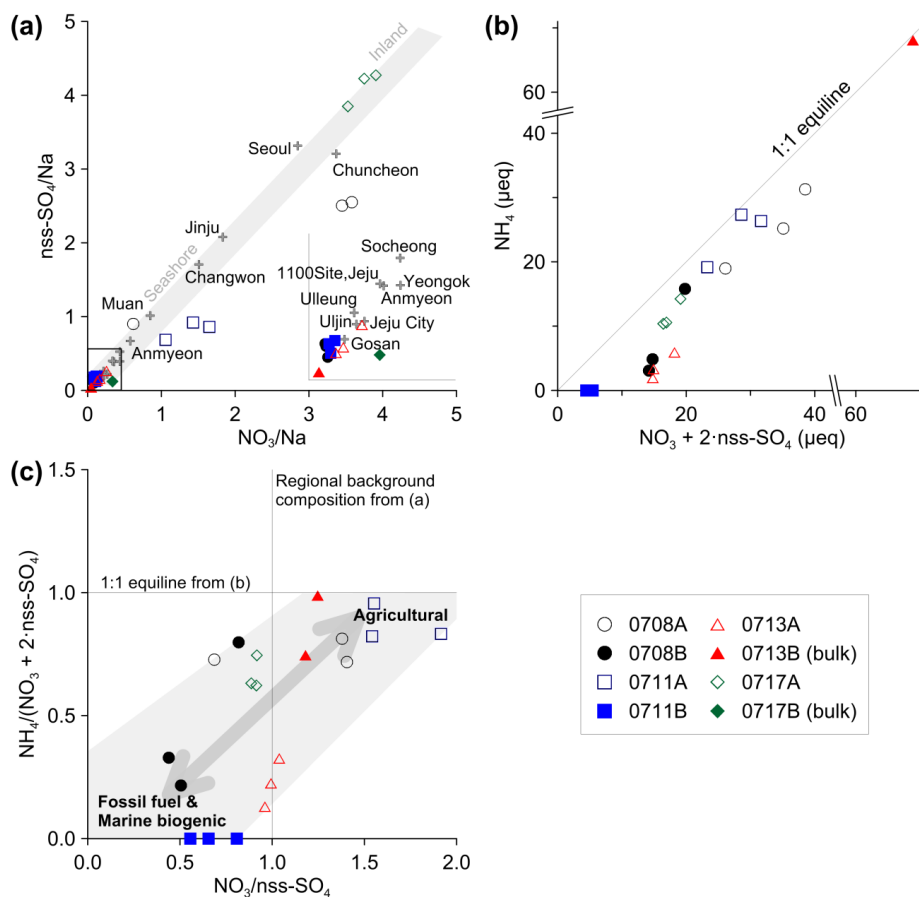


Figure 2-7. The ratios between inorganic components. (a) $\text{nss-SO}_4/\text{Na}$ vs. NO_3/Na molar ratios. The gray crosses indicate the rainwater composition at various sites in the Korea Peninsula, compiled from Kang *et al.* (2006), Kang *et al.* (2003) and Lee *et al.* (2000). The inset for the gray crosses enlarges near the origin. (b) $(\text{NO}_3 + 2 \cdot \text{nss-SO}_4)$ vs. NH_4 . One of the bulk samples, 0717B, was excluded due to its extreme composition. (c) $\text{NH}_4/(\text{NO}_3 + 2 \cdot \text{nss-SO}_4)$ vs. $\text{NO}_3/\text{nss-SO}_4$.

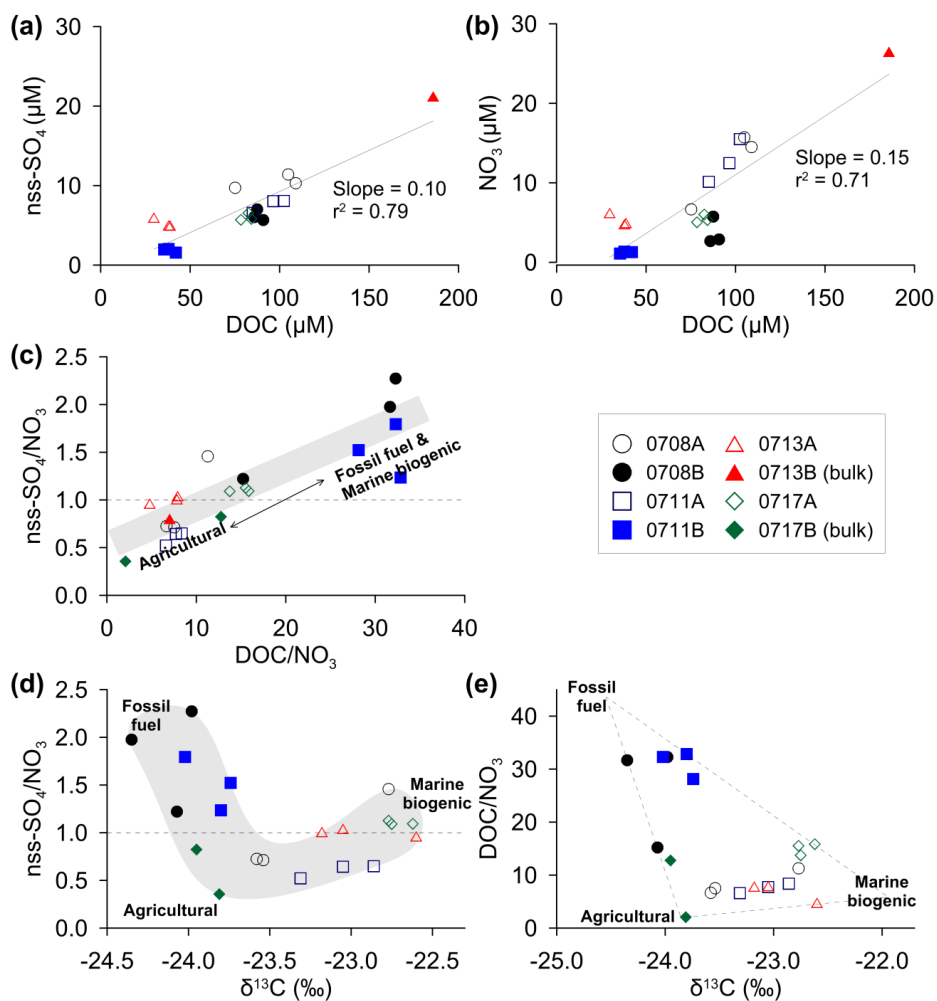


Figure 2-8. The relationship between the compositions of the dissolved organic carbon (DOC and $\delta^{13}\text{C}_{\text{DOC}}$) and inorganic constituents (nss-SO₄ and NO₃). (a - b) nss-SO₄ and NO₃ vs. DOC, (c) nss-SO₄ vs. DOC normalized by NO₃, (d) nss-SO₄/NO₃ vs. $\delta^{13}\text{C}_{\text{DOC}}$, and (e) DOC/NO₃ vs. $\delta^{13}\text{C}_{\text{DOC}}$ with tentative compositions of end-members for DOC.

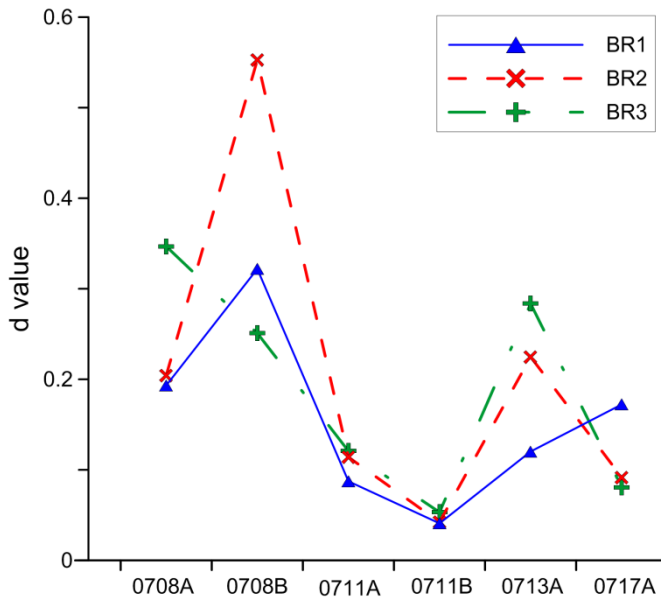


Figure 2-9. The variation of d value that means the degree to which each sampling site contributes to the spatial variation in the rainwater compositions. Site BR1 is the most representative location with comparatively lower d values.

Table 2-1. The dissolved major ion and organic carbon composition of rainwater samples at BARC in 2009.

Site	F (μM)	Cl (μM)	NO ₃ (μM)	SO ₄ (μM)	Na (μM)	K (μM)	Mg (μM)	Ca (μM)	NH ₄ (μM)	TZ ^{1a} (μeq)	TZ ^{2b} (μeq)	pH	Cond ^c ($\mu\text{S cm}^{-1}$)	ss-TZ ^d (%)	DOC (μM)	$\delta^{13}\text{C}_{\text{DOC}}$ (‰)	Precip ^e (mm)
0708A																	
BR1	bdl ^f	4.71	15.7	11.7	4.55	1.11	0.59	1.49	31.3	41.1	43.7	4.62	8.81	14	105	-23.6	28
BR2	bdl	3.59	14.5	10.6	4.05	0.74	0.51	1.72	25.2	34.5	39.2	4.58	9.50	13	109	-23.5	20
BR3	bdl	10.6	6.67	10.4	10.8	0.84	0.97	1.16	19.0	34.8	38.0	4.62	8.90	34	75	-22.8	>32
0708B																	
BR1	bdl	38.1	2.66	8.13	34.6	1.24	3.34	0.03	4.84	47.4	57.0	4.83	11.1	77	86	-24.0	20
BR2	bdl	74.2	5.75	10.9	63.9	1.96	6.54	2.39	15.8	99.5	102	6.03	13.3	76	88	-24.1	6
BR3	bdl	38.2	2.87	7.77	34.9	1.04	3.40	1.36	3.07	48.5	56.6	4.74	11.3	77	91	-24.4	16
0711A																	
BR1	bdl	8.6	12.5	8.57	8.74	0.93	1.00	1.51	27.3	42.0	38.2	4.39	12.3	25	97	-23.1	31
BR2	bdl	9.63	10.1	7.15	9.59	1.07	1.07	1.72	19.1	35.4	34.1	4.39	11.1	32	85	-22.9	23
BR3	bdl	16.9	15.5	8.65	9.38	1.12	1.04	1.47	26.4	41.9	49.7	4.35	11.8	33	102	-23.3	>32
0711B																	
BR1	bdl	10.5	1.35	2.71	10.8	0.71	0.85	1.02	bdl	15.3	17.2	5.46	3.19	73	38	-23.7	15
BR2	bdl	10.8	1.10	2.65	11.3	0.68	0.82	1.07	bdl	15.7	17.2	5.25	3.07	74	36	-24.0	12
BR3	bdl	11.9	1.28	2.32	12.2	0.72	1.00	1.04	bdl	17.0	17.8	5.26	3.45	76	42	-23.8	19
0713A																	
BR1	bdl	40.6	4.95	7.28	38.2	1.04	3.70	1.61	3.35	53.2	60.1	4.91	5.46	77	39	-23.2	>32
BR2	bdl	41.1	6.21	8.26	37.9	1.24	3.83	1.67	5.91	56.1	63.9	4.71	6.18	73	30	-22.6	>32
BR3	bdl	19.2	4.80	6.13	18.9	1.10	1.73	1.13	1.92	27.6	36.2	4.75	5.43	66	38	-23.1	>32
0713B (Bulk)																	
BR1	- ^g	-	-	-	-	-	-	-	-	-	-	4.42	267	-	-	-	-
BR2	0.58	669	26.5	54.0	544	17.1	64.6	16.4	68.0	792	805	4.36	88.3	84	186	-	12
BR3	0.57	400	25.9	42.5	340	11.4	38.8	12.3	52.0	506	512	4.34	81.6	81	-	-	7
0717A																	
BR1	bdl	1.13	6.01	6.66	1.70	0.75	0.34	0.92	14.2	19.2	20.5	4.68	6.99	10	83	-22.8	>32
BR2	bdl	0.82	5.05	5.78	1.35	1.09	0.23	0.80	10.4	14.9	17.4	4.62	7.09	10	78	-22.8	>32
BR3	bdl	0.86	5.31	5.89	1.36	1.11	0.22	0.81	10.6	15.1	18.0	4.63	6.99	10	84	-22.6	>32
0717B (Bulk)																	
BR1	-	-	-	-	-	-	-	-	-	-	-	4.74	580	-	-	-	1
BR2	0.57	399	25.9	42.5	-	-	-	-	-	-	510	4.51	158	-	330	-24.0	3
BR3	5.7	526	156	83.9	462	15.5	55.2	48.3	150	836	857	4.24	138	65	329	-23.8	3

^aTZ⁺=[Na⁺]+[K⁺]+2[Ca²⁺]+2[Mg²⁺]+[NH₄⁺]

^bTZ⁻=[F⁻]+[Cl⁻]+[NO₃⁻]+2[SO₄²⁻]

^cCond: conductivity

^dss-TZ (%) = (ss-TZ⁺ + ss-TZ⁻)/(TZ⁺ + TZ⁻) × 100, ss: sea salt

^ePrecip: precipitation

^fbdl : below detection limit

^g- : not measured

Table 2-2. The concentration of NO₃, nss-SO₄ and Na and their ratios monitored at various sites on the Korea Peninsula.

Site name ^a	NO ₃ (μM)	nss-SO ₄ (μM)	Na (μM)	NO ₃ /Na	nss-SO ₄ /Na	Period	Reference
Seoul	29.9	34.8	10.5	2.85	3.31		
Socheong	28.5	34.2	65.3	0.44	0.52		
Ulleung	20.9	25.3	96.7	0.22	0.26		
Chuncheon	23.6	22.5	7.0	3.37	3.21	1996. 5 - 1998. 4	Lee <i>et al.</i> , 2000
Changwon	17.5	19.8	11.6	1.51	1.71		
Anmyeon	17.9	20.8	31.0	0.58	0.67		
Yeongok	18.6	20.4	52.1	0.36	0.39		
Jinju ^b	19.8	22.5	10.8	1.83	2.08		
Muan	17.3	20.7	20.4	0.85	1.01	1997.3 - 1998.4	
1100Site	9.5	11.2	28.0	0.34	0.40	1997. 3 - 2002. 5	Kang <i>et al.</i> 2003
Jeju City	16.7	13.9	62.9	0.27	0.22	1996. 10 - 2002. 5	
Anmyeon	20.4	18.3	46.6	0.44	0.39	1997 - 2004	Kim <i>et al.</i> , 2006
Uljin	15.0	13.7	66.0	0.23	0.21	1998 - 2004	
Gosan	17.1	13.6	100.7	0.17	0.14	1998 - 2004	

^aAll site in the table are given in the current name.

^bThe old name was Chinyang.

Chapter 3

Assessing the impact of locally produced aerosol on the rainwater composition at Gosan background site in East Asia

*

Han Y., Huh Y., 2012. Assessing the impact of locally produced aerosol on the rainwater composition at Gosan background site in East Asia. *To be submitted*

Abstract: Monitoring the rainwater composition is a direct method for evaluating the regional wet deposition of airborne materials, but additional local contribution from the rain sampling site can exaggerate the wet deposition flux. We investigated the impact of locally produced aerosols on the rainwater composition and deposition fluxes of nitrate (NO_3^-), sulfate (SO_4^{2-}) and ammonium (NH_4^+) ions at Gosan Station, a background site in East Asia. In a 14-year record of rainwater composition, ionic ratios (NO_3/Na , SO_4/Na and NH_4/Na) were found to vary coherently with the wind direction. The relationship stems from the change in local aerosol source between western (sea) and eastern (farmland and grassland) areas. In addition, presence of the local influence is also supported by meter-scale spatial variability of rainwater composition in simultaneously collected samples and previously reported water-soluble ionic composition of airborne aerosol. We quantified the local influence in order to derive wet deposition flux from the background atmosphere.

Key words: wet deposition, rainwater chemistry, ionic ratio, background atmosphere

3.1. Introduction

Atmospheric precipitation plays an important role in the removal of airborne materials from the atmosphere. During several decades, environmental and climatological concerns about increasing anthropogenic emission have prompted studies on the rainwater composition associated with the air pollution and acid deposition (Rodhe *et al.*, 2002) and the deposition of aerosols that produce direct/indirect effects on radiative forcing (Granat *et al.*, 2010). Monitoring rainwater composition is useful for tracing the source of aerosols and soluble gases and their transport on a regional scale (Granat *et al.*, 2002). For instance, the Acid Deposition Monitoring Network in East Asia (EANET) and the European Monitoring and Evaluation Programme (EMEP) have operated networks for monitoring the rainwater composition in East Asia and Europe, respectively, in order to assess regional atmospheric pollution and trans-boundary transport of pollutants. Additionally, data from the monitoring program can be used to validate computer-based acid deposition models (Wang *et al.*, 2008).

A remote rural site is generally preferred when monitoring wet deposition from the regional background atmosphere, because it can avoid local influence (Das *et al.*, 2010; Das *et al.*, 2011; Laouali *et al.*, 2012). In Das *et al.* (2011) and Granat *et al.* (2010), for example, Hanimadhoo island in Maldives was selected as a strategic location for monitoring transport from South Asia and the southern Indian Ocean. At this site, local influence was

neglected based on subdued topography (<3 m), low population (~1,200) and absence of local industry. However, even at such a remote site, various factors related to the sampling strategy can affect the rainwater composition: e.g., the collector type (bulk or wet-only), collector position and height above ground, surrounding topography and surface type (e.g., land/sea, open soil, grass, concrete, and architecture) and local wind conditions. In general, a wet-only collector installed at a higher elevation is preferred for reducing input of wind-drifted particles from the underlying surface (Kulshrestha *et al.*, 1995). Based on the simultaneous sampling at different heights, it is suggested that a height of several tens to a few hundred meters may be required to be free from the input of locally wind-drifted particles (Kulshrestha *et al.*, 2005), but maintaining a rain collector at such heights is not practical in the ground-based rain sampling.

The influence of local sources would be more severe in a windy area where strong winds are liable to stir up more particles from the surface. This was highlighted by simultaneous rain sampling at multiple positions on a windy coastal site (Losno *et al.*, 1998), from which it was observed that the concentrations of sea-salt components in rainwater and their spatial variability increased with wind speed. This was due to uneven inputs of wind-driven marine aerosols, which was produced from the nearby sea surface and introduced into individual collectors before being homogeneously dispersed in the air. In the case, the evaluation of wet deposition would include wet scavenging and dry deposition of locally produced marine aerosols.

If it is the wet deposition representative of a regional scale that is of

interest, local influences can lead to overestimation and hence should be carefully assessed. One way to cope with this problem is to test the spatial distribution of rainwater composition with multiple sampling at meter- to hundred-meter-scale (Kulshrestha *et al.*, 2005). However, it would be impractical for long-term monitoring to maintain multiple collectors. Instead, in this study, an attempt is made to detect the local influence from a 14-year data set of dissolved ion composition acquired by using a single wet-only collector at Gosan Station in Jeju Island, Korea. Gosan Station, a remote island site, was previously suggested as a suitable location for monitoring the regional background atmosphere and continental outflow in East Asia (Carmichael *et al.*, 1997; Chuang *et al.*, 2003). Moreover, this site is expected to be ideal for examining the local influence, because its location on the western tip of the island provides a marked contrast in the surrounding surface types (Fig. 3-1) – the sea to the west and farmland or grassland to the east. In addition to marine aerosol that would dominate the coastal site, the eastern cultivated region would act as a local source of terrestrial aerosols like nitrate (NO_3^-), non-sea-salt sulfate (nss-SO_4^{2-}) and ammonium (NH_4^+). If local aerosols are produced by the wind, then they would differently influence the rainwater composition depending on wind direction. Here, we present evidences that locally produced aerosols do indeed affect the rainwater composition and propose a quantitative assessment. This scheme allows researchers to better characterize the wet deposition flux representative of the regional background atmosphere.

3.2. Method

3.2.1. Study area

In Gosan Station (33.292°N, 126.162°E), located on top of a ~70 m cliff on the western coast of the island, several atmospheric monitoring devices have been installed in and on the rooftops (3 – 4 m heights above the ground) of shipping containers, and on two tower platforms 10 m and 15 m high (Fig. 3-1). The mean annual precipitation is about 1100 mm, about half of which falls during the summer season. This coastal site is windy with a mean speed of 7.0 m s^{-1} . Land use around the site is primarily agricultural with little grassland and trees. There are two small villages near the site, 0.5 km to the southeast and 2 km to the northeast, with less than 600 residents in each.

3.2.2. Rainwater chemistry data base and meteorological data

The rainwater chemistry data set at Gosan Station was provided by the Korea Meteorological Administration (KMA). It includes precipitation (mm), electrical conductivity ($\mu\text{S cm}^{-1}$), pH, and concentration ($\mu\text{mol L}^{-1}$) of major ions (F^- , Cl^- , NO_3^- , SO_4^{2-} , Na^+ , NH_4^+ , K^+ , Mg^{2+} , Ca^{2+}). The data set covers the period from October 1998 to December 2011, during which 540 individual rain samples were collected by a wet-only collector on a daily basis at 09:00 a.m. The position of the collector is shown in Fig. 3-1. The mouth of the collector is at ~1 m height from the ground. The non-sea-salt sulfate (nss-

SO_4^{2-}) concentration is calculated using $\text{nss-SO}_4^{2-} (\mu\text{mol L}^{-1}) = \text{SO}_4^{2-} - 0.06028 \times \text{Na}^+$ (EANET, 2012).

The mean wind direction and speed during rain events are derived from automatic weather station (AWS) data, archived by KMA from October 1999 to present. The AWS data set includes the 10-minute mean wind direction (degree) and speed (m s^{-1}), daily cumulative precipitation (mm) and rain sensing signal (whether it is raining or not) for every 10-minute interval. Since the wet-only rain collector opens its lid only while the rain sensor was actuated, the wind direction and speed are averaged only for the ‘raining’ intervals. This calculation was carried out on the 493 (out of 540) samples, for which the AWS data were available.

The air mass back trajectory analysis was conducted using NOAA/HYSPLIT (National Oceanic and Atmospheric Administration/hybrid single-particle Lagrangian integrated trajectory) model (Draxler and Hess, 1997) and meteorological data from NCEP/GDAS (National Centers for Environmental Prediction/global data assimilation system) available from December 2004.

3.2.3. Simultaneous rain sampling

To test the effect of locally produced aerosols on the meter-scale variability of rainwater composition, two rain events on April 22 and 27, 2008 (GS22 and GS27, hereafter) were sampled simultaneously at four sites at Gosan Station: on two tower platforms of 15 m (T1) and 10 m (T2) height, and two ground sites <20 m from the tower platforms (F1, F2) (Fig. 3-1).

Identical bulk samplers were installed 1 - 2 m above the surfaces of tower platforms and ground to reduce splashed rain input. The samples were immediately frozen and transferred to the laboratory at Seoul National University. After melting, samples were filtered through 0.2 μm Nylon syringe filters. After discarding the first 0.5 mL, the filtered rainwater was stored in pre-cleaned HDPE bottles. Next, to prevent microbial growth, thymol was added to the final concentration of 0.4 $\mu\text{g L}^{-1}$ (Granat *et al.*, 2001), which did not affect the determination of major ion concentrations. Samples were then stored in a refrigerator until analysis. Sample handling was performed within laminar flow clean benches/hoods to minimize contamination. The sampling procedure is also described in Soyol-Erdene *et al.* (2011a).

Major ionic concentrations were determined by ion chromatography (IC, ICS2000, Dionex) at Seoul National University. Cation (Na^+ , K^+ , Ca^{2+} , Mg^{2+}) contents were also determined by inductively-coupled plasma atomic emission spectrometer (ICP-AES, Optima-4300 DV, PerkinElmer) at Korea Basic Science Institute. The internal precision for all measurements was less than 10% (relative standard deviation, RSD). Accuracy was tested with two certified reference materials, BCR-CRM 408 (simulated rainwater, low contents) and SLRS-4 (river water), and we obtained the results within 10% of the certified values. The ICP-AES results agreed well with the IC results within 8.5% except a potassium result (17.6%) of GS27-T1 with very low potassium content.

3.3. Results and discussion

3.3.1. NO_3/Na ratio as a proxy for local influence

The compositional distinction between marine and terrestrial aerosols allows the use of NO_3/Na ratio as a proxy for the locally produced aerosols at Gosan Station (Fig 3-S1). Against primitive NO_3/Na ratio reflecting the long-range transport and, in turn, the background atmosphere, the marine aerosols depleted in nitrate ($\text{NO}_3/\text{Na} < 10^{-4}$, molar ratio hereafter; Parungo *et al.*, 1987) would lower the ratio, whereas potential nitrate input from the eastern cultivated region could increase it. Then the local influence would give rise to variation in the NO_3/Na ratio depending on the wind direction as the westerly (easterly) decreases (increase) the ratio. Furthermore, the wind directional variability of the rainwater composition would be deepened by stronger wind speed that can produce and transport more local aerosols.

To explore the relationship between the wind direction and NO_3/Na ratio, the wind direction was divided into eight sectors of 45° each (I – VIII; Fig.3-1), taking into consideration the positions of adjacent buildings and structures that can act as windbreaks. The NO_3/Na ratios are treated in two different ways: (1) the mean NO_3/Na ratios and (2) frequency of NO_3/Na “peaks” above a threshold (1.302; mean + 3s.d) are calculated for each wind sector (Fig. 3-2). As expected, the NO_3/Na ratio was highly dependent on the wind direction. The land sectors (III, IV and V) had higher mean NO_3/Na ratios and more frequent NO_3/Na peak events compared to the sea sectors of (VII and VIII) (Fig. 3-2), suggesting that the eastern land and western sea

represent additional local sources of NO_3^- and Na^+ , respectively. The sectors I and II exhibit the intermediate mean values and peak frequencies, which can be partly attributed to the blocking effect by the contiguous building.

Fig. 3-3 displays show NO_3/Na varies with wind speed. The NO_3/Na ratios decrease with wind speed not only for the sea sectors but also for the land sectors. This indicates that the local production of marine aerosols increase with strong wind and the sea surface is still the dominant source for the local aerosols at the island site regardless of wind direction. Nevertheless, relatively high NO_3/Na ratios happen below 7.5 m s^{-1} , indicating that the local contribution of NO_3 surpasses that of Na. Overall, the dependence of the NO_3/Na ratio on wind speed supports the local production of aerosols by wind. Moreover, the transition of the peak frequency at $6 - 7.5 \text{ m s}^{-1}$ reflects incremental contribution of marine aerosols over terrestrial aerosols. In this case, the extent of the “local” area can be though to enlarge with stronger wind, and marine aerosol can be derived from farther sea surface.

The air mass back trajectory analysis was performed for events with NO_3/Na peaks to attest that these peaks did not result from the long-range transport. For the 43 peak events (out of 48) for which GDAS meteorological data were available, 3-day back trajectories with starting heights of 50, 500 and 1500 m above ground levels were calculated at 3 hour intervals. The results were illustrated by means of frequencies of intersection between each map grid cell (0.25×0.25 degree) and the trajectories projected on the map (Fig. 3-4). No source region or preferred air flow pathway could be identified for the NO_3/Na peak events (Fig. 3-4), supporting that the peak events took

place at the local scale.

When applying the same calculation with SO_4/Na and NH_4/Na ratios, dependence on the wind direction was also observed (Fig. 3-2). Their coherent trends with NO_3/Na can be explained by that (1) these three ratios are commonly controlled by local Na^+ input, (2) the eastern cultivated area supplied nss-SO_4^{2-} and NH_4^+ as well as NO_3^- , or both. Since ammonium nitrate and ammonium sulfate are the major constituents of fertilizers, the agriculture may be a common source of NO_3^- , SO_4^{2-} and NH_4^+ . However, the wind directional variability decreases in the order of NO_3/NH_4 , $\text{nss-SO}_4/\text{NH}_4$ and $\text{NO}_3/\text{nss-SO}_4$ (Fig. 3-5). This implies that local inputs of NO_3^- surpass those of nss-SO_4^{2-} of NH_4^+ . This will be further discussed in Section 3.3.

3.3.2. Meter-scale spatial variability of rainwater composition

The two sets of simultaneous samples (GS22 and GS27) with the contrasting wind conditions and ion contents provide an opportunity to examine the influence of wind direction on the rainwater composition. Event GS22 was dominated by strong winds from the seaward sectors (VIII to I) and winds from the inland sector (IV) prevailed during event GS27 (Fig. 3-6). GS27 had significantly higher ion contents than GS22, with average TZ^- of $956 \mu\text{eq L}^{-1}$ and $254 \mu\text{eq L}^{-1}$, respectively. The concentrations of the individual ions were also higher in GS27, especially for SO_4^{2-} and NO_3^- .

A plot of NO_3/Na vs. $\text{nss-SO}_4/\text{Na}$ is useful for illustrating the relative contributions of the marine and terrestrial inputs (Fig. 3-7). This can be verified by compiling rainwater composition monitored at various sites in

Korea (Kang *et al.*, 2003; Kim *et al.*, 2006; Lee *et al.*, 2000). In Fig. 3-7, the coastal sites plot near the origin due to the abundant input of marine aerosols, and an increase of the terrestrial contribution in the inland sites elevates those ratios along a line with a slope of ~ 1 . The good linearity between those ratios qualifies these ratios as a useful tool in assessing the relative contributions of the sea and land. In addition, it would point to a primary source of nss-SO_4^{2-} and NO_3^- in the Korea Peninsula, characterized by their ratio ~ 1 .

GS27 are shown to have larger spatial variability of the ionic ratios than GS22 (Fig. 3-7). As expected from the wind direction, GS22 lie near the origin due to the large influence of marine aerosol (Fig. 3-7). On the contrary, GS27 have a wide range of both $\text{nss-SO}_4/\text{Na}$ and NO_3/Na ratios highlighting meter-scale variability of rainwater composition. This would result from uneven contributions of locally produced aerosols to individual rain collectors due to different sampling conditions of each collector – i.e. the rain collector height and the adjacent buildings and towers. For example, the effect of the sampling height can be inferred from the observation that the $\text{nss-SO}_4/\text{Na}$ and NO_3/Na ratios increase in the order of T2-T1-F1-F2 in GS27. This means that the ground sites (F1 and F2), compared to the tower sites (T1 and T2), are more liable to be affected by locally produced aerosols marked by similar $\text{nss-SO}_4/\text{NO}_3$ ratio as the background composition (~ 1) in the Korea peninsula. On the other hand, the buildings (2 – 3 m heights) or towers (10 and 15 m heights) neighboring the collectors can form temporal rain shadow depending to the wind conditions and lead to the spatial variance in the amount of precipitation and hence the rainwater composition. In addition, rain splash on the face of

the buildings and towers can influence the rainwater composition. For instance, GS27-T1 and T2 have higher Ca^{2+} than F1 and F2, which cannot be explained by the rain shadow. The excess Ca^{2+} might be sourced from anticorrosive chemicals or accumulated salts on the surface of the tower platforms themselves.

3.3.3. Comparison to aerosol composition data

To check whether the interpretation of the local influence in the rainwater composition is compatible with the atmospheric aerosols composition, previously reported data were compiled for water-soluble components (Na^+ , NO_3^- , SO_4^{2-} and NH_4^+) of total suspended particulates (Table 3-1). In Gosan Station, interestingly, there are parallel data sets obtained respectively at the heights of 3 and 6 m, in which the ion concentrations are generally higher at 3 m than at 6 m. This is consistent with what can be expected from the local influence, because local aerosols are produced from the surfaces of the sea and ground and would be more influential to the lower elevation site. To test how much the relative abundance of the individual ions depends on the sampling height, the ion ratios at the two heights are compared each other (Fig. 3-8). When normalized by sodium, NO_3/Na was higher at the lower elevation site whereas $\text{nss-SO}_4/\text{Na}$ and NH_4/Na were lower (Fig. 3-8a). In addition, $\text{NO}_3/\text{nss-SO}_4$ and NO_3/NH_4 are higher at the lower site (Fig. 3-8b). These imply that the increase of NO_3^- concentration toward the ground level is greater than those of nss-SO_4 and NH_4 . The higher relative abundance of NO_3^- at the lower site can

be explained by a greater association of NO_3^- with larger particles than nss-SO_4^{2-} and NH_4^+ , because larger particles would be blown up lower, settle down faster than smaller particles and hence be relatively abundant near the surface. In another study for the aerosol size distribution of the water-soluble ions at Gosan Station, $\text{NO}_3^-/\text{NH}_4^+$ and $\text{NO}_3^-/\text{nss-SO}_4^{2-}$ ratios were shown to increase with the particle size – 0.16 and 0.25 ($\text{PM}_{1.0}$), 0.25 and 0.34 ($\text{PM}_{2.5}$), and 0.48 and 0.69 (PM_{10}) (Lim *et al.*, 2012), supporting the NO_3^- associative with larger particles.

It is likely that the averaged ionic ratios of the rainwater maintain the tendency of those of the aerosols, although the rainwater composition should be carefully compared with the aerosol composition (Fig. 3-8). It is shown from the wind directional variability of $\text{NO}_3^-/\text{NH}_4^+$ and $\text{nss-SO}_4^{2-}/\text{NH}_4^+$ ratios in the rainwater composition (Fig. 3-5) that the local contribution for NO_3^- and is superior to those of nss-SO_4^{2-} and NH_4^+ . This is congruent with the aerosol composition data that show the association of NO_3^- with larger particles preferable for the deposition into the rain collectors.

3.3.4. Significance of the local influence on the wet deposition flux

It is necessary to discriminate the local influence from the measured value in order to evaluate the wet deposition that represents the background atmosphere. For the calculation, we introduce following notations:

$$F = F_B + F_L \text{ and } f = F_B / F,$$

where F is the measured wet deposition flux (mol m^{-2} , concentration [mol m^{-3}] \times precipitation [m]), is the sum of the background flux (F_B) and the local

influence (F_L), and f is a correction factor defined by the fraction of the background flux in the total flux. Then, the background fluxes of Na^+ , NO_3^- , SO_4^{2-} and NH_4^+ and their ratios can be expressed as:

$$F_{i,B} = f_i \times F_i \text{ and } \frac{F_{i_1,B}}{F_{i_2,B}} = \left(\frac{f_{i_1}}{f_{i_2}} \right) / \left(\frac{F_{i_1}}{F_{i_2}} \right) \text{ (} i \text{ is Na, NO}_3\text{, SO}_4 \text{ or NH}_4\text{)}.$$

Since the flux ratio is equal to the molar ratio, F_{i_1}/F_{i_2} can be replaced by the measured molar ratio and $F_{i_1,B}/F_{i_2,B}$ represents the background molar ratio of i_1/i_2 (e.g., NO_3/Na). We speculate that $F_{i_1,B}/F_{i_2,B}$ is independent of the local wind direction by assuming the local influence F_L as the portion that has the wind directional variability, which is used as a rule of thumb for finding the best correction factors (f_i).

The correction factors are optimized using a genetic algorithm (GA) from the Matlab Optimization Toolbox 6.2. Initial correction factors of f_{NO_3} , f_{SO_4} , f_{NH_3} and f_{Na} set randomly between 0 and 1 evolve to the optima satisfying the following conditions for mitigating the wind direction variability: (1) The mean $F_{i_1,B}/F_{i_2,B}$ ratios and (2) total flux ratio ($\sum F_{i_1,B} / \sum F_{i_2,B}$) of each wind sector coincide within predefined level (x-axis in Fig. 3-9) (3) with minimal corrections (maximum $\sum F_{i,B} / \sum F_i$). These conditions allow for evaluating the lower limit of the local influence. The optimization result is shown in Fig. 3-9. When 5% of the wind directional variability between the wind sectors is allowed for the natural variation of the background flux, it is estimated that 10% of nitrogen (N; $\text{NO}_3^- + \text{NH}_4^+$) and 12% of sulfur (S; nss-SO_4^{2-}) have the local origin. If wider variability is permitted,

the local influence is reduced and more portions are assigned to the background flux. However, it should be noted that these modeled values represent the minimum local influence. For example, we do not consider observations of the particle size distribution of the ions and the effect of the wind speed, in order to retain the simplicity of the model calculation.

3.4. Conclusion

We could discern the impact of the local influence on the dissolved ion composition of rainwater monitored for ~14 years at Gosan Station and correct it in order to evaluate the wet deposition from the background atmosphere. As a proxy for the local influence, NO_3/Na ratio displayed the wind directional variability as a consequence of selective transport of NO_3^- from the land or Na^+ from the sea according to the wind direction, which was also observed for SO_4/Na and NH_4/Na ratios. It was also shown that the aerosol drift at a local scale could lead to the meter-scale spatial variability of the rainwater composition in the simultaneous collected samples and compositional heterogeneity in aerosol simultaneously monitored at different heights. To reduce the wind directional variability within 5%, at least ~10% of nitrogen and ~12% of sulfur in their measured wet deposition fluxes should be attributed to the local influence. We suggest that these fractions at least should be corrected in order to evaluate their regional background fluxes.

3.5. References

- Carmichael, G.R., Hong, M.S., Ueda, H., Chen, L.L., Murano, K., Park, J.K., Lee, H., Kim, Y., Kang, C., Shim, S., 1997. Aerosol composition at Cheju Island, Korea. *Journal of Geophysical Research D: Atmospheres* 102(5), 6047-6061.
- Chuang, P.Y., Duvall, R.M., Bae, M.S., Jefferson, A., Schauer, J.J., Yang, H., Yu, J.Z., Kim, J., 2003. Observations of elemental carbon and absorption during ACE-Asia and implications for aerosol radiative properties and climate forcing. *J. Geophys. Res.* 108(D23), 8634.
- Das, N., Das, R., Chaudhury, G.R., Das, S.N., 2010. Chemical composition of precipitation at background level. *Atmospheric Research* 95(1), 108-113.
- Das, R., Granat, L., Leck, C., Praveen, P.S., Rodhe, H., 2011. Chemical composition of rainwater at Maldives Climate Observatory at Hanimaadhoo (MCOH). *Atmos. Chem. Phys.* 11(8), 3743-3755.
- Draxler, R.R., Hess, G.D., 1997. Description of the HYSPLIT_4 Modeling System, NOAA, Silver Spring, Md.
- EANET, 2012. Data Report on the Acid Deposition in the East Asian Region 2010, Asia Center for Air Pollution Research (ACAP), Niigata-shi, Japan.
- Granat, L., Das, S., Tharkur, R., Rodhe, H., 2001. Atmospheric deposition in a rural area in India-net and potential acidity. *Water, Air, & Soil*

Pollution 130(1), 469-474.

Granat, L., Engström, J.E., Praveen, S., Rodhe, H., 2010. Light absorbing material (soot) in rainwater and in aerosol particles in the Maldives. *J. Geophys. Res.* 115(D16), D16307.

Granat, L., Norman, M., Leck, C., Kulshrestha, U.C., Rodhe, H., 2002. Wet scavenging of sulfur compounds and other constituents during the Indian Ocean Experiment (INDOEX). *J. Geophys. Res.* 107(D19), 8025.

Kang, C.H., Kim, W.H., Lee, W., 2003. Chemical composition characteristics of precipitation at two sites in Jeju Island. *BULLETIN-KOREAN CHEMICAL SOCIETY* 24(3), 363-368.

Kawamura, K., Kobayashi, M., Tsubonuma, N., Mochida, M., Watanabe, T., Lee, M., 2004. Organic and inorganic compositions of marine aerosols from East Asia: Seasonal variations of water-soluble dicarboxylic acids, major ions, total carbon and nitrogen, and stable C and N isotopic composition, in: Ronald J. Hill, J.L.Z.A.M.J.B.G.C.R.E.M.G., Kenneth, P. (Eds.), *The Geochemical Society Special Publications*. Elsevier, pp. 243-265.

Kim, S.-B.K., Choi, B.-C.C., Oh, S.-Y.O., Kim, S.K., Kang, G.-U., 2006. Acidity and Chemical Composition of Precipitation at Background Area of the Korean Peninsula (Anmyeon, Uljin, Gosan). *Korean Society for Atmospheric Environment* 22(1), 15-24.

Kulshrestha, U.C., Granat, L., Engardt, M., Rodhe, H., 2005. Review of precipitation monitoring studies in India—a search for regional

- patterns. *Atmospheric Environment* 39(38), 7403-7419.
- Kulshrestha, U.C., Sarkar, A.K., Srivastava, S.S., Parashar, D.C., 1995. Wet-only and bulk deposition studies at New Delhi (India). *Water, Air, & Soil Pollution* 85(4), 2137-2142.
- Kundu, S., Kawamura, K., Lee, M., 2010. Seasonal variation of the concentrations of nitrogenous species and their nitrogen isotopic ratios in aerosols at Gosan, Jeju Island: Implications for atmospheric processing and source changes of aerosols. *J. Geophys. Res.* 115(D20), D20305.
- Laouali, D., Galy-Lacaux, C., Diop, B., Delon, C., Orange, D., Lacaux, J.P., Akpo, A., Lavenu, F., Gardrat, E., Castera, P., 2012. Long term monitoring of the chemical composition of precipitation and wet deposition fluxes over three Sahelian savannas. *Atmospheric Environment* 50(0), 314-327.
- Lee, B.K., Hong, S.H., Lee, D.S., 2000. Chemical composition of precipitation and wet deposition of major ions on the Korean peninsula. *Atmospheric Environment* 34(4), 563-575.
- Lee, S.-B., Kang, C.-H., Jung, D.-S., Ko, H.-J., Kim, H.-B., Oh, Y.-S., Kang, H.-L., 2010. Composition and pollution characteristics of TSP, PM_{2.5} atmospheric aerosols at Gosan site, Jeju Island. *Analytical Science & Technology* 23(4), 372-382.
- Lim, S., Lee, M., Lee, G., Kim, S., Yoon, S., Kang, K., 2012. Ionic and carbonaceous compositions of PM₁₀, PM_{2.5} and PM_{1.0} at Gosan ABC Superstation and their ratios as source signature. *Atmos. Chem.*

Phys. 12(4), 2007-2024.

Losno, R., Colin, J.L., Spokes, L., Jickells, T., Schulz, M., Rebers, A., Leermakers, M., Meuleman, C., Baeyens, W., 1998. Non-rain deposition significantly modifies rain samples at a coastal site. *Atmospheric Environment* 32(20), 3445-3455.

Park, M.H., 2003. A study on long-term characteristics of ion composition and transport pattern of aerosol at Gosan, Korea, Ewha Womans University, Seoul, Korea.

Parungo, F.P., Nagamoto, C.T., Madel, R., Rosinski, J., Haagenson, P.L., 1987. Marine aerosols in Pacific upwelling regions. *Journal of Aerosol Science* 18(3), 277-290.

Rodhe, H., Dentener, F., Schulz, M., 2002. The Global Distribution of Acidifying Wet Deposition. *Environmental Science & Technology* 36(20), 4382-4388.

Soyol-Erdene, T.-O., Han, Y., Lee, B., Huh, Y., 2011. Sources and fluxes of Pb, Ir and REE in the Seoul metropolitan area through wet scavenging processes. *Atmospheric Environment* 45(11), 1970-1978.

Wang, Z., Xie, F., Sakurai, T., Ueda, H., Han, Z., Carmichael, G.R., Streets, D., Engardt, M., Holloway, T., Hayami, H., Kajino, M., Thongboonchoo, N., Bennet, C., Park, S.U., Fung, C., Chang, A., Sartelet, K., Amann, M., 2008. MICS-Asia II: Model inter-comparison and evaluation of acid deposition. *Atmospheric Environment* 42(15), 3528-3542.

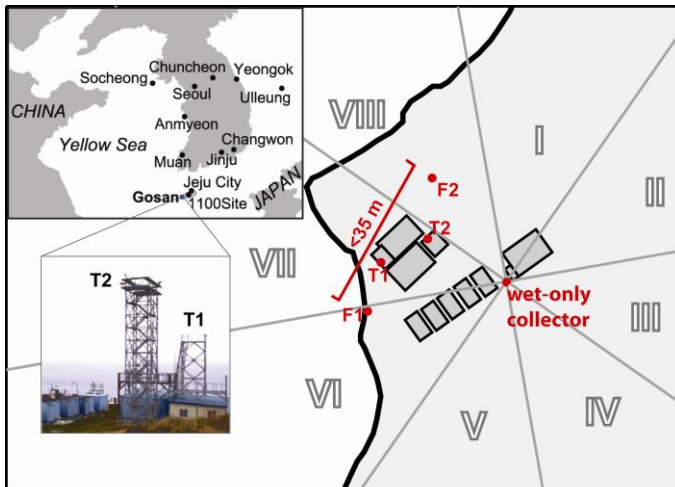


Figure 3-1. The location and outline of Gosan Station in Jeju Island, Korea. The simultaneous rain samples were collected at four points (T1, T2, F1 and F2) all within 35 m. The position of the wet only collector and the wind sector division (I to VIII) are displayed.

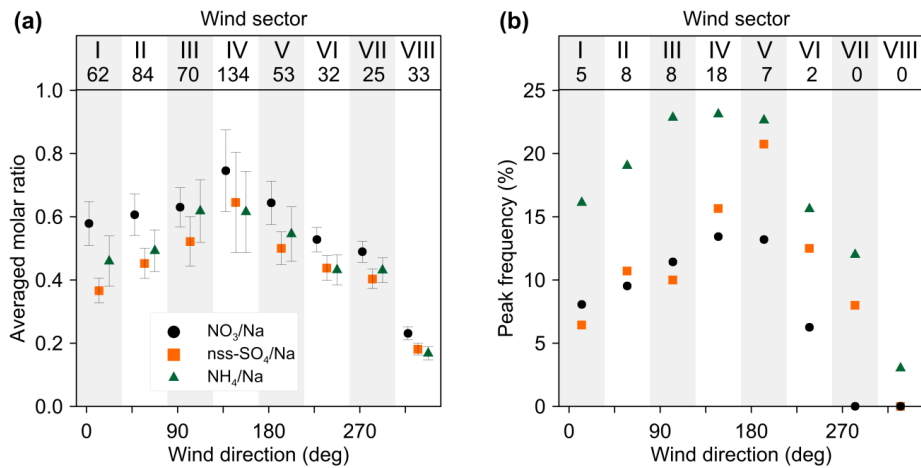


Figure 3-2. (a) The molar ratios of NO₃/Na, nss-SO₄/Na and NH₄/Na averaged for each wind sector. The wind sectors are designated by Roman numerals with number of samples belonging to each wind sector. The error bar indicates one-tenth the standard deviation (s.d). (b) The frequencies of peaks for NO₃/Na, nss-SO₄/Na and NH₄/Na ratios. The peak is defined by a value above the threshold of mean plus 3s.d.

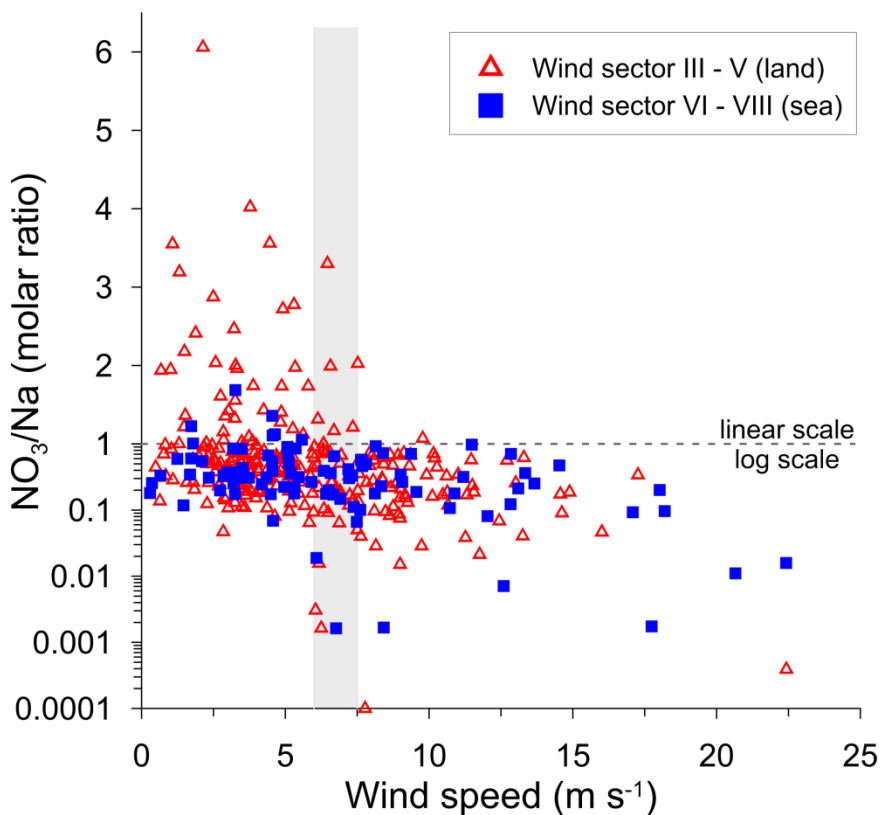


Figure 3-3. The relationship between the NO_3/Na ratio and wind speeds. The opened triangle (red) is for the land sectors and closed square (blue) is for the sea sector. The shaded indicates the change of predominant components of the local aerosol from the terrestrial to marine aerosols. Note the change in the scale at $\text{NO}_3/\text{Na} = 1$.

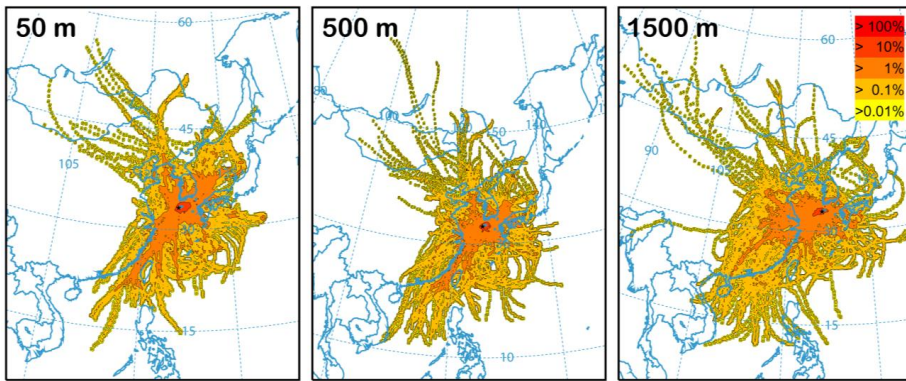


Figure 3-4. The frequency distribution map for trajectories computed for 43 NO_3/Na peaks, which are individually obtained at the starting heights of 50, 500 and 1500 m above ground levels.

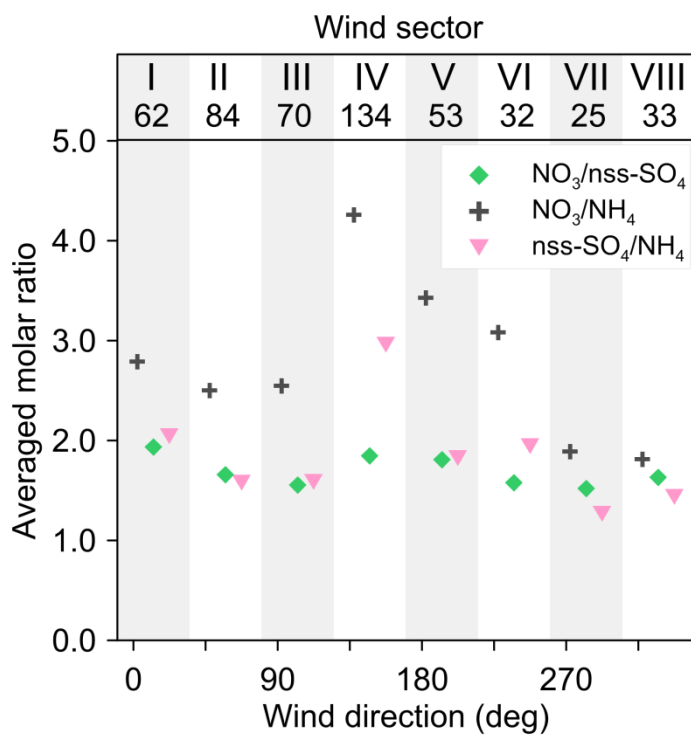


Figure 3-5. The molar ratios of $\text{NO}_3/\text{nss-SO}_4$, NO_3/NH_4 and $\text{nss-SO}_4/\text{NH}_4$ averaged for each wind sector.

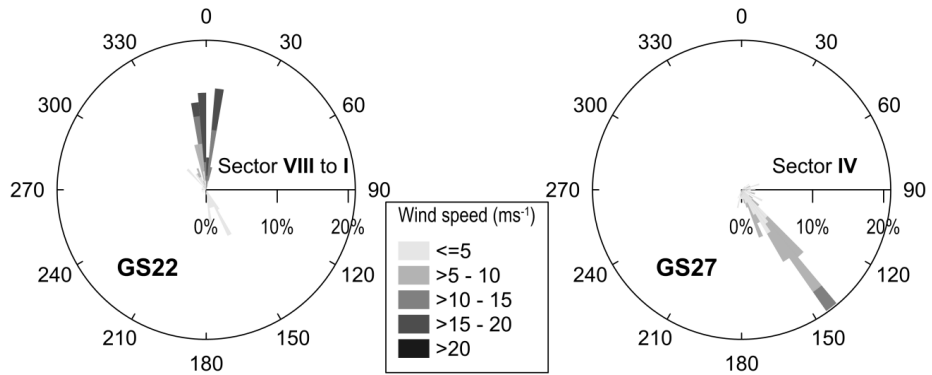


Figure 3-6. Wind diagram for GS22 and GS27 samples characterized by distinct wind direction.

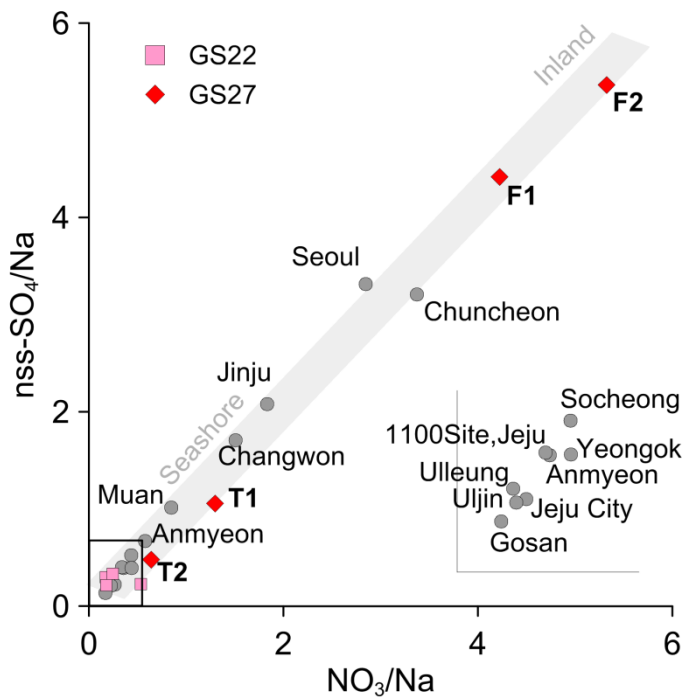


Figure 3-7. Plot of nss-SO₄/Na vs. NO₃/Na molar ratios. Gray circles are compilation from previous studies for long-term rainwater composition monitoring conducted in Korea. GS22 and GS27 samples are plotted by closed square and diamond symbols, respectively.

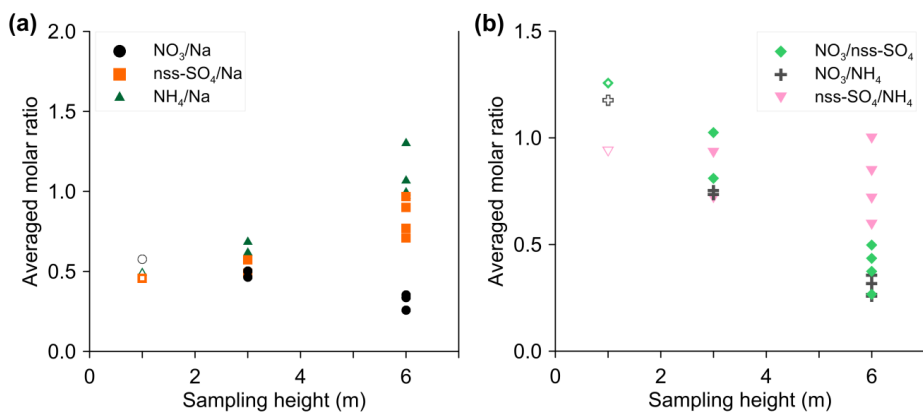


Figure 3-8. The molar ratios of water-soluble ions in total suspended particulate for (a) NO_3/Na , $\text{nss-SO}_4/\text{Na}$, NH_4/Na and (b) $\text{NO}_3/\text{nss-SO}_4$, NO_3/NH_4 , $\text{nss-SO}_4/\text{NH}_4$, monitored at 3 m and 6 m heights on Gosan Station. Those ratios for the rainwater composition are shown together.

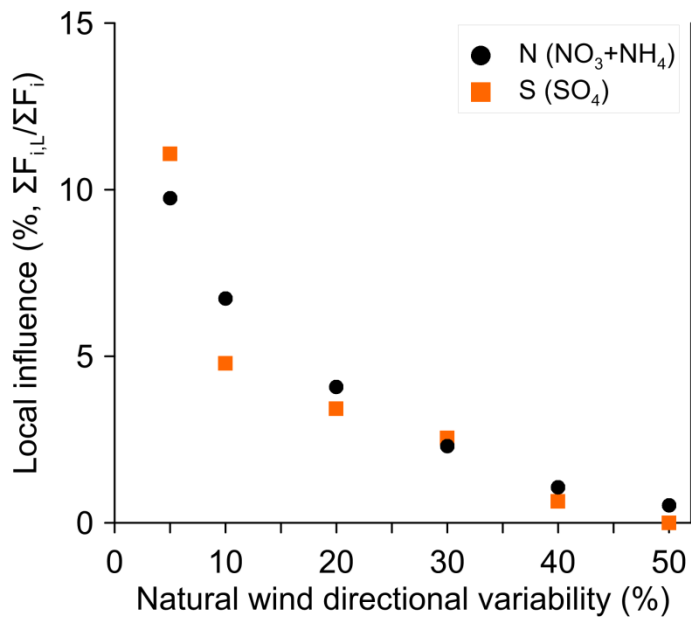


Figure 3-9. Model result for the quantification of the local influence. The lower limit for the local influence on the total nitrogen and sulfur deposition are estimated when predefined level (x-axis) is permitted for the wind directional variability of the background wet deposition.

Table 3-1. Water-soluble ion concentrations of total suspended particulate in Gosan Station.

Sampling height	Na	NO ₃	SO ₄	NH ₄	Sampling period	Reference
m (agl)	nmol m ⁻³	nmol m ⁻³	nmol m ⁻³	nmol m ⁻³	yyyy.mm	
3	170.3	85.5	93.7	116.4	2001.04 - 2002.03	Kawamura <i>et al.</i> , 2004
3	152.8	71.0	96.8	94.2	2003.04 - 2004.04	Kundu <i>et al.</i> , 2010
6	72.5	18.7	74.5	70.4	1992.03 - 1995.02	Carmichael <i>et al.</i> , 1997
6	80.0	25.0	75.0	83.0	1992.03 - 2002.02	Park, 2003
6	81.3	28.4	61.9	80.4	2001.01 - 2004.06	Hong <i>et al.</i> , 2011
6	102.2	34.3	84.9	133.0	2005.01 - 2006.12	Lee <i>et al.</i> , 2010

agl: above ground level

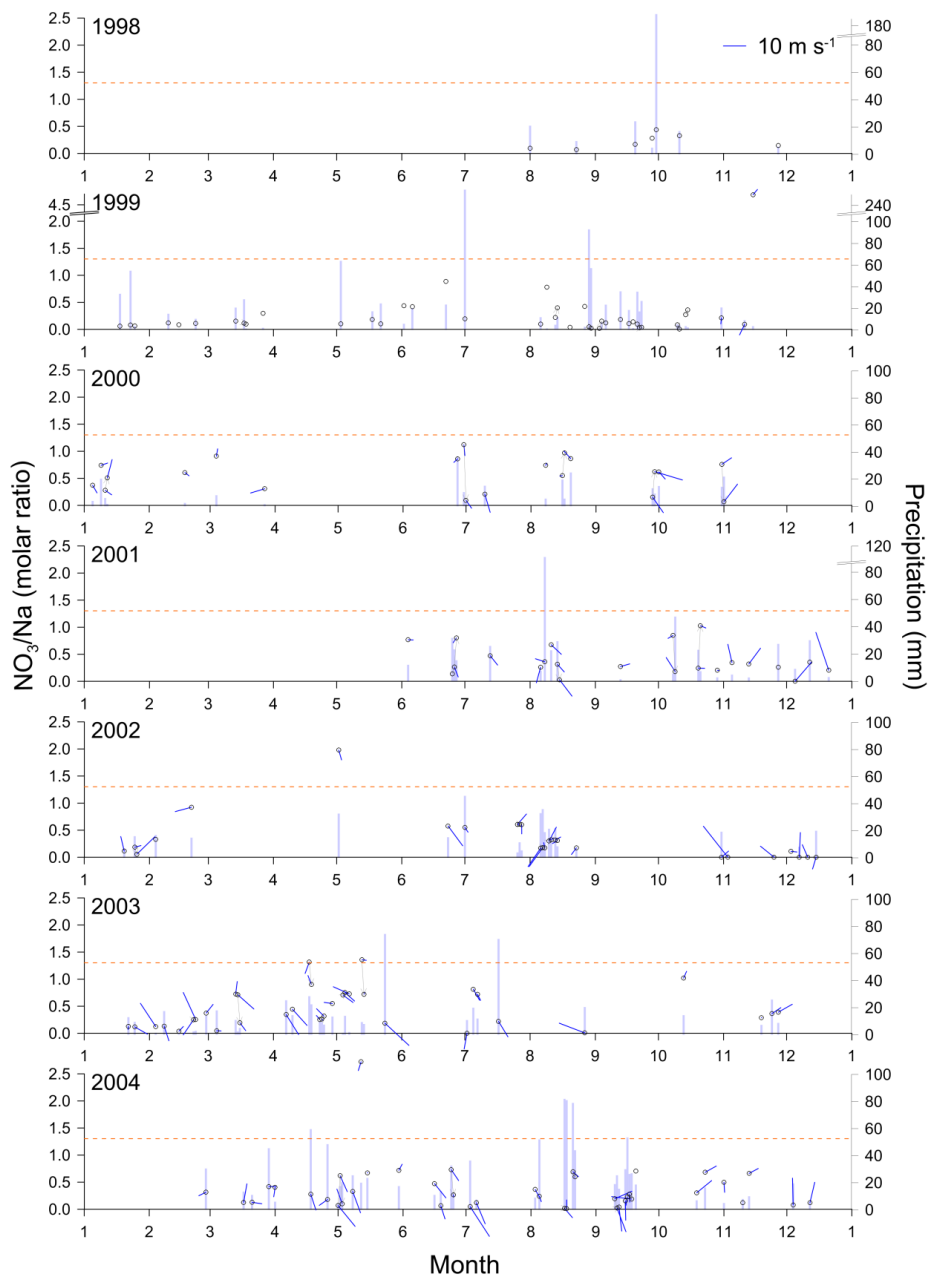


Figure 3-S1. Time series of NO_3/Na molar ratio with precipitation (mm) and wind directions and speeds from 1998 to 2004.

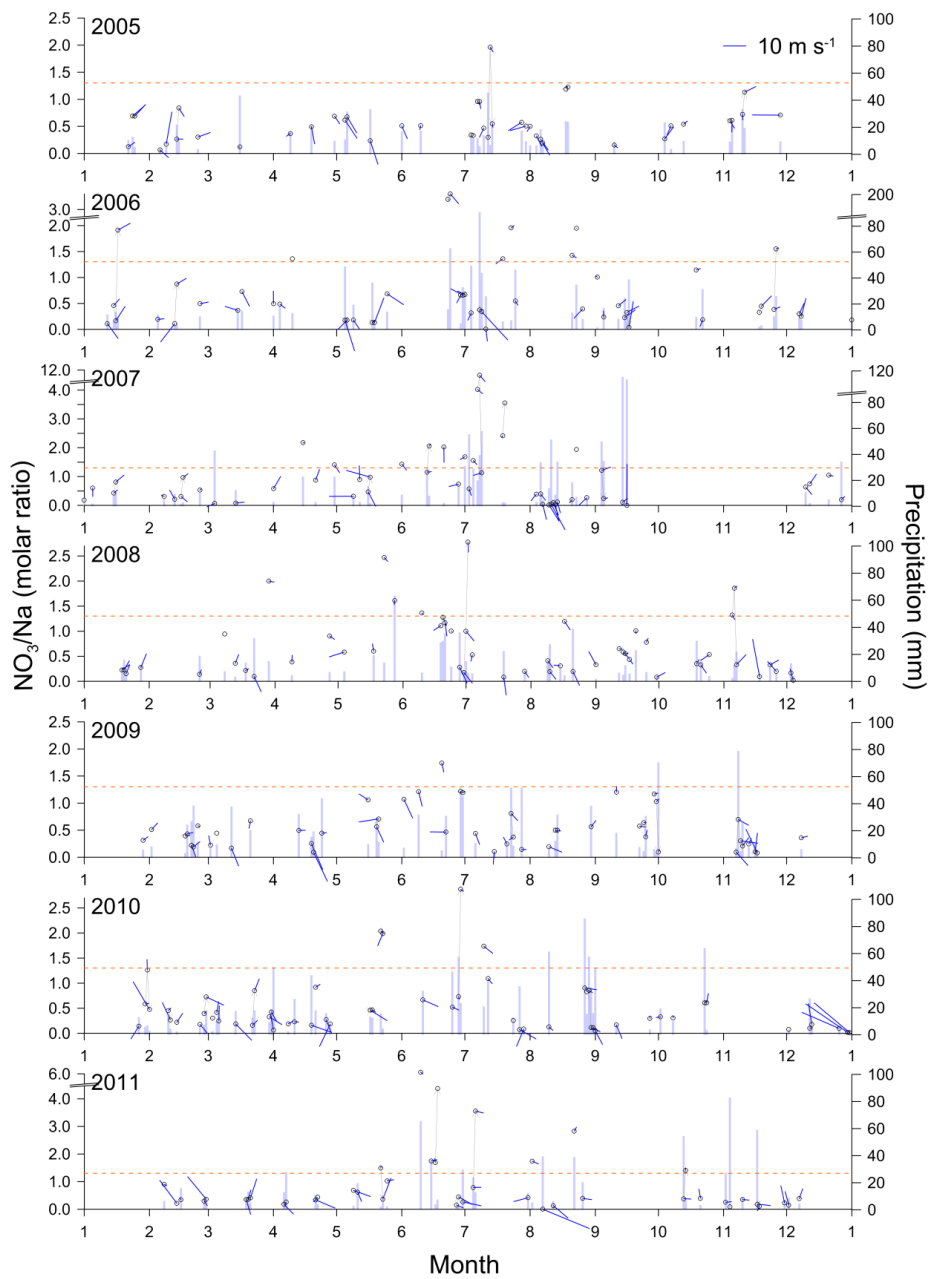


Figure 3-S1. (continued)

PART II

Chapter 4

Quantification of total mercury in Antarctic surface snow using ICP-SF-MS: spatial variation from the coast to Dome Fuji

Han, Y., Huh, Y., Hong, S., Hur, S.D., Motoyama, H., Fujita, S., Nakazawa, F., Fukui, K., 2011. Quantification of total mercury in Antarctic surface snow using ICP-SF-MS: spatial variation from the coast to Dome Fuji. Bull. Korean Chem. Soc. 32, 4258-4264

Abstract: The total mercury concentration (Hg_T) of surface snow samples collected along a ~1500 km transect in east Queen Maud Land was determined using inductively coupled plasma sector field mass spectrometry to address the behavior of Hg on the Antarctic Plateau. Due to the volatile nature of mercury, measures were taken against Hg loss from standard solutions by choosing appropriate container material and stabilizing agents. Glass bottles with Teflon-lined caps were superior to Teflon and polyethylene containers in protecting against Hg loss, but addition of gold chloride ($AuCl_3$) or bromine chloride ($BrCl$) was necessary to ensure preservation of Hg. As Hg loss was also observed in snowmelt samples, our analysis may underestimate the actual amount of Hg_T in the snow. Even so, the measured Hg_T was still very low ($< 0.4 - 10.8 \text{ pg g}^{-1}$, $n=44$) without a signal of depositional enhancement accompanying photo-oxidation of atmospheric elemental mercury in austral mid-summer. Moreover, the dynamic variation along the traverse implies spatial and temporal heterogeneity in its source processes.

Keywords: gaseous elemental mercury, reactive gaseous mercury, atmospheric mercury depletion event, photochemical oxidation and reduction

4.1. Introduction

The thick snowpack covering the vast Antarctic continent acts as a perennial sink for various trace metals (Boutron, 1995). Because gaseous elemental mercury (GEM, Hg^0) has a long atmospheric residence time of 6 – 24 months (Schroeder and Munthe, 1998b), it can be transported from distant sources and deposit onto the Antarctic snowpack (Sheppard *et al.*, 1991).

The sequestration of atmospheric Hg by polar snowpack results from an imbalance between the dry/wet deposition and re-emission principally governed by photochemical redox chemistry (Steffen *et al.*, 2008; Nguyen *et al.*, 2009). For example, the atmospheric mercury depletion event (AMDE) is the rapid disappearance of atmospheric GEM in spring as a result of its photo-oxidation to reactive gaseous mercury (RGM, Hg^{II}) and subsequent deposition onto surface snow (Lu *et al.*, 2001; Johnson *et al.*, 2008). The phenomenon of AMDE has been documented through atmospheric measurements, first at Alert in the Arctic (Schroeder *et al.*, 1998a) then in several Arctic (Steffen *et al.*, 2008; Nguyen *et al.*, 2009) and a few Antarctic sites (Ebinghaus *et al.*, 2002), which tends to occur with abundant marine halogen supply from nearby sea-ice. The deposition instantly elevates Hg levels in the surface snow, although it can be re-emitted as GEM through photochemical reduction (Lalonde *et al.*, 2002).

Recent studies of snow samples from Antarctica reported elevated total mercury (Hg_T) concentrations which were attributed to enhanced

atmospheric GEM oxidation. This has been observed both in the inland sites far from direct marine halogen supply, at South Pole (198 pg g⁻¹; Brooks *et al.*, 2008a) and Concordia (several hundred pg g⁻¹; Dommergue *et al.*, 2010) as well as in the sea-ice region near McMurdo (70 – 430 pg g⁻¹; Brooks *et al.*, 2008b) (Fig. 4-1, Table 4-1). These observations stand in contrast to previous studies which reported low Hg_T values both for the inland and coastal snow samples (< 40 pg g⁻¹, Table 4-1). One possible reason may be that prior to the first documentation of AMDE in 1998, high Hg_T levels in snow had been attributed to contamination (Dick *et al.*, 1990). As the snowpack over the vast Antarctic Plateau (> 5 million km²) may play an important role in the global Hg cycle, the wide variation of Hg_T of Antarctic snow in the literature needs to be evaluated precisely. Existing data sets are not systematic enough, temporally and spatially, to constrain important parameters such as distance from the coast, atmospheric circulation pattern, topography, and sampling season. One objective of this study was to add new Hg_T data for Antarctic surface snow with large spatial coverage within a relatively short sampling period (1.5 months).

Determination of Hg_T in the snowmelt is challenging because various Hg species (i.e. organic, inorganic and particulate) occur at very low levels (< 1 pg g⁻¹; Table 4-1), while some species are even volatile (e.g. Hg⁰, (CH₃)₂Hg). The inductively coupled plasma sector field mass spectrometry (ICP-SF-MS) offers a number of advantages over the conventional cold vapor generation method for determining Hg_T by reducing sample consumption, by eliminating complicated pretreatment steps, and by promoting decomposition of

nonreactive or strongly bound mercury (Planchon *et al.*, 2004). However it should be noted that the volatility of mercury, regarded as an advantage for the cold vapor generation method, can cause bias due to mercury loss from solutions prior to introduction into the ICP (Parker and Bloom, 2005). Single elemental mercury solutions prepared with dilute nitric acid is known to be extremely unstable (Planchon *et al.*, 2004; Parker and Bloom, 2005), and another objective of this study was to investigate the loss of volatile Hg in artificial standard solutions so that one can properly evaluate such loss in natural snowmelt samples.

4.2. Experimental

Snow samples were obtained during the Japanese-Swedish Antarctic Expedition (JASE) which took place between November 2007 and January 2008 as part of the International Trans Antarctic Scientific Expedition (ITASE) program. Surface snow samples were collected at 147 locations over a distance of ~3000 km (1500 km one way) from the Syowa Station near the coast via Dome Fuji (77.30°S, 39.78°E) to the Turning Point (75.88°S, 25.83°E) before returning to the Syowa Station (Fig. 4-1). Snow samples were transferred to thoroughly pre-cleaned 1 L LDPE bottles double sealed in acid-cleaned LDPE bags and kept frozen in the dark until further processing. Details on cleaning and sample handling protocols can be found in the reference (Hong *et al.*, 2000).

Of the 147 surface snow samples collected during the ITASE program, 44 were subsampled and analyzed for Hg_T (Fig. 4-1). Thirty five samples (hereafter referred to as SS1) were thawed at room temperature in a class 10 clean bench at the Korea Polar Research Institute (KOPRI). After complete melting which took less than 6 hours, ~5 mL aliquots for Hg_T analyses were stored in pre-cleaned 15 mL LDPE bottles and kept frozen in the dark. They were thawed and acidified to 2% HNO_3 just prior to ICP-SF-MS analyses. For nine samples (hereafter referred to as SS2), we skipped the second storage step by thawing, aliquoting, and acidifying the snow samples in the sample introduction area of the ICP-SF-MS and analyzing them immediately. It took less than 15 minutes from aliquoting to the end of analysis for each sample. The SS2 samples were refrozen until re-analysis carried out a month later.

Snow samples were analyzed on Thermo Scientific ELEMENT2 ICP-SF-MS installed at the National Center for Inter-university Research Facilities (NCIRF) at Seoul National University. The detection limit estimated as three times the standard deviation of the blank ($n=9$) was 0.4 pg g^{-1} or about 0.8 pg under our experimental conditions. See Supplementary Material for details on instrumental setting, calibration, blank, and wash procedures.

We prepared 20 pg g^{-1} Hg standard solutions to assess the temporal loss of Hg as a function of container material and preservative. The solutions were rapidly diluted from freshly prepared 100 ng g^{-1} solution with 2% HNO_3 using an electronic micropipette (50–1000 μL , precision < 0.6%, Eppendorf) just before instrumental analyses. Mercury loss was monitored every 10

minutes for one hour from solutions contained in four different types of containers: HDPE (15 mL centrifuge tube, BD Falcon), PTFE (15 mL Teflon vial with closure, Savillex), PFA (20 mL bottle, As One), and amber glass bottle with Teflon lined cap (40ml EPA vial, I-Chem). Bromine chloride (BrCl) and gold chloride (AuCl_3) were tested as preservatives against Hg loss. BrCl, an oxidizing agent generally used to determine Hg_T in cold vapor generation methods, was prepared following the U. S. Environmental Protection Agency (US EPA) method 245.7 “Mercury in water by cold vapor atomic fluorescence spectrometry”; it was added to 20 pg g^{-1} standard solution in HDPE tube to the final concentration of 0.5% (v/v) in 2% HNO_3 matrix. US EPA also recommends stabilizing Hg using $1 \text{ } \mu\text{g g}^{-1}$ AuCl_3 in 2% HNO_3 .¹⁹ However, we lowered the AuCl_3 concentration to 100 ng g^{-1} , considering the Hg impurity in commercial AuCl_3 solutions (1000 mg L^{-1} ICP single element standard, Inorganic Ventures Inc.). The standard solution with 100 ng g^{-1} AuCl_3 in amber glass bottle was also monitored every 10 minutes for an hour and was found to be stable.

4.3. Results and discussion

4.3.1. Mercury loss from dilute standard solutions

The temporal evolution of Hg loss in different types of containers is shown in Fig. 4-2a. Both HDPE and Teflon (PFA and PTFE) incurred significant loss of $0.09\text{--}0.15 \text{ pg Hg g}^{-1} \text{ min}^{-1}$. Although Teflon was expected to

be superior to HDPE against Hg loss (Parker and Bloom, 2005), both PFA and PTFE failed to preserve Hg for the monitoring duration of one hour (Fig. 4-2a). They showed slightly improved retention of 50 pg g⁻¹ Hg in 1% (v/v) HNO₃ only over longer term (5 hours): 82% (PTFE) versus 77% (LDPE) (not shown). The glass bottle retained Hg fairly well, with all results falling within 10% of the initial value (Fig. 4-2a). However, loss comparable to the HDPE was irregularly experienced (not shown), perhaps due to imperfect sealing of the vial. For this reason, we decided to further add preservatives to stabilize the Hg.

The strong oxidant BrCl has been used effectively for Hg fixation in solution, as for the ORMS-4 reference material kept in a glass ampule. For the HDPE bottle, adding BrCl to the same level as for the ORMS-4 (0.5% (v/v)) was also appeared to be efficient against Hg loss (Fig. 4-2b). Alternatively, the addition of AuCl₃ at a tenth (100 ng g⁻¹) of the US EPA recommended concentration retained Hg_T in the glass bottle (Fig. 4-2b). The irregular loss experienced with glass bottles was overcome with AuCl₃ addition. Injection of BrCl or AuCl₃ into the instrument can cause transient increase of the Hg signal, because they are more efficient than the wash solution (2% HNO₃) in mobilizing Hg from the sample introduction system. Therefore, use of preservatives required additional time for washing and conditioning.

The loss of Hg from standards leads to its overestimation in the sample, and the discrepancy increases with time. Applying the determined loss rate (0.09-0.15 pg Hg g⁻¹ min⁻¹) of the 20 pg g⁻¹ Hg standard solution, a delay of 10 minutes from the time of standard preparation would result in

about 5–8% overestimation (Fig. 4-S1). Factors such as bottle size, shape, and seal could change the loss rate.

In summary, immediate analyses of the working standards within a few minutes of dilution is a practical approach if an error range of 5–8% is acceptable. For better results, use of glass containers with Teflon seals and addition of an appropriate preservative effectively prevents Hg loss. In this study, we used glass containers and AuCl_3 for preparation of working standards.

4.3.2. Hg_T of surface snow samples

Total mercury in the surface snow samples (SS1, $n=35$) varied from below detection limit (0.4 pg g^{-1}) ($n=12$) to $10.8 \pm 1.2 \text{ pg g}^{-1}$ (1σ instrumental precision) (Fig. 4-3; Table 4-S2).

4.3.3. Mercury loss in snow samples

The SS2 series samples ($n=9$) suffered Hg loss similar to the dilute working standards. Of the nine samples, seven with original $\text{Hg}_T < 2 \text{ pg g}^{-1}$ fell below detection limit on the second analysis, and two with original $\text{Hg}_T > 2 \text{ pg g}^{-1}$ (samples 574 and 628) lost 52% and 37%, respectively, of the original Hg_T (Fig. 4-5; Table 4-S3). The loss of Hg from SS2 series samples implies that the SS1 series could also have experienced loss between aliquoting and analysis, making our Hg_T measurements underestimates. The ratio of Hg_T before and after storage is not unique for all SS2 samples and suggests that the

actual amount in SS1 can be approximately 2 – 5 times higher than what we measured.

It appears that the labile species of mercury in snow becomes volatile during melting and in the liquid state. Loss during transportation and storage is probably minimal since the samples were kept frozen in the dark to prevent photochemical redox reaction. Hg evasion during snowmelt has been observed in field studies (Lindberg *et al.*, 2002; Dommergue *et al.*, 2003; Faïn *et al.*, 2007), and laboratory experiments have also demonstrated increasing GEM flux as snow is melted (Faïn *et al.*, 2007). However, there have also been cases where only partial or no loss occurred (Planchon *et al.*, 2004; Dommergue *et al.*, 2007), implying that the extent of Hg loss is dependent on factors such as Hg speciation and the chemical composition of the snowmelt matrix.

4.3.4. Spatial variation of mercury from the coast inland

High Hg_T values above the third quartile ($> 1.7 \text{ pg g}^{-1}$) were observed only in the inner Plateau ($> 570 \text{ km}$ from the sea-ice, $> 3500 \text{ m}$ altitude) (Fig. 4-3, 4-4; Table 4-S2). The average Hg_T inland of site 560 is higher than that seaward of site 560 (Student's *t*-test, 95% confidence level). However, no significant trend was observed with distance from the sea ice ($r^2=0.19$) or with altitude ($r^2=0.15$) (Fig. 4-4). A consistent spatial trend of Hg_T in surface snow was found only within a short distance ($< 100 \text{ km}$): Hg_T gradually diminishing with distance inland from the edge of the sea ice, probably owing to the decreased supply of marine halogens for photo-oxidation of GEM (Brooks *et*

al., 2008b; Poulain *et al.*, 2007). For example, at McMurdo Hg_T decreased unevenly from 440 to 70 pg g^{-1} within approximately 30 km (Brooks *et al.*, 2008b), and Cornwallis Island in the Arctic from 17 to 2 pg g^{-1} within approximately 80 km (Poulain *et al.*, 2007). Our samples were collected along a much longer distance, and various factors could be obscuring a spatial trend. First, although direct transport of sea-salt decreases with distance from the coast, there could also be recycling of deposited halogens (Suzuki *et al.*, 2002; Hara *et al.*, 2004). Additionally, our most seaward sample (site 540) is already at an altitude of 948 m (Fig. 4-1, Table 4-S1, 4-S2). Hence, none of our samples is truly coastal. Second, the period of 1.5 months taken for the traverse from the Syowa Station to the turning point could have allowed varying degrees of depositional and post-depositional photochemical processes at coastal versus inland sites. Third, a given thickness of surface snow layer at an inland site integrates over a longer time interval than an equivalent thickness of surface snow layer near the coast because of the lower accumulation rate in the interior. Fourth, long-range transport and vertical precipitation of Hg from the stratosphere could be more pronounced on the inner Plateau.

The magnitude of spatial plus temporal variability can be gauged from the comparison of samples 590 vs. 678 and samples 574 vs. 675 in SS2 (Fig. 4-5). Each pair was obtained at the same sites albeit at different times (Fig. 4-1). The first pair coincided within uncertainty but the second pair exhibited a large discrepancy of a factor of 7 ($\sim 5 \text{ pg g}^{-1}$) (Fig. 4-5).

4.3.5. Low Hg_T in surface snow: low photo-oxidation or high photo-reduction?

Published Hg concentrations of Antarctic snow fall into two distinct categories: high (40 to hundreds of $pg\ g^{-1}$) and low ($< 40\ pg\ g^{-1}$) (Table 4-1). Lack of precise information on the sampling strategies and use of diverse analytical techniques make direct comparison difficult. Some studies do not report the sampling dates and the effect of temporal variation in the magnitude of photochemical oxidation of Hg cannot be appraised. In terms of analytical methods, the cold vapor generation method measures soluble inorganic Hg that can be readily reduced to elemental mercury, whereas the ICP-MS technique measures total mercury, i.e. all that can be ionized in the hot plasma. Even allowing for the temporally variable Hg_T level in surface snow and potential underestimation of SS1 series samples, it is still notable that our samples fall in the “low” category.

Total mercury in snow is balanced by deposition and re-emission fluxes in the course of photochemical redox processes (Steffen *et al.*, 2008). The quasi-permanent sequestration of Hg by the polar snowpack then should be determined by how long the snowpack resides above the sunlight penetration depth and how fast the reactive Hg^{II} in the snowpack is re-emitted as a consequence of photochemical reduction within the sunlit layer. The prevailing oxidation of atmospheric GEM to RGM after polar sunrise and subsequent deposition was postulated as cause for the high Hg_T in surface snow at two dome sites (Brooks *et al.*, 2008a; Dommergue *et al.*, 2010). It is proposed that three factors regulate the atmospheric mercury oxidation and

deposition – (1) supply of halogen radicals, (2) thickness of the turbulent mixing layer, and (3) amount of snowfall.

First, halogen radicals (e.g. Br·, BrO·, and Cl·) play a key role in the oxidation of atmospheric GEM. Although they are concentrated near sea-ice regions (Ebinghaus *et al.*, 2002), long-range transport and recycling of sea-salt appear to supply marine halogens even to the inland Plateau (Suzuki *et al.*, 2002). Sea-salt particles on Dome Fuji preferentially liberate Cl⁻ and Br⁻ in austral summer (Hara *et al.*, 2004), allowing GEM oxidation to advance (Brooks *et al.*, 2008a). Thus, the interior location in itself should not hinder Hg deposition on surface snow.

Second, the atmospheric turbulent layer encourages entrainment of RGM from the free troposphere during the sunlit period (Brooks *et al.*, 2008a), populating RGM near surface snow and subsequently depositing them. The thickness of the turbulent layer at Dome Fuji remains at ~20 m in winter but increases (up to ~300 m with diurnal variation) in summer (Swain and Gallée, 2006; Takato *et al.*, 2008). Therefore, the thickness of the turbulent layer should not limit surface Hg deposition at Dome Fuji.

Third, under the severely dry climatic condition of our sampling site, the low snowfall (< 10 cm yr⁻¹; Kameda *et al.*, 2008) could limit scavenging and deposition of RGM (Ferrari *et al.*, 2008). However, dry deposition of RGM to the snowpack provides an alternative pathway (Lindberg *et al.*, 2002) and hence the low snowfall cannot be the cause of low Hg deposition at our site.

Thus, our samples satisfy the conditions of the “high Hg_T ” category (thick turbulent layer, recycling of halogens) yet exhibit low Hg_T . The low Hg_T levels must be due to an as-yet-unidentified factor for GEM oxidation or to active post-depositional reduction.

Post-depositional photo-reduction causes re-emission of Hg from the surface snow and contributes to the temporal heterogeneity of Hg_T in snow (Ferrari *et al.*, 2005; Faïn *et al.*, 2007). Up to 40–54% of deposited Hg is released back to the atmosphere within 24 hours by photo-induced reduction in the temperate suburban areas (Lalonde *et al.*, 2002; Lalonde *et al.*, 2003) and up to 92% within 2 days after AMDE in the Arctic (Poulain *et al.*, 2004).

The extremely low (sometimes negative) accumulation rate on the inner Plateau compared to the coastal region exposes the snowpack to sunlight for a longer period. At Dome Fuji, the annual accumulation rate is as low as 10 cm y^{-1} and is slightly lower during the austral summer than winter (Kameda *et al.*, 2008). Assuming the effective penetration depth of sunlight to be deeper than 10 cm (King and Simpson, 2001; Warren *et al.*, 2006), the surface snow once deposited should reside within the sunlit layer for at least a year, allowing ample time for post-depositional photo-reduction. The lifetime of Hg^{II} in the snowpack under solar irradiation is estimated to be 1–6 hours (Dommergue *et al.*, 2007) but is subject to change depending on the chemical composition and physical property of the snow and ambient climatic conditions (Steffen *et al.*, 2008). The poorly understood dynamics and factors influencing the post-depositional fate of Hg do not allow us to draw an unequivocal conclusion regarding the reason for the low Hg_T in our surface

snow samples. Future studies on mass-independent fractionation of mercury isotopes associated with photochemical reactions (Sherman *et al.*, 2010) and continuous monitoring of atmospheric Hg species are expected to be helpful.

4.3.6. Refractory mercury

The fraction of Hg in snow resistant to evasion during melting and to photo-reduction is destined for long-term sequestration (Lalonde *et al.*, 2002; Planchon *et al.*, 2004; Dommergue *et al.*, 2007). We speculate that the major component of this refractory fraction is inorganic/organic particle-bound Hg, based on the sample behavior during ICP-SF-MS analyses and ice core records. The particle-bound fraction not oxidized by BrCl in conventional cold vapor generation method is decomposed at the high temperatures of the plasma (Planchon *et al.*, 2004). The high Hg_T of some samples analyzed by ICP-SF-MS was accompanied by large uncertainties (Fig. 4-3; Fig. 5 of Planchon *et al.*, 2004; Fig. 1 of Jiratu *et al.*, 2009), which can be explained by inhomogeneous distribution of particles in the snowmelt and their efficient decomposition in the plasma. Such associations would not be observed in data obtained with conventional methods which only detect total soluble Hg.

The 670-kyr record of the Dome C ice core shows Hg_T enhancements concurrent with increases of dust particle input during cold climate stages (Jiratu *et al.*, 2009). Particles scavenge RGM from the atmosphere, but the particle-bound Hg resists photo-reduction and is eventually sequestered in snow. Nearby volcanic eruptions or drier climate conditions can induce influx of particles to the Antarctic Plateau and promote

Hg sequestration. Our hypothesis about the long-term sequestration of Hg by refractory particles can be tested by investigating vertical profiles of mercury in snow pits at high resolution to obtain seasonal to annual Hg_T variations and episodic events like volcanic eruptions.

4.4. Conclusions

We obtained new Hg_T data of Antarctic surface snow that are near-contemporaneous (< 1.5 month) and spatially extensive (~1500 km traverse).

On the analytical side, we found that use of glass bottles and addition of $100 \text{ ng g}^{-1} \text{ AuCl}_3$ or 0.5%(v/v) BrCl prevent problematic Hg loss from dilute standard solutions. Some mercury loss also occurred in snowmelt samples, and we offer our Hg_T measurements as lower limits.

The Hg_T results displayed large spatial and/or temporal variation and were low compared to other Antarctic inland sites. This implies fast and/or spatially heterogeneous dynamics (oxidation-reduction) of Hg on the Antarctic snowpack. The factors that affect the long-term Hg sequestration are not fully understood, but snow accumulation rate and particle flux seem to be important.

Supplementary Material

Analytical details are available in the Supplementary Material. (Fig. 4-S1, Tables 4-S1 – 4-S3).

Acknowledgements

This work was performed as part of the ITASE project, and we thank all field personnel in the 2007–2008 Japanese-Swedish IPY Antarctic expedition. This work was supported by the Mid-Career Researcher Program (No. 2010-0027586) through NRF grant funded by the MEST, KOPRI research grant (No. PE11090), and Inha University research grant (No. INHA-42819-01).

4.5. References

- Boutron, C.F., 1995. Historical reconstruction of the earth's past atmospheric environment from Greenland and Antarctic snow and ice cores. *Environmental Reviews* 3(1), 1-28.
- Brooks, S., Arimoto, R., Lindberg, S., Southworth, G., 2008a. Antarctic polar plateau snow surface conversion of deposited oxidized mercury to gaseous elemental mercury with fractional long-term burial. *Atmospheric Environment* 42(12), 2877-2884.

- Brooks, S., Lindberg, S., Southworth, G., Arimoto, R., 2008b. Springtime atmospheric mercury speciation in the McMurdo, Antarctica coastal region. *Atmospheric Environment* 42(12), 2885-2893.
- Butler, L. C.; Pearson, G. Mercury preservation techniques, US Environmental Protection Agency, 2003, <http://www.epa.gov/esd/tsc/fact-sheets.htm>.
- Dick, A.L., Sheppard, D.S., Patterson, J.E., 1990. Mercury content of Antarctic surface snow: Initial results. *Atmospheric Environment* 24(4), 973-978.
- Dommergue, A., Ferrari, C.P., Gauchard, P.-A., Boutron, C.F., Poissant, L., Pilote, M., Jitaru, P., Adams, F.C., 2003. The fate of mercury species in a sub-arctic snowpack during snowmelt. *Geophysical Research Letter* 30(12), 1621.
- Dommergue, A., Bahlmann, E., Ebinghaus, R., Ferrari, C., Boutron, C., 2007. Laboratory simulation of Hg⁰ emissions from a snowpack. *Analytical and Bioanalytical Chemistry* 388(2), 319-327.
- Dommergue, A., Sprovieri, F., Pirrone, N., Ebinghaus, R., Brooks, S., Courteaud, J., Ferrari, C.P., 2010. Overview of mercury measurements in the Antarctic troposphere. *Atmospheric Chemistry and Physics* 10(7), 3309-3319.
- Ebinghaus, R., Kock, H.H., Temme, C., Einax, J.W., Löwe, A.G., Richter, A., Burrows, J.P., Schroeder, W.H., 2002. Antarctic springtime depletion of atmospheric mercury. *Environmental Science and Technology* 36(6), 1238-1244.

- Fain, X., Grangeon, S., Bahlmann, E., Fritsche, J., Obrist, D., Dommergue, A., Ferrari, C.P., Cairns, W., Ebinghaus, R., Barbante, C., Cescon, P., Boutron, C., 2007. Diurnal production of gaseous mercury in the alpine snowpack before snowmelt. *Journal of Geophysical Research* 112(21), D21311.
- Ferrari, C.P., Gauchard, P.-A., Aspmo, K., Dommergue, A., Magand, O., Bahlmann, E., Nagorski, S., Temme, C., Ebinghaus, R., Steffen, A., Banic, C., Berg, T., Planchon, F., Barbante, C., Cescon, P., Boutron, C.F., 2005. Snow-to-air exchanges of mercury in an Arctic seasonal snow pack in Ny-Å lesund, Svalbard. *Atmospheric Environment* 39(39), 7633-7645.
- Ferrari, C.P., Padova, C., Fa, X., Gauchard, P.-A., Dommergue, A., Aspmo, K., Berg, T., Cairns, W., Barbante, C., Cescon, P., Kaleschke, L., Richter, A., Wittrock, F., Boutron, C., 2008. Atmospheric mercury depletion event study in Ny-Å lesund (Svalbard) in spring 2005. Deposition and transformation of Hg in surface snow during springtime. *Science of the Total Environment* 397(1-3), 167-177.
- Hara, K., Osada, K., Kido, M., Hayashi, M., Matsunaga, K., Iwasaka, Y., Yamanouchi, T., Hashida, G., Fukatsu, T., 2004. Chemistry of sea-salt particles and inorganic halogen species in Antarctic regions: Compositional differences between coastal and inland stations. *Journal of Geophysical Research* 109(D20208).
- Hong, S., Lluberas, A., Rodriguez, F., 2000. A clean protocol for determining ultralow heavy metal concentrations: Its application to the analysis of

- Pb, Cd, Cu, Zn and Mn in Antarctic snow. *Korean Journal of Polar Research* 11, 35-47.
- Johnson, K.P., Blum, J.D., Keeler, G.J., Douglas, T.A., 2008. Investigation of the deposition and emission of mercury in arctic snow during an atmospheric mercury depletion event. *Journal of Geophysical Research* 113(D17), D17304.
- Jitaru, P., Gabrielli, P., Marteel, A., Plane, J.M.C., Planchon, F.A.M., Gauchard, P.A., Ferrari, C.P., Boutron, C.F., Adams, F.C., Hong, S., Cescon, P., Barbante, C., 2009. Atmospheric depletion of mercury over Antarctica during glacial periods. *Nature Geoscience* 2(7), 505-508.
- Kameda, T., Motoyama, H., Fujita, S., Takahashi, S., 2008. Temporal and spatial variability of surface mass balance at Dome Fuji, East Antarctica, by the stake method from 1995 to 2006. *Journal of Glaciology* 54, 107-116.
- Lalonde, J.D., Poulain, A.J., Amyot, M., 2002. The role of mercury redox reactions in snow on snow-to-air mercury transfer. *Environmental Science and Technology* 36(2), 174-178.
- Lalonde, J.D., Amyot, M., Doyon, M.-R., Auclair, J.-C., 2003. Photo-induced Hg(II) reduction in snow from the remote and temperate Experimental Lakes Area (Ontario, Canada). *Journal of Geophysical Research* 108, 4200.
- Lindberg, S.E., Brooks, S., Lin, C.J., Scott, K.J., Landis, M.S., Stevens, R.K., Goodsite, M., Richter, A., 2002. Dynamic oxidation of gaseous

mercury in the Arctic troposphere at polar sunrise. *Environmental Science and Technology* 36(6), 1245-1256.

Lu, J., Schroeder, W., Barrie, L., Steffen, A., Welch, H., Martin, K., Lockhart, L., Hunt, R., Boila, G., Richter, A., 2001. Magnification of atmospheric mercury deposition to polar regions in springtime: the link to tropospheric ozone depletion chemistry. *Geophysical Research Letter* 28(17), 3219-3222.

Nguyen, H.T., Kim, K.-H., Shon, Z.-H., Hong, S., 2009. A Review of Atmospheric Mercury in the Polar Environment. *Critical Reviews in Environmental Science and Technology* 39(7), 552 - 584.

Parker, J.L., Bloom, N.S., 2005. Preservation and storage techniques for low-level aqueous mercury speciation. *Science of the Total Environment* 337(1-3), 253-263.

Planchon, F.A.M., Gabrielli, P., Gauchard, P.A., Dommergue, A., Barbante, C., Cairns, W.R.L., Cozzi, G., Nagorski, S.A., Ferrari, C.P., Boutron, C.F., Capodaglio, G., Cescon, P., Varga, A., Wolff, E.W., 2004. Direct determination of mercury at the sub-picogram per gram level in polar snow and ice by ICP-SFMS. *Journal of Analytical Atomic Spectrometry* 19(7), 823-830.

Poulain, A.J., Lalonde, J.D., Amyot, M., Shead, J.A., Raofie, F., Ariya, P.A., 2004. Redox transformations of mercury in an Arctic snowpack at springtime. *Atmospheric Environment* 38(39), 6763-6774.

Poulain, A.J., Roy, V., Amyot, M., 2007. Influence of temperate mixed and deciduous tree covers on Hg concentrations and photoredox

- transformations in snow. *Geochimica et Cosmochimica Acta* 71(10), 2448-2462.
- Schroeder, W.H., Anlauf, K.G., Barrie, L.A., Lu, J.Y., Steffen, A., Schneeberger, D.R., Berg, T., 1998a. Arctic springtime depletion of mercury. *Nature* 394, 331-332.
- Schroeder, W.H., Munthe, J., 1998b. Atmospheric mercury – An overview. *Atmospheric Environment* 32(5), 809-822.
- Sheppard, D.S., Patterson, J.E., McAdam, M.K., 1991. Mercury content of Antarctic ice and snow: Further results. *Atmospheric Environment* 25(8), 1657-1660.
- Sherman, L.S., Blum, J.D., Johnson, K.P., Keeler, G.J., Barres, J.A., Douglas, T.A., 2010. Mass-independent fractionation of mercury isotopes in Arctic snow driven by sunlight. *Nature Geoscience* 3(3), 173-177.
- Steffen, A., Douglas, T., Amyot, M., Ariya, P., Aspö, K., Berg, T., Bottenheim, J., Brooks, S., Cobbett, F., Dastoor, A., Dommergue, A., Ebinghaus, R., Ferrari, C., Gardfeldt, K., Goodsite, M.E., Lean, D., Poulain, A.J., Scherz, C., Skov, H., Sommar, J., Temme, C., 2008. A synthesis of atmospheric mercury depletion event chemistry in the atmosphere and snow. *Atmospheric Chemistry and Physics* 8(6), 1445-1482.
- Suzuki, T., Iizuka, Y., Matsuoka, K., Furukawa, T., Kamiyama, K., Watanabe, O., 2002. Distribution of sea salt components in snow cover along the traverse route from the coast to Dome Fuji station 1000 km inland at east Dronning Maud Land, Antarctica. *Tellus B* 54(4), 407-411.25.

- Swain, M.R., Gallée, H., 2006. Antarctic boundary layer seeing. *Publications of the Astronomical Society of the Pacific* 118(846), 1190-1197.
- Takato, N., Ichikawa, T., Uraguchi, F., Lundock, R., Murata, C., Taniguchi, Y., Motoyama, H., Fukui, K., Taguchi, M., 2008. A 2-M class telescope at Dome Fuji. *European Astronomical Society Publications Series* 33, 271-274.
- King, M.D., Simpson, W.R., 2001. Extinction of UV radiation in Arctic snow at Alert, Canada (82°N). *Journal of Geophysical Research* 106, 12499-12507.
- Warren, S., Brandt, R., Grenfell, T., 2006. Visible and near-ultraviolet absorption spectrum of ice from transmission of solar radiation into snow. *Applied Optics* 45(21), 5320-5334.

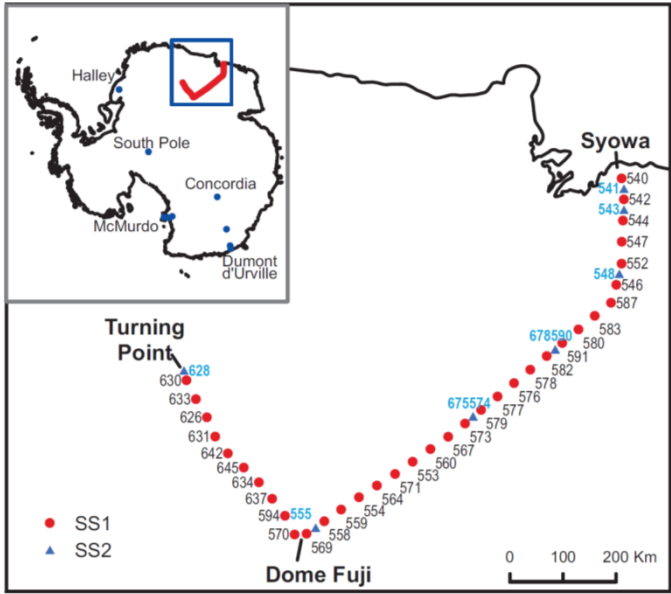


Figure 4-1. Sample location along the traverse from the Syowa station via Dome Fuji to the Turning Point and back. Site numbers are indicated for the SS1 series (analyzed after aliquoting and storage) and SS2 series (analyzed immediately after aliquoting). Samples 574 and 675 and samples 590 and 678 were collected at the same sites but at different times. Locations for which snow Hg data are available in the literature (Table 4-1) are shown on the inset. South Victoria Land and Taylor Valley are located close to McMurdo.

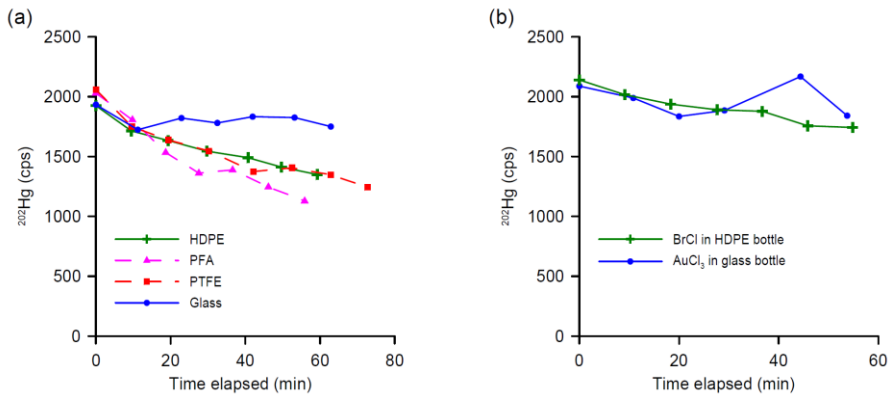


Figure 4-2. Mercury loss from 20 pg g⁻¹ Hg standard solutions for (a) different container material and (b) different preservatives (0.5% (v/v) BrCl and 100 ng g⁻¹ AuCl₃).

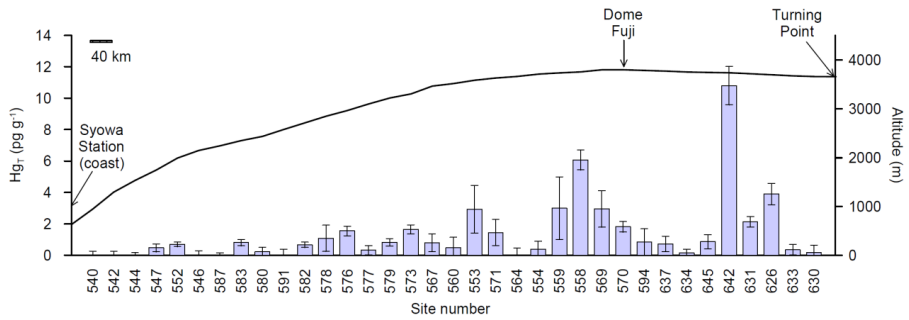


Figure 4-3. Total mercury concentrations of surface snow samples (SS1 series) collected along the traverse shown in Figure 4-1. These are underestimates due to potential mercury loss from the snowmelt samples. The error bars indicate 1 σ instrumental precision.

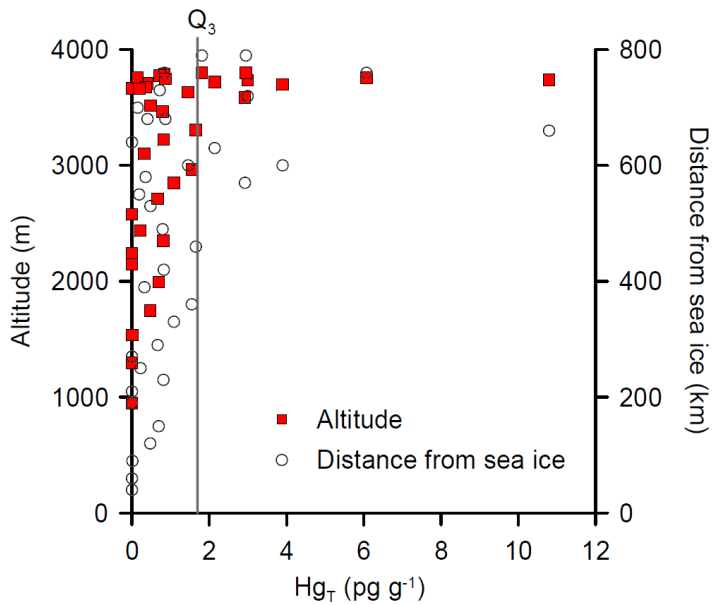


Figure 4-4. The relationship between total mercury and altitude (m) and distance from sea ice (km) for SS1 series. Q_3 indicates the third quartile ($1.7\ pg\ g^{-1}$).

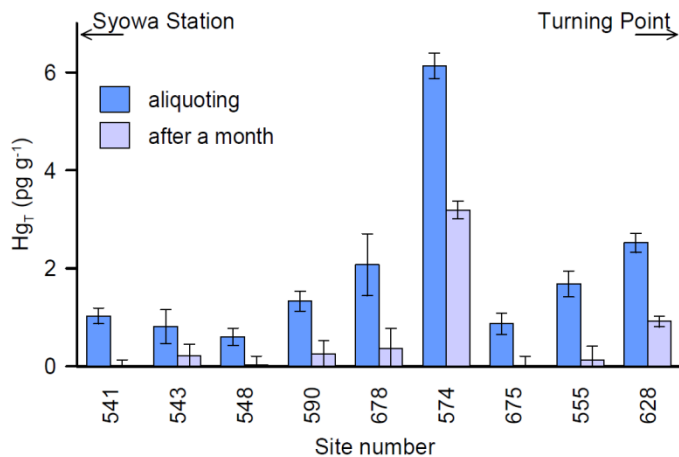


Figure 4-5. Duplicate analyses of the surface snow samples (SS2 series) analyzed a month apart. The error bars indicate 1σ instrumental precision.

Table 4-1. Published total mercury concentrations (Hg_T) in Antarctic snow

Location	Distance from coast (km)	Altitude (m)	Sampling date (yyyy/mm/dd)	Hg_T ($\mu g\ g^{-1}$)	Analytical method	Sample type	Reference
McMurdo	-30 – 0	0	2003/11/03 – 04	40 – 430 (n=24)	CVAFS	Surface snow on sea-ice	13
South Victoria Land	5	2200	1988/12/30 – 31	0.4 – 1.5 (n=5)	Photoacoustic Hg analyzer	Surface snow	3
Taylor Valley	10	678	2004	0.3 – 40 (n=32)	CVAFS	Snow pit	37
Dome F traverse	30 – 800	948 – 3809	2007/11/14 – 2008/01/19	<0.4 – 10.8 (n=44)	ICP-SF-MS	Surface snow	This study
Dumont d'Urville traverse	33	848	1983/01	0.50	CVAFS	Age 1982/09 – 1983/01	38
(Adelie Land – Dome C)	103	1500	1983/01	0.20	CVAFS	Age 1982/06 – 1983/01	
	433	2525	1983/01	0.13	CVAFS	Age 1982/06 – 1983/01	
Halley (Coats Land)	200	1420	1986-1987/ Summer	0.2 – 16.1 (n=170)	ICP-SF-MS	Depth 0 – 16.3 m Age 1834–1986	15
Concordia	1070	3240	Not reported	Hundreds	Not reported	Not reported	12
South Pole	1274	2880	1984/01	0.25	CVAFS	Age 1982/11 – 1984/01	38
South Pole	1274	2880	2005/11/16	198 (n=3)	Not reported	Surface snow	11

CVAFS: Cold Vapor Atomic Fluorescence Spectrometry

4.6. Supplementary Material

4.6.1. Instrumental setting and parameter optimization

Two sets of Thermo Scientific ELEMENT2 ICP-SF-MS installed at the National Center for Inter-university Research Facilities (NCIRF) at Seoul National University and at Korea Polar Research Institute (KOPRI) were used for total mercury (Hg_T) analyses. To prevent contamination, the sample introduction areas of the instruments were placed in class 100 clean booth (KOPRI) and laminar flow clean bench (NCIRF) inside dust-controlled rooms equipped with HEPA air filtration system. The two instruments were used in parallel for refining the analytical protocol and cross-checking their performances, but all snow samples were analyzed at NCIRF to achieve consistency.

Microflow PFA nebulizer (PFA-100, Elemental Scientific) and Scott type quartz spray chamber were routinely used for sample introduction at NCIRF. Scott type PFA spray chamber, cyclonic quartz/PFA spray chamber, and concentric glass nebulizer were also tested, but changing the components did not improve instrumental sensitivity or reduce memory effect.

The instrumental parameters (Table 4-S1) were optimized with 100 $\mu\text{g g}^{-1}$ multi-elemental solution at low resolution ($m \cdot \Delta m^{-1} = 300$) to obtain $> 120,000$ cps of ^{115}In and $^{238}\text{U}^{16}\text{O}^+ / ^{238}\text{U}^+$ ratio $< 8\%$.

4.6.2. Selection of isotope

Two isotopes of Hg were analyzed: ^{201}Hg and ^{202}Hg with natural abundances of 13.2% and 29.9%, respectively. The intensity of ^{184}W and ^{185}Re were monitored for potential interference on ^{202}Hg and ^{201}Hg from their oxides ($^{186}\text{W}^{16}\text{O}$, $^{185}\text{Re}^{16}\text{O}$), but for both the working standard solutions and natural samples, only sub-hundred counts per second (cps) intensities were detected contributing < 1% of ^{201}Hg and ^{202}Hg . Hence, additional corrections were skipped.

4.6.3. Calibration and detection limit

In order to apply external calibration, 1000 mg L⁻¹ single element Hg standard in 10% HNO₃ matrix (ICP standard, Merck) was sequentially diluted to the 1–20 pg g⁻¹ range. The working standard solutions were acidified to 2% (v/v) HNO₃ with ultrapure HNO₃ (Optima grade, Fisher Scientific) and sub-boiling double-distilled water (KOPRI) (Hong *et al.*, 2000). Gold chloride (AuCl₃) solution was added to a final concentration of 100 ng g⁻¹ as preservative for volatile Hg.

External calibration curve was obtained using more than 4 working standards. The slope normally varied within 100–150 cps (pg g⁻¹)⁻¹ ($r^2 > 0.99$) for ^{202}Hg and 45–65 cps (pg g⁻¹)⁻¹ ($r^2 > 0.99$) for ^{201}Hg depending on daily instrumental conditions. The detection limits, estimated as three times the standard deviation of the blank, were 0.3–0.5 pg g⁻¹ for ^{202}Hg and 0.5–0.7 pg g⁻¹ for ^{201}Hg .

To ensure accuracy, we tested three different certified reference materials (CRM): (1) NIST SRM 1641D is 1.557 ± 0.020 µg g⁻¹ mercury in

water, acidified to 2% (v/v) HNO₃ and stabilized with 1 µg g⁻¹ gold. Hg loss occurred when it was diluted to the working standard range, as the stabilizer was also diluted. Therefore, the diluted CRM was analyzed instantly to avoid loss. (2) NRCC ORMS-4 is elevated Hg in river water (22.0 ± 1.6 pg g⁻¹) stabilized with 0.5% (v/v) BrCl. It did not require dilution but, due to interference by tungsten oxide on ²⁰²Hg, only ²⁰¹Hg could be verified. (3) NWRI HG91 is reference water for Hg at a range of concentrations, 0.0028 (HG91-9) to 0.430 (HG91-10) µg L⁻¹, stabilized with 1% sulfuric acid and 0.5% potassium dichromate. They altered instrumental condition and require extremely long wash time due probably to the matrix. Therefore, it was better to dilute them so as to lower the sulfuric acid content and minimize their effect on instrumental conditions. HG91 also suffered from tungsten oxide interference. Adopting ORMS-4 and diluted SRM 1641D, we proceeded with sample analyses only when the results of CRMs deviated less than 10% from their certified values.

4.6.4. Blank and washing time

When the 5% HNO₃ wash solution was monitored in continuous acquisition mode after running enriched Hg solution (i.e. > 50 pg g⁻¹), the Hg intensity decreased exponentially before reaching a stable level. Conditioning with 2% HNO₃ (sample acidity) for one minute produced a stable ²⁰²Hg signal of < 500 cps that corresponded to about < 5 pg g⁻¹ of Hg. We confirmed the Hg blank of 2% HNO₃ to be less than the detection limit of gold-amalgamation cold-vapor atomic fluorescence spectrometry (< 0.1 pg g⁻¹) at

Korea Ocean Research & Development Institute. This implied that most Hg signal of the blank solution was contributed from memory effect in the sample introduction system of the ICP-SF-MS. This memory effect lowered the signal-to-blank ratio at pg g^{-1} Hg level. Nevertheless, since the background signal was not lowered by longer wash and since it persisted at a stable level (1% RSD over 10 minutes), the blank intensity could be subtracted from analyte intensity for correction (Jiratu *et al.*, 2009). We proceeded to the next sample only after the 2% HNO_3 blank stabilized at <500 cps. The 2% HNO_3 solution was periodically analyzed (every 5-6 samples) as a pseudo-sample and used for blank correction.

4.6.5. References

- Hong, S., Lluberas, A., Rodriguez, F., 2000. A clean protocol for determining ultralow heavy metal concentrations: Its application to the analysis of Pb, Cd, Cu, Zn and Mn in Antarctic snow. *Korean Journal of Polar Research* 11, 35-47.
- Jitaru, P., Gabrielli, P., Marteel, A., Plane, J.M.C., Planchon, F.A.M., Gauchard, P.A., Ferrari, C.P., Boutron, C.F., Adams, F.C., Hong, S., Cescon, P., Barbante, C., 2009. Atmospheric depletion of mercury over Antarctica during glacial periods. *Nature Geoscience* 2(7), 505-8.

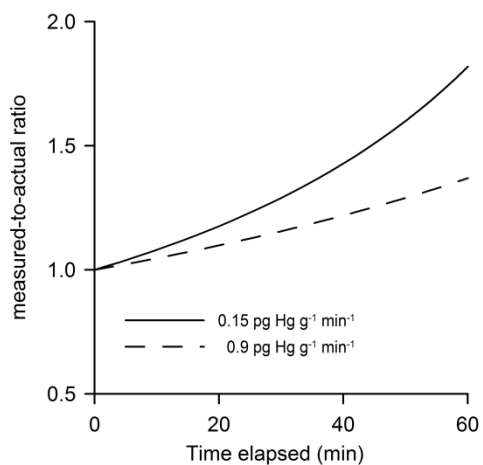


Figure 4-S1. The error propagation with time when applying the loss rate of the 20 pg g⁻¹ solution

Table 4-S1. Instrumental parameters for Element2.

RF power (W)	1200 - 1300
Gas flow rates	
Cool/l.min ⁻¹	16
Auxiliary/l.min ⁻¹	0.70 - 1.10
Sample/l.min ⁻¹	0.80 - 1.100
Washing time/min	3-6
Take up time/min	1
Selected isotopes	²⁰² Hg, ²⁰¹ Hg, ¹⁸⁴ W, ¹⁸⁵ Re
Resolution	Low ($m \cdot \Delta m^{-1}$) = 300
Sample per peak	50
Total acquisition time	0.5s per mass segment
Acquisition window (%)	100
Search window (%)	100
Integration window (%)	40

Table 4-S2. Sampling information and analytical results of SS1 sample set.

Site number	Longitude	Latitude	Altitude (m)	Date	Total Hg (ng L ⁻¹)	s.d. (1σ)
540	40.5531	-69.0388	948	2007-11-14	0.00	0.26
542	41.2855	-69.2812	1296	2007-11-15	0.00	0.25
544	41.9184	-69.5589	1535	2007-11-16	0.01	0.16
547	42.5742	-69.8346	1748	2007-11-17	0.47	0.25
552	43.3001	-70.1083	1993	2007-11-18	0.69	0.14
546	43.8379	-70.4273	2148	2007-11-18	0.00	0.29
587	44.2756	-70.7094	2244	2007-11-19	0.00	0.15
583	44.1441	-71.0572	2351	2007-11-20	0.81	0.20
580	44.0259	-71.4151	2439	2007-11-21	0.22	0.28
591	43.9045	-71.7723	2577	2007-11-22	0.00	0.37
582	43.7858	-72.1129	2714	2007-11-24	0.66	0.17
578	43.6523	-72.4710	2849	2007-11-25	1.08	0.84
576	43.5046	-72.8283	2966	2007-11-26	1.55	0.30
577	43.3475	-73.1855	3101	2007-11-26	0.32	0.30
579	43.1860	-73.5423	3224	2007-11-27	0.82	0.24
573	43.0360	-73.9003	3308	2007-11-28	1.65	0.29
567	42.8345	-74.2589	3465	2007-12-02	0.80	0.56
560	42.5360	-74.6200	3517	2007-12-03	0.48	0.66
553	42.2331	-74.9826	3586	2007-12-04	2.92	1.52
571	41.9107	-75.3396	3632	2007-12-05	1.45	0.83
564	41.5177	-75.6933	3666	2007-12-05	0.00	0.46
554	41.1085	-76.0482	3711	2007-12-06	0.40	0.50
559	40.7112	-76.4076	3737	2007-12-07	3.00	1.99
558	40.3341	-76.7492	3757	2007-12-08	6.07	0.63
569	39.9129	-77.1091	3801	2007-12-09	2.95	1.16
570	39.2360	-77.2490	3801	2007-12-16	1.81	0.34
594	37.7563	-77.0985	3789	2007-12-17	0.84	0.85
637	36.1955	-76.9995	3775	2007-12-18	0.72	0.49
634	34.6487	-76.8992	3757	2007-12-18	0.15	0.25
645	33.0797	-76.8362	3747	2007-12-19	0.86	0.45
642	31.5113	-76.7748	3739	2007-12-21	10.79	1.22
631	30.0472	-76.6395	3720	2007-12-21	2.14	0.33
626	28.8198	-76.4222	3698	2007-12-22	3.90	0.67
633	27.5058	-76.2342	3676	2007-12-23	0.35	0.34
630	26.2935	-76.0190	3663	2007-12-24	0.19	0.47

Table 4-S3. Sampling locations and analytical results for SS2 sample set.

Site number	Longitude	Latitude	Altitude (m)	Date	1st analysis		2nd analysis ^a	
					Total Hg (ng L ⁻¹)	s.d. (1σ)	Total Hg (ng L ⁻¹)	s.d. (1σ)
541	40.9377	-69.1426	1156	2007-11-15	1.03	0.16	0.00	0.13
543	41.5931	-69.4094	1412	2007-11-16	0.81	0.35	0.22	0.23
548	43.5526	-70.2599	2060	2007-11-18	0.60	0.18	0.03	0.18
590	43.8481	-71.9335	2634	2007-11-23	1.33	0.20	0.26	0.27
574	43.1044	-73.7208	3272	2007-11-28	6.14	0.26	3.19	0.18
555	40.1234	-76.9288	3781	2007-12-08	1.68	0.26	0.14	0.27
628	25.8337	-75.8880	3661	2007-12-27	2.52	0.20	0.92	0.11
675	43.1044	-73.7208	3272	2008-01-16	0.87	0.21	0.00	0.21
678	43.8481	-71.9335	2634	2008-01-19	2.08	0.63	0.36	0.41

^a The second analysis was carried out a month after the first analysis.

Chapter 5

Records of mercury sequestration in the shallow snow pits of Dome Fuji, Antarctica

Han, Y., Huh, Y., Hong, S., Hur, S.D., Motoyama, H., 2012. Records of mercury sequestration in the shallow snow pits of Dome Fuji, Antarctica. *To be submitted.*

Abstract: The investigation of mercury in the shallow snowpack is helpful for understanding the mercury dynamics over the Antarctic Plateau and their role in the global mercury cycle and for interpreting ice core data. The total mercury concentration (Hg_T) was determined from two 4-m snow pits recovered from Dome Fuji, which varied between <0.32 and 2.93 pg g^{-1} ($n=160$) seasonally to interannually. They were lower than the results simultaneously determined from the surface snow, which suggested the enhancement of photochemical redox processes and consequent bidirectional exchange of mercury between the snowpack and the atmosphere during the summer. However, their impact on Hg sequestration was not substantial during the past ~50 years. This stressed the role of the Antarctic Plateau snowpack as a temporal reservoir of mercury rather than its net sink.

Keywords: Hg dynamics, Antarctic Plateau, Antarctic snow, total mercury

5.1. Introduction

Mercury (Hg) found within the snowpack (or ice) in the Antarctic Plateau has two major implications. The first is that the Antarctic Plateau acts as a natural sink for mercury. By taking into consideration the vast extent (>5 million km²), the amount of mercury sequestered in this region could be a significant component of the global mercury cycle (Brooks *et al.*, 2008). Secondly, variation of mercury concentration in snowpack with depth can provide a temporal record of environmental changes that affect Hg sequestration (Jitaru *et al.*, 2009; Vandal *et al.*, 1993).

Recent studies suggested that an active exchange of mercury takes place between the atmosphere and surface snow in the Antarctic Plateau (Brooks *et al.*, 2008; Dommergue *et al.*, 2012). Among different species of mercury, gaseous elemental mercury (Hg⁰, GEM) has a relatively long atmospheric residence time of 6 – 24 months (Schroeder and Munthe, 1998) and is the primary species transported long-range via the atmosphere to the Antarctic Plateau environment. However, while the snowpack offers a large interstitial space for air-snow interaction (Dominé and Shepson, 2002), Hg⁰ is poorly adsorbed by snow (Bartels-Rausch *et al.*, 2008; Ferrari *et al.*, 2004). Instead, it is proposed that a series of photochemical redox processes would mediate the air-snow exchange of mercury (Brooks *et al.*, 2008). At the South Pole, for example, reactive Hg^{II} were abundantly detected in the atmospheric boundary layer during the sunlit period, and their rapid wet/dry deposition

greatly enriched Hg in the surface snow (Brooks *et al.*, 2008). The reverse flux of mercury from the snowpack to the atmosphere was evidenced by the Hg^0 concentration higher in interstitial air of the surface snowpack than in the ambient air, observed both at the South Pole (Brooks *et al.*, 2008) and Dome C (Dommergue *et al.*, 2012) in the summer season. Then, it can be thought that mercury that remains in the snowpack is the result of the photochemical Hg cycling during the sunlit period. However, it is unclear whether the active Hg cycling observed from the two dome sites can be extended to the entire Antarctic Plateau.

The investigation on snow represents a useful tool to address the impact of the Hg cycling on the snowpack. To date, there have been a few measurements of mercury concentration in surface snow on the Antarctic Plateau (Han *et al.*, 2011, and references therein). They were commonly reported at sub- to a few pg g^{-1} , before photochemical behavior of mercury was concerned. In recent studies, highly enriched Hg were reported as markers of the photochemical oxidation of Hg^0 to Hg^{II} during the sunlit period followed by its deposition onto the surface snow (198 pg g^{-1} at the South Pole, Brooks *et al.*, 2008; 60.3 pg g^{-1} near the Dome C, Dommergue *et al.*, 2012). In Han *et al.* (2011), we previously determined the total mercury concentration (Hg_T) of surface snow collected around the Dome Fuji in the summer (Fig. 5-1) but could not observe such elevations ($<0.4 - 10.8 \text{ pg g}^{-1}$, $n=30$). However, direct comparison of the present surface snow data poses several limitations. First, the sampling thicknesses were not reported. This can be problematic, especially when the surface Hg concentration rapidly decreases with depth as

exemplified in (Brooks *et al.*, 2008), because a thicker sampling would result in a lower Hg concentration. Second, snow accumulation rate could vary between individual sampling sites. In this case, the surface snow layers even with same thickness could integrate different time intervals. Third, most snow sampling has been carried out during the summer. Then, determined Hg concentration could be a transient value due to the photochemical cycle of mercury. Fourth, the analytical methods were not uniform. Various methods have been applied for determining Hg concentration; inductively coupled plasma sector field mass spectrometry (ICP-SFMS) (Han *et al.*, 2011), cold vapor atomic fluorescence spectrometry (CVAFS) (Dommergue *et al.*, 2012; Vandal *et al.*, 1995) and photoacoustic Hg analyzer (Sheppard *et al.*, 1991). The different analytical methods can produce different results for the same sample. For example, (Planchon *et al.*, 2004) showed that ICP-SFMS yielded higher Hg concentration than cold vapor generation method for the identical snow samples, which was attributed to a better dissociation of non-reactive or strongly bound mercury by the ICP. The cold vapor generation method relies on the reduction of Hg^{II} in solution to mercury vapor (Hg^0), and hence dissolved mercury reducible by the applied reducing agent (e.g., SnCl_2) are only measurable. For this reason, when determining the total mercury concentration, a pre-oxidation step with an oxidant (e.g., BrCl) is required to solubilize Hg in sample solution prior to the cold vapor generation. Then, the data obtained without pre-oxidation would reflect labile mercury species and underestimate the total mercury concentration (Vandal *et al.*, 1995).

Therefore, systematic approaches to both the sampling and analysis

are necessary to properly examine the impact of the mercury dynamics on the Antarctic Plateau snowpack, which has been hardly achieved. Here, following on the previous study on the surface snow (Han *et al.*, 2011), we report Hg_T in two 4-m snow pits obtained during the same expedition and determined using the same method with the surface sample. This allows for a reliable comparison between the surface snow and snow pit. In addition, Hg_T determined from successive snow layers of the snow pits would be useful for tracing seasonal to interannual variations in Hg sequestration. This study would contribute to understanding the impact of the photochemical Hg cycle on surface snow and sub-surface snowpack in the Antarctic Plateau.

5.2. Sample description and experimental methods

5.2.1. Sample description

Snow pits were obtained from two sites in Dronning Maud Land, East Antarctica during the Japanese-Swedish Antarctic Expedition, carried out between November 2007 and January 2008 as part of the International Trans Antarctic Scientific Expedition (ITASE) program (Fujita *et al.*, 2012; Fujita *et al.*, 2011). Pit-A was located at Dome Fuji (77.30°S, 39.78°E, 3785 m) and Pit-B (75.88°S, 25.83°E, 3656 m) was at a point ~400 km away from Pit-A (Fig. 5-1). Each pit was successively sampled at a 5 cm interval down to a depth of 4 m by pushing the cylindrical sampling container horizontally. The snow samples were transported in pre-cleaned 500 mL LDPE bottles double-

sealed in acid-cleaned LDPE bags and kept frozen in the dark until further processing. The ultraclean sampling protocol and the cleaning procedure for the sampling items are described in Hur *et al.* (2007) and Hong *et al.* (2000).

5.2.2. Analytical procedures

The snow samples were aliquoted after melting at room temperature, but the two pits were differently treated. For Pit-A, ~5 mL aliquots were contained in pre-cleaned 15 mL LDPE bottles and stored frozen in the dark. The aliquots were thawed and acidified to 2% HNO₃ just prior to the analyses. For Pit-B, ~5 ml aliquots were transferred into 20 ml PFA bottles and acidified to 2% HNO₃. The Pit-B aliquots were analyzed within 24 hours without a further storage step. The melting and aliquotation were performed in a class 10 clean bench at the Korea Polar Research Institute (KOPRI).

The difference in preparing the aliquots was related to mercury loss that could occur in this step. Mercury is unstable in the dilute nitric acid and readily volatilized (Han *et al.*, 2011). Although mercury in snowmelt could be sometimes stable (Planchon *et al.*, 2004), we observed significant Hg loss from the snowmelt of our surface snow samples, which resulted in an underestimation of Hg_T by a factor of 2 – 5 (Han *et al.*, 2011). The Pit-A samples was handled along with the surface snow samples throughout the sampling, transport, storage, aliquotation and analysis. This could cause Hg loss also in the Pit-A samples but allowed for a reliable comparison between the surface snow and Pit-A. For Pit-B, to minimize potential Hg loss, the aliquots were contained in Teflon (PFA) bottles (Parker and Bloom, 2005)

and rapidly analyzed. This could provide another comparison between Pit-A and Pit-B with respect to Hg loss after initial melting of the snow sample.

Hg_T of the snowmelt samples was determined by inductively coupled plasma sector field mass spectrometry (ICP-SF-MS) using Element2 (Thermo Scientific, Germany) at the National Center for Inter-university Research Facilities (NCIRF) in Seoul National University campus. ICP-SF-MS is capable of quantifying Hg at sub-pg g⁻¹ levels with limited sample volume (< a few mL) and hence particularly useful for the polar snow (or ice) samples that sample volume may be limited. The details of the analytical method can be found in Han *et al.* (2011). The working standard solutions, diluted to between 1 to 50 pg g⁻¹ in 2% (v/v) HNO₃, were prepared from a single elemental standard of Hg at 1000 mg L⁻¹ in a 10% HNO₃ matrix (ICP standard, Merck) to obtain external calibration curves for ²⁰¹Hg and ²⁰²Hg (natural abundances of 13.2% and 29.9%). To prevent mercury loss in the dilute standard solutions, gold chloride (AuCl₃) solution was added as a preservative to a final concentration of 100 µg L⁻¹. The instrumental sensitivity varied within 100-140 cps (pg g⁻¹)⁻¹ (r²>0.998) for ²⁰²Hg over the course of our analyses, which brought about slightly different detection limits (d.l) of 0.36 pg g⁻¹ for Pit-A and 0.32 pg g⁻¹ for Pit-B. Each detection limit was estimated as three times the standard deviation of the blank signal (n = 9). To ensure the accuracy of the calibration, two different certified reference materials (CRM) were tested: (1) ORMS-4 (elevated Hg in river water, 22.0 ± 1.6 pg g⁻¹ stabilized with 0.5% (v/v) BrCl, NRCC) and (2) diluted (1:100,000) SRM 1641D (mercury in water, 1.557 ± 0.020 µg g⁻¹ acidified to 2% (v/v) HNO₃

and stabilized with $1 \mu\text{g g}^{-1}$ gold, NIST). Since ORMS-4 contained tungsten-186 (^{186}W) that interfere ^{202}Hg , it was used to certify ^{201}Hg . The diluted SRM 1641 was used both for ^{201}Hg and ^{202}Hg . All CRM results coincided with the certified values within 10%.

The memory effect in the sample introduction part led to low signal-to-blank ratio at the pg g^{-1} Hg level, but the blank contribution could be reliably subtracted from the total signal based on the short term (1% RSD over 10 minutes) and long term (10% RSD over the course of analysis, 470 ± 50 cps, $n = 56$) stabilities of the blank. The intensity of ^{184}W and ^{185}Re were monitored for potential isobaric interferences from their oxides ($^{186}\text{W}^{16}\text{O}$, $^{185}\text{Re}^{16}\text{O}$), but their contributions to ^{202}Hg and ^{201}Hg signals were negligible for both the working standard solutions and the snowmelt samples (less than 1%); hence, additional corrections were unnecessary.

5.2.3. Depth-to-age models

The depth-to-age models for both snow pits are adopted from Soyol-Erdene *et al.* (2011) and Fujita *et al.* (2011) (Fig. 5-2). Those studies correlated striking non-sea-sulfate (nss-SO_4^{2-}) anomalies with the large volcanic eruptions of Mt. Pinatubo (1991), Mt. Cerro Hudson (1991) and Mt. Agung (1963) to constrain the depth-to-age relation. Using linear interpolation, the two pits have been estimated to cover ~53 years (1955 - 2008, Pit-A) and ~34 years (1974 - 2008, Pit-B), respectively.

Based on the mean accumulation rates, 5-cm snow layer approximately corresponded to 8 months in Pit-A and 5 months in Pit-B,

which would allow for the examination of seasonal to interannual variability in Hg sequestration. However, on-site monitoring at Dome Fuji using the 36 bamboo stakes showed spatial variations in the snow accumulation rate ranging 46 – 123% within $<0.01 \text{ km}^2$ during 1995 – 2006 (Kameda *et al.*, 2008), due to extremely low precipitation rates with intense post-depositional reworking, such as wind-born redistribution or sublimation on the Antarctic Plateau. Therefore, it should be noted that the temporal variation can be absent or diminished.

5.3. Results

The depth profiles of Hg_T with 90% confidence intervals (CI) are presented in Fig. 5-2 and Table 5-2. The results varied between <0.36 (below d.l, $n = 40$) and 2.93 pg g^{-1} in Pit-A ($n = 80$; Fig. 5-2a) and between <0.32 (below d.l, $n = 23$) and 0.89 pg g^{-1} in Pit-B ($n=80$; Fig. 5-2b). They were within the range previously reported but close to the lower end (Han *et al.*, 2011 and references therein).

In comparison, the snow pit samples appeared to have the lower Hg_T than the surface snow samples (Student's t-test; $P < 0.01$). The averages (\pm standard deviation, s.d) for Pit-A and Pit-B were $0.37 (\pm 0.57) - 0.56 (\pm 0.47)$ (minimum (\pm s.d) – maximum (\pm s.d)) and $0.36 (\pm 0.26) - 0.45 (\pm 0.15)$, respectively, whereas that of the surface snow samples with an altitude > 2500 m was $1.73 (\pm 2.35) - 1.81 (\pm 2.29)$. The box-whisker plots for the surface

snow samples, Pit-A and Pit-B are shown in Fig. 5-3, which also displays relative enrichment of Hg_T in the surface snow.

Despite the differences in the aliquot bottle and storage time, the results of Pit-A and Pit-B occurred over a similar range. This can suggest two possibilities: (1) The snow pit samples were depleted in volatile Hg species that could be reduced and reemitted into the atmosphere prior to its burial. (2) The Pit-B samples have undergone rapid Hg loss during a few hours (<24 hours) between the snow melting and instrumental analysis. In this case, the determined Hg_T would be underestimated.

For a calculation of the mercury sequestration rates, snow density profiles are adopted from Fujita *et al.* (2012) and the mercury content within each 5 cm layer down to a depth of 4 m is summed. Then the mean mercury sequestration rates are calculated to be $0.6 - 2.0 \text{ pg cm}^{-2} \text{ yr}^{-1}$ (Pit-A) and $1.1 - 2.4 \text{ pg cm}^{-2} \text{ yr}^{-1}$ (Pit-B) for the time period of ~53 and ~34 years, respectively. The rates at Pit-A and Pit-B are comparable, even when we compare the rate for the recent 34 years ($0.5 - 1.7 \text{ pg cm}^{-2} \text{ yr}^{-1}$). However, we note that the potential Hg loss could lead to underestimation of the Hg sequestration rates.

Available data for the mercury sequestration rate determined from the Antarctic snowpack or ice cores are compiled in Table 5-1. Prehistoric Hg sequestration in the Antarctic Plateau has been solely reconstructed from Dome C ice cores (Jitaru *et al.*, 2009; Vandal *et al.*, 1993) and is estimated to be $\sim 6 \text{ pg cm}^{-2} \text{ yr}^{-1}$ for the interglacial period (Jitaru *et al.*, 2009). The recent Hg sequestration estimated from near-coastal sites in the Victoria Land was $11 \text{ pg cm}^{-2} \text{ yr}^{-1}$ (Witherow and Lyons, 2008), 3.9 and $10.2 \text{ pg cm}^{-2} \text{ yr}^{-1}$ (Capelli *et al.*,

1998). The latter two values are likely underestimated, because they were determined for labile Hg species rather than Hg_T. In comparison, the rates at our sampling sites are shown to be at the lowest end of the range. Existing data broadly indicate that the mercury sequestration rates are higher at the coastal sites with low elevation and high snow accumulation rates than at the inland plateau sites under extremely arid conditions.

5.4. Discussion

5.4.1. Photochemical impact on mercury concentration in Antarctic Plateau snow

There are two striking implications of the lower Hg_T in the surface pit than in the surface snow. First, atmospheric Hg^{II} concentrations and its deposition to surface snow were enhanced during the summer. Second, the deposited Hg^{II} was mostly reduced and reemitted into the atmosphere. These interpretations are consistent with previous observations from the two other dome sites, the South Pole (Brooks *et al.*, 2008) and the Dome C (Dommergue *et al.*, 2012), which highlighted photochemically-mediated bidirectional exchange of mercury between the snowpack and the atmosphere in the summer. Then, it can be concluded that the bidirectional interaction is widespread over the Antarctic Plateau during the summer, despite its spatial heterogeneity (Han *et al.*, 2011). In addition, the active interaction allows the Antarctic Plateau snowpack to act as a temporal sink and source of mercury

(Brooks *et al.*, 2008) but does not result in the enhancement of Hg sequestration.

5.4.2. Current understanding of seasonal to interannual variation in Hg sequestration

The temporal variation in Hg sequestration would be primarily governed by the photochemical processes but was expected to be affected by various factors. One way to test the seasonality of Hg sequestration is correlating Hg_T with other proxies such as the chemical (e.g., ionic concentrations) and isotopic (e.g., $\delta^{18}O$, δD) compositions, even though intense post-depositional reworking can easily disrupt the seasonality (Motoyama *et al.*, 2005). Here, we compare Hg_T with sulfate (SO_4^{2-}) (Fig. 5-2). Sulfate concentration in atmospheric aerosols is highest during summer at Dome Fuji, but fractional sulfatization of sulfate aerosols and a diurnal cycle of snow sublimation and condensation are suggested to produce sulfate depleted snow layer during the summer season (Iizuka *et al.*, 2004; Iizuka *et al.*, 2012). Although how thick the sulfate depleted layer forms is unknown, Iizuka *et al.* (2004) adopted this layer as an indicator for the summer season and detected every annual layer for 37 years (1963 – 2000) based on a 2-cm sampling interval. Then if Hg_T elevation in the depth profile accompanies the sulfate minimum, this can be attributed to the photochemistry during the summer and prove the impact of the photochemical processes on Hg sequestration.

Although the thicker sampling intervals of 5-cm largely attenuated the

sulfate minima and only a few could be detected in our pits, we could detect some Hg_T peaks that accompanied the sulfate minimum (e.g. depth of 40 cm in Pit-A, 280 and 290 cm in Pit-B) (Fig. 5-2). However, other Hg_T peaks without the sulfate minimum point to another factor that enhanced Hg sequestration. For instance, when comparing with the density profile (Fujita *et al.*, 2012), we found that a few Hg_T peaks (e.g., depth of 235 and 250 cm in Pit-A) occurred in much less dense layers ($<300 \text{ kg m}^{-3}$) than the neighboring layers ($\sim 350 \text{ kg m}^{-3}$). One possible explanation for this is that heavy snowfall event during the summer encouraged the scavenging of RGM (Ferrari *et al.*, 2008) and sequestered deposited mercury before re-emitted.

Once produced, the oxidized mercury is easily incorporated into the snowpack via wet/dry deposition, and various factors can influence its flux, e.g., snowfall (Lalonde *et al.*, 2002), boundary layer depth (Brooks *et al.*, 2008; Dommergue *et al.*, 2010), and dust particle load (Jitaru *et al.*, 2009). After deposition, Hg^{II} is rapidly reduced under solar irradiation and reemitted into the atmosphere with a lifetime of several hours in the snowpack (Dommergue *et al.*, 2007). This process is favored by the low accumulation rate over the Antarctic Plateau, which allows ample time for photo-reduction before burial below the sunlit layer (Han *et al.*, 2011). However, the lifetime is subject to change depending on the chemical and physical properties of the snow and on meteorological factors (Steffen *et al.*, 2008). Additionally, it is proposed that reactive mercury scavenged by dust particle has an extended lifetime against photo-reduction in the snowpack and can be sequestered (Han *et al.*, 2011; Jitaru *et al.*, 2009). Overall, oxidation, deposition and re-emission

have effects on the seasonal to interannual variation in Hg sequestration, but the understanding of each process still remains incomplete.

We could not find a relationship between Hg_T and other constituents such as major elements, trace metals (Hong *et al.*, 2012) or platinum group elements (PGEs) (Soyol-Erdene *et al.*, 2011). The reason for this is that other elements are more sensitive to variation in their emission and transport to the Antarctic Plateau, whereas atmospheric mercury maintains a relatively constant background level at $\sim 1 \text{ ng m}^{-3}$. For example, volcanic emissions (i.e., Pinatubo, Cerro Hudson, El Chinchon, Agung) have left distinct peaks of sulfate, aluminum or PGEs within the snow profiles (Soyol-Erdene *et al.*, 2011), but their contribution to mercury sequestration is not recognizable, in spite of the significant mercury load of giant volcanic eruptions into the atmosphere (Pyle and Mather, 2003). This stresses that photochemical dynamics play a leading role in mercury sequestration in the Antarctic Plateau.

5.5. Conclusion

Hg_T determined from two shallow snow pits on the Antarctic Plateau were lower than the results simultaneously determined from the surface snow. This stressed that the photochemical processes that led to redox reactions of mercury were widespread over the Antarctic Plateau during the summer. However, its impact on Hg sequestration was not significant during past the

~50 years. This indicated that the Antarctic Plateau snowpack play a role as a temporal sink and source of mercury rather than its net sink.

Acknowledgements

The traverse was fully supported by the teams of the 48th and 49th Japanese Antarctic Research Expeditions led by H. Miyaoka and S. Imura, respectively. Special thanks go to members of the traverse, S. Fujita, H. Enomoto, S. Sugiyama, K. Fukui and F. Nakazawa, for their very generous support during the traverse. This work was supported by the Mid-Career Researcher Program (No. 2010-0027586) through an NRF grant funded by the MEST, a KOPRI research grant (No. PE12070), an Inha University research grant (No. INHA-40890-01), and the Japan Society for the Promotion of Science (JSPS) research grant ((A) 20241007).

5.6. References

- Bartels-Rausch, T., Huthwelker, T., Jöri, M., Gäggeler, H., Ammann, M., 2008. Interaction of gaseous elemental mercury with snow surfaces: laboratory investigation. *Environmental Research Letters* 3(4).
- Brooks, S., Arimoto, R., Lindberg, S., Southworth, G., 2008. Antarctic polar plateau snow surface conversion of deposited oxidized mercury to gaseous elemental mercury with fractional long-term burial.

Atmospheric Environment 42(12), 2877-84.

Capelli, R., Minganti, V., Chiarini, C., De Pellegrini, R., 1998. Mercury in snow layers from the Antarctica. *International Journal of Environmental Analytical Chemistry* 71(3), 289-96.

Dominé, F., Shepson, P.B., 2002. Air-snow interactions and atmospheric chemistry. *Science* 297(5586), 1506.

Dommergue, A., Bahlmann, E., Ebinghaus, R., Ferrari, C., Boutron, C., 2007. Laboratory simulation of Hg⁰ emissions from a snowpack. *Analytical and Bioanalytical Chemistry* 388(2), 319-27.

Dommergue, A., Barret, M., Courteaud, J., Cristofanelli, P., Ferrari, C., Gallée, H., 2012. Dynamic recycling of gaseous elemental mercury in the boundary layer of the Antarctic Plateau. *Atmospheric Chemistry and Physics* 12(22), 11027-11036.

Dommergue, A., Sprovieri, F., Pirrone, N., Ebinghaus, R., Brooks, S., Courteaud, J., Ferrari, C.P., 2010. Overview of mercury measurements in the Antarctic troposphere. *Atmospheric Chemistry and Physics* 10(7), 3309-19.

Ferrari, C.P., Dommergue, A., Boutron, C.F., Jitaru, P., Adams, F.C., 2004. Profiles of Mercury in the snow pack at Station Nord, Greenland shortly after polar sunrise. *Geophysical Research Letters* 31(3).

Ferrari, C.P., Padova, C., Fa, X., Gauchard, P.-A., Dommergue, A., Aspö, K., Berg, T., Cairns, W., Barbante, C., Cescon, P., Kaleschke, L., Richter, A., Wittrock, F., Boutron, C., 2008. Atmospheric mercury depletion event study in Ny-Ålesund (Svalbard) in spring 2005. Deposition and

transformation of Hg in surface snow during springtime. *Science of the Total Environment* 397(1-3), 167-77.

Fujita, S., Enomoto, H., Fukui, K., Iizuka, Y., Motoyama, H., Nakazawa, F., Sugiyama, S., Surdyk, S., 2012. Formation and metamorphism of stratified firm at sites located under spatial variations of accumulation rate and wind speed on the East Antarctic ice divide near Dome Fuji. *The Cryosphere Discuss.* 6(2), 1205-1267.

Fujita, S., Holmlund, P., Andersson, I., Brown, I., Enomoto, H., Fujii, Y., Fujita, K., Fukui, K., Furukawa, T., Hansson, M., Hara, K., Hoshina, Y., Igarashi, M., Iizuka, Y., Imura, S., Ingvander, S., Karlin, T., Motoyama, H., Nakazawa, F., Oerter, H., Sjöberg, L.E., Sugiyama, S., Surdyk, S., Ström, J., Uemura, R., Wilhelms, F., 2011. Spatial and temporal variability of snow accumulation rate on the East Antarctic ice divide between Dome Fuji and EPICA DML. *The Cryosphere* 5(4), 1057-1081.

Han, Y., Huh, Y., Hong, S., Hur, S.D., Motoyama, H., Fujita, S., Nakazawa, F., Fukui, K., 2011. Quantification of total mercury in Antarctic surface snow using ICP-SF-MS: spatial variation from the coast to Dome Fuji. *Bulletin of the Korean Chemical Society* 32(12), 4258-64.

Hong, S., Lluberas, A., Rodriguez, F., 2000. A clean protocol for determining ultralow heavy metal concentrations: Its application to the analysis of Pb, Cd, Cu, Zn and Mn in Antarctic snow. *Kororean Journal of Polar Research* 11, 35-47.

Hong, S., Soyol-Erdene, T.-O., Hwang, H.J., Hong, S.B., Hur, S.D.,

- Motoyama, H., 2012. Evidence of Global-Scale As, Mo, Sb, and Tl Atmospheric Pollution in the Antarctic Snow. *Environmental Science and Technology* 46(21), 11550-11557.
- Hur, S.D., Cunde, X., Hong, S., Barbante, C., Gabrielli, P., Lee, K., Boutron, C.F., Ming, Y., 2007. Seasonal patterns of heavy metal deposition to the snow on Lambert Glacier basin, East Antarctica. *Atmospheric Environment* 41(38), 8567-78.
- Iizuka, Y., Fujii, Y., Hirasawa, N., Suzuki, T., Motoyama, H., Furukawa, T., Hondoh, T., 2004. SO₄²⁻ minimum in summer snow layer at Dome Fuji, Antarctica, and the probable mechanism. *Journal of Geophysical Research* 109(D04307).
- Iizuka, Y., Tsuchimoto, A., Hoshina, Y., Sakurai, T., Hansson, M., Karlin, T., Fujita, K., Nakazawa, F., Motoyama, H., Fujita, S., 2012. The rates of sea salt sulfatization in the atmosphere and surface snow of inland Antarctica. *Journal of Geophysical Research* 117(D4).
- Jitaru, P., Gabrielli, P., Marteel, A., Plane, J.M.C., Planchon, F.A.M., Gauchard, P.A., Ferrari, C.P., Boutron, C.F., Adams, F.C., Hong, S., Cescon, P., Barbante, C., 2009. Atmospheric depletion of mercury over Antarctica during glacial periods. *Nature Geoscience* 2(7), 505-8.
- Kameda, T., Motoyama, H., Fujita, S., Takahashi, S., 2008. Temporal and spatial variability of surface mass balance at Dome Fuji, East Antarctica, by the stake method from 1995 to 2006. *Journal of Glaciology* 54, 107-16.
- Lalonde, J.D., Poulain, A.J., Amyot, M., 2002. The role of mercury redox

reactions in snow on snow-to-air mercury transfer. *Environmental Science and Technology* 36(2), 174-8.

Motoyama, H., Hirasawa, N., Satow, K., Watanabe, O., 2005. Seasonal variations in oxygen isotope ratios of daily collected precipitation and wind drift samples and in the final snow cover at Dome Fuji Station, Antarctica. *Journal of Geophysical Research* 110(D11).

Parker, J.L., Bloom, N.S., 2005. Preservation and storage techniques for low-level aqueous mercury speciation. *Science of the Total Environment* 337(1-3), 253-263.

Planchon, F.A.M., Gabrielli, P., Gauchard, P.A., Dommergue, A., Barbante, C., Cairns, W.R.L., Cozzi, G., Nagorski, S.A., Ferrari, C.P., Boutron, C.F., Capodaglio, G., Cescon, P., Varga, A., Wolff, E.W., 2004. Direct determination of mercury at the sub-picogram per gram level in polar snow and ice by ICP-SFMS. *Journal of Analytical Atomic Spectrometry* 19(7), 823-30.

Pyle, D.M., Mather, T.A., 2003. The importance of volcanic emissions for the global atmospheric mercury cycle. *Atmospheric Environment* 37(36), 5115-24.

Schroeder, W.H., Munthe, J., 1998. Atmospheric mercury – An overview. *Atmospheric Environment* 32(5), 809-822.

Sheppard, D.S., Patterson, J.E., McAdam, M.K., 1991. Mercury content of Antarctic ice and snow: Further results. *Atmospheric Environment* 25(8), 1657-1660.

Soyol-Erdene, T.-O., Huh, Y., Hong, S., Hur, S.D., 2011. A 50-year record of

platinum, iridium, and rhodium in Antarctic snow: volcanic and anthropogenic sources. *Environmental Science and Technology* 45(14), 5929-35.

Steffen, A., Douglas, T., Amyot, M., Ariya, P., Aspö, K., Berg, T., Bottenheim, J., Brooks, S., Cobbett, F., Dastoor, A., Dommergue, A., Ebinghaus, R., Ferrari, C., Gardfeldt, K., Goodsite, M.E., Lean, D., Poulain, A.J., Scherz, C., Skov, H., Sommar, J., Temme, C., 2008. A synthesis of atmospheric mercury depletion event chemistry in the atmosphere and snow. *Atmospheric Chemistry and Physics* 8(6), 1445-82.

Vandal, G.M., Fitzgerald, W.F., Boutron, C.F., Candelone, J.-P., 1993. Variations in mercury deposition to Antarctica over the past 34,000 years. *Nature* 362, 621-3.

Vandal, G.M., Fitzgerald, W.F., Boutron, C.F., Candelone, J.P., 1995. Mercury in ancient ice and recent snow from the Antarctic. in: *Delmas, R.J. (Ed.), Ice Core Studies of Global Biogeochemical Cycles*. Springer-Verlag, Berlin, Germany, pp. 401-416.

Wetherow, R.A., Lyons, W.B., 2008. Mercury deposition in a polar desert ecosystem. *Environmental Science and Technology* 42(13), 4710-6.

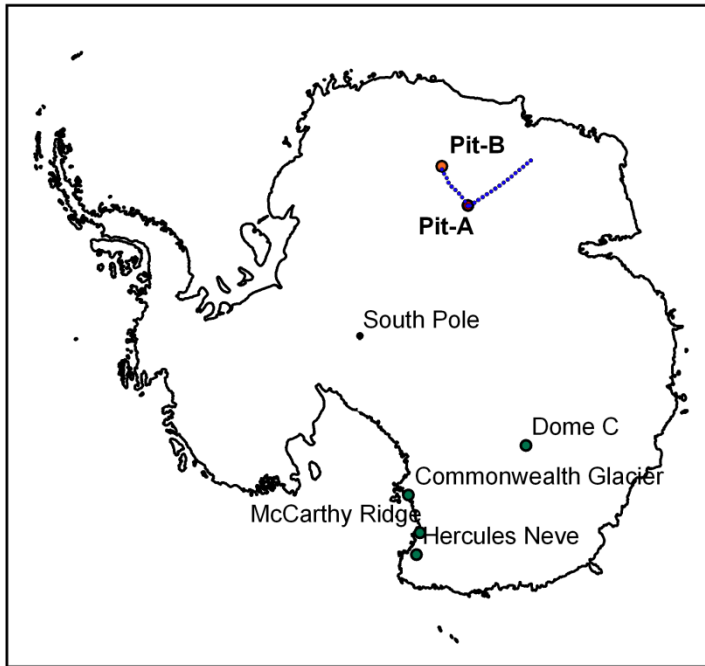


Figure 5-1. The sampling locations for Pit-A at Dome Fuji and Pit-B. The blue dots are the sampling locations for the surface snow samples from Han *et al.* (2011). The green circles indicate the locations listed in Table 5-1.

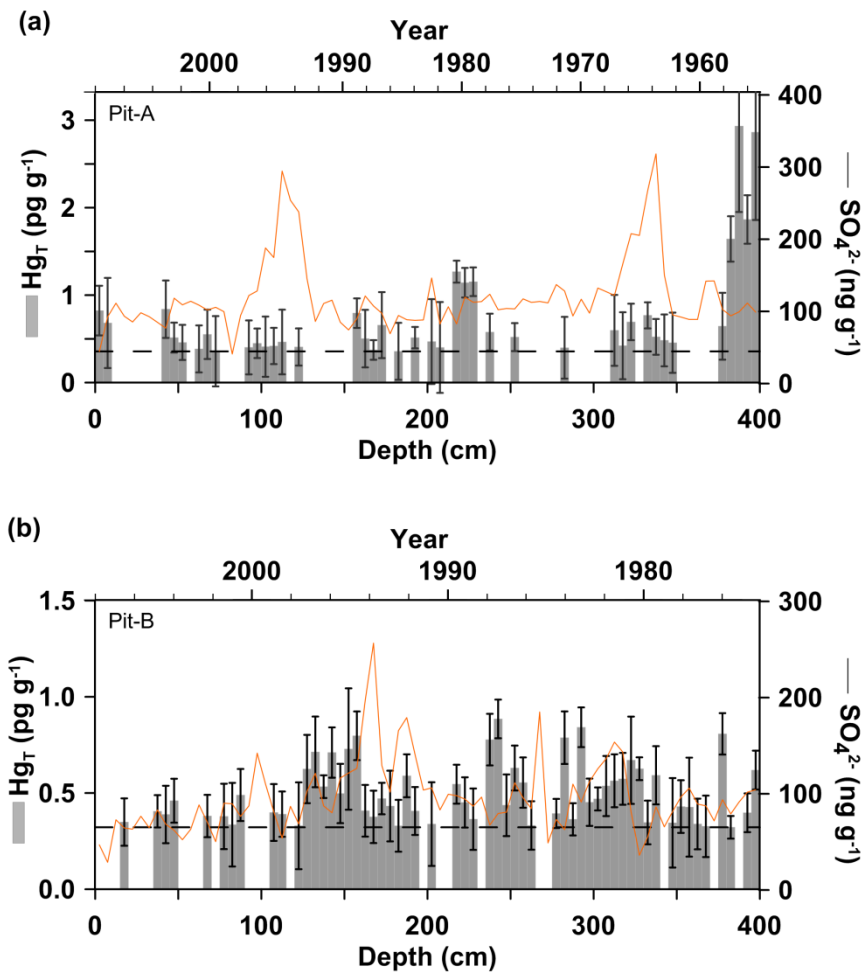


Figure 5-2. The total mercury concentration (bar) profiles with sulfate (line) and a depth-to-age model. The horizontal dotted line represents the detection limits. The results below the detection limits are not shown. The error bars indicate 90% confidence intervals.

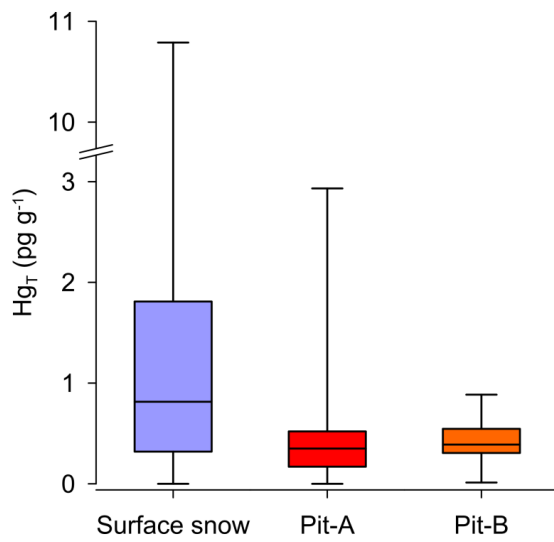


Figure 5-3. The box-whisker plot for the surface snow samples (Han *et al.*, 2011), Pit-A and Pit-B.

Table 5-1. Mercury sequestration rates estimated from Antarctic snowpack or

Location	Distance from coast (km)	Elev (m)	Snow accumulation rate (cm y ⁻¹)	Recovered period	Hg concentration (pg g ⁻¹)	Hg sequestration rate (pg cm ⁻² y ⁻¹)	Analytical method	Sample type	Reference
Dome Fuji (Pit-A)	900	3785	8	1957 - 2007	<0.36 (d.l) - 2.93	1.3	ICP-SF-MS	snow pit	this study
Dome Fuji (Pit-B)	650	3656	12.5	1975 - 2007	<0.32 (d.l) - 0.89	1.9	ICP-SF-MS	snow pit	this study
Commonwealth Glacier, Taylor Valley, Victoria Land	10	678	15	1987 - 2004	0.3 - 40	11	CVAFS with oxidation	snow pit	Witherow and Lyons, 2008
Hercules Névé, Victoria Land	80	2960	38.6	1988 - 1993	0.09 - 0.55 ^a	3.9	CVAFS without oxidation	snow pit	Capelli <i>et al.</i> , 1998
McCarthy Ridge, Victoria Land	40	875	55.0	1990 - 1993	0.16 - 0.71 ^a	10.2	CVAFS without oxidation	snow pit	Capelli <i>et al.</i> , 1998
Dome C	1000	3240	-	3.9 - 33.7 ka	0.19 - 2.21 ^a	0.9 - 3.1	CVAFS without oxidation	ice core	Vandal <i>et al.</i> , 1993
Dome C	1000	3233	-	2 - 672 ka	<1 (d.l) - 65	<1 - 121	ICP-SF-MS	ice core	Jiratu <i>et al.</i> , 2009

^a determined from measure of labile species without pre-oxidation step
ice core

Table 5-2. Total mercury concentrations in each layer of Pit-A and Pit-B. The results below the detection limits are not listed.

Depth (cm)		Pit-A ($\mu\text{g g}^{-1}$)			Pit-B ($\mu\text{g g}^{-1}$)		
top	bottom	concentration	90% CI ^a	Estimated top age	concentration	90% CI ^a	Estimated top age
0	5	0.82	0.28	2008.0	-	-	2008.0
5	10	0.68	0.52	2007.4	-	-	2007.6
10	15	-	-	2006.7	-	-	2007.2
15	20	-	-	2006.1	0.35	0.12	2006.7
20	25	-	-	2005.5	-	-	2006.3
25	30	-	-	2004.8	-	-	2005.9
30	35	-	-	2004.2	-	-	2005.5
35	40	-	-	2003.5	0.41	0.08	2005.0
40	45	0.84	0.33	2002.9	0.39	0.15	2004.6
45	50	0.51	0.17	2002.3	0.46	0.11	2004.2
50	55	0.46	0.20	2001.6	-	-	2003.8
55	60	-	-	2001.0	-	-	2003.3
60	65	0.39	0.27	2000.4	-	-	2002.9
65	70	0.55	0.28	1999.7	0.38	0.11	2002.5
70	75	0.36	0.40	1999.1	-	-	2002.1
75	80	-	-	1998.5	0.38	0.17	2001.6
80	85	-	-	1997.8	0.34	0.22	2001.2
85	90	-	-	1997.2	0.49	0.14	2000.8
90	95	0.40	0.31	1996.5	-	-	2000.4
95	100	0.45	0.17	1995.9	-	-	1999.9
100	105	0.41	0.34	1995.3	-	-	1999.5
105	110	0.42	0.21	1994.6	0.40	0.15	1999.1
110	115	0.46	0.37	1994.0	0.39	0.12	1998.7
115	120	-	-	1993.3	-	-	1998.2
120	125	0.41	0.21	1992.7	0.33	0.23	1997.8
125	130	-	-	1992.0	0.62	0.18	1997.4
130	135	-	-	1991.3	0.71	0.18	1997.0
135	140	-	-	1990.7	0.53	0.06	1996.5
140	145	-	-	1990.0	0.71	0.13	1996.1
145	150	-	-	1989.3	0.50	0.15	1995.7
150	155	-	-	1988.7	0.73	0.32	1995.3
155	160	0.79	0.17	1988.0	0.80	0.13	1994.8
160	165	0.50	0.33	1987.3	0.41	0.13	1994.4
165	170	0.37	0.11	1986.7	0.38	0.14	1994.0
170	175	0.66	0.38	1986.0	0.47	0.08	1993.6
175	180	-	-	1985.3	0.43	0.18	1993.2
180	185	0.36	0.33	1984.7	0.33	0.13	1992.7
185	190	-	-	1984.0	0.59	0.11	1992.3
190	195	0.51	0.12	1983.3	0.41	0.12	1991.9
195	200	-	-	1982.7	-	-	1991.5

Depth (cm)		Pit-A (pg g ⁻¹)			Pit-B (pg g ⁻¹)		
top	bottom	concentration	90% CI ^a	Estimated top age	concentration	90% CI ^a	Estimated top age
200	205	0.47	0.48	1982.0	0.34	0.22	1991.0
205	210	0.40	0.52	1981.3	-	-	1990.6
210	215	-	-	1980.7	-	-	1990.2
215	220	1.27	0.13	1980.0	0.55	0.10	1989.8
220	225	1.14	0.17	1979.3	0.45	0.13	1989.3
225	230	1.15	0.16	1978.7	0.36	0.16	1988.9
230	235	-	-	1978.0	-	-	1988.5
235	240	0.58	0.21	1977.3	0.78	0.13	1988.1
240	245	-	-	1976.7	0.89	0.10	1987.6
245	250	-	-	1976.0	0.44	0.16	1987.2
250	255	0.52	0.16	1975.3	0.63	0.12	1986.8
255	260	-	-	1974.7	0.55	0.13	1986.4
260	265	-	-	1974.0	0.33	0.13	1985.9
265	270	-	-	1973.3	-	-	1985.5
270	275	-	-	1972.7	-	-	1985.1
275	280	-	-	1972.0	0.39	0.08	1984.7
280	285	0.40	0.35	1971.3	0.79	0.14	1984.2
285	290	-	-	1970.7	0.36	0.08	1983.8
290	295	-	-	1970.0	0.84	0.10	1983.4
295	300	-	-	1969.3	0.45	0.12	1983.0
300	305	-	-	1968.7	0.47	0.06	1982.5
305	310	-	-	1968.0	0.54	0.16	1982.1
310	315	0.60	0.41	1967.3	0.56	0.14	1981.7
315	320	0.42	0.38	1966.7	0.57	0.13	1981.3
320	325	0.69	0.21	1966.0	0.67	0.23	1980.8
325	330	-	-	1965.3	0.63	0.06	1980.4
330	335	0.77	0.15	1964.7	0.35	0.11	1980.0
335	340	0.52	0.20	1964.0	0.59	0.15	1979.6
340	345	0.48	0.30	1963.3	-	-	1979.2
345	350	0.46	0.34	1962.7	0.35	0.23	1978.7
350	355	-	-	1962.0	0.43	0.14	1978.3
355	360	-	-	1961.3	0.43	0.26	1977.9
360	365	-	-	1960.7	0.34	0.13	1977.5
365	370	-	-	1960.0	0.33	0.16	1977.0
370	375	-	-	1959.3	-	-	1976.6
375	380	0.64	0.38	1958.7	0.81	0.11	1976.2
380	385	1.64	0.26	1958.0	0.32	0.06	1975.8
385	390	2.93	0.98	1957.3	-	-	1975.3
390	395	1.87	0.28	1956.7	0.40	0.10	1974.9
395	400	2.86	1.00	1956.0	0.62	0.10	1974.5

^a CI is confidence interval. CIs are presented for the results above the detection limits.

Chapter 6

Seasonal and interannual variation in mercury sequestration in Antarctic Plateau snowpack

Han, Y., Huh, Y., Hong, S., Hur, S.D., Motoyama, H., 2012. Records of mercury sequestration in the shallow snow pits of Dome Fuji, Antarctica. *To be submitted.*

Abstract: Temporal variation in mercury (Hg) sequestration recorded within the Antarctic Plateau snowpack reflects change in atmospheric condition that influences the mercury dynamics in the Antarctic interior. At Dome Fuji, we determined Hg concentration in successive snow layers from the surface down to 2 m with a resolution of 2.5 cm, which allowed for examining seasonal and interannual variability of Hg sequestration. The total Hg concentration (Hg_T) varied between 0.12 and 5.19 $pg\ g^{-1}$ ($n = 80$). Relatively high Hg_T were observed during the transition period from the polar night to the sunlit period, when photochemical dynamics of mercury was expected to be just activating. However, strong sea-salt transport during the polar night appeared to be a prerequisite condition. The mercury sequestration rate was $3.3 \pm 0.1\ pg\ cm^{-2}\ yr^{-1}$ on average but displayed a gradual decrease over the last ~24 years, which would stem from reduced poleward transport of sea-salt.

6.1. Introduction

Mercury (Hg) found within the Antarctic Plateau snowpack is considered to be the result of active photochemical interaction between snow and ambient air (Brooks *et al.*, 2008; Han *et al.*, 2011). Among different forms of mercury, gaseous elemental mercury (GEM, Hg^0) has an atmospheric residence time of 6 – 24 months (Schroeder and Munthe, 1998) and is the predominant species transported to the Antarctic Plateau from its remote sources. However, Hg^0 is poorly adsorbed by snow (Bartels-Rausch *et al.*, 2008; Ferrari *et al.*, 2004) and would not significantly contribute to the Hg concentration in the snowpack. Instead, during the sunlit period, a series of photochemical processes switches the oxidation state of mercury between Hg^0 and reactive oxidized species (Hg^{II}) and mediates its bidirectional exchange between the snowpack and the atmosphere. The oxidation of atmospheric GEM produces reactive Hg^{II} that preferentially partitions into snow and substantially elevates Hg concentration in the surface snow up to hundreds pg g^{-1} (Brooks *et al.*, 2008). However, another photochemical process in the snowpack reduces deposited Hg^{II} into Hg^0 , which is re-emitted into the atmosphere (Dommergue *et al.*, 2012). As a result, a part of deposited Hg^{II} is remained within the Antarctic Plateau snowpack (Han *et al.*, 2013).

Hg level in snow could reflect external and internal factors regulating the bidirectional fluxes, by which Hg concentration would vary with depth in response to change in atmospheric conditions. In another aspect,

considering the vast extent of the Antarctic Plateau that represents >3% of the continental surface, the active Hg exchange and fractional sequestration may be significant components of the global mercury cycle (Brooks *et al.*, 2008). However, Hg data are sparse for the Antarctic Plateau snowpack due to difficulties in both sampling and analysis. In our previous study, we reported total mercury concentration (Hg_T) in 4 m snow pit collected at Dome Fuji in the summer of 2008 and interpreted it based on the current understanding of the mercury dynamics (Han *et al.*, 2013). However, Hg_T were found at only sub- to a few pg g^{-1} level, and no notable Hg_T elevation associated with photochemical processes was observed. Accordingly, we suggested that the photochemical contribution to Hg sequestration was not substantial. The low Hg content and its variation within a narrow range imply that precise determination is required for discriminating the variation in Hg content with depth.

It was previously suggested that ICP-SFMS (inductively coupled plasma sector field spectrometry) could provide better performance than conventional cold vapor (CV) generation method for the Hg_T determination. Using ICP-SFMS, consumption of polar snow samples could be reduced (~ a few mL for multiple analyses) and pre-oxidation and reduction steps could be skipped (Jitaru *et al.*, 2009; Planchon *et al.*, 2004). However, it posed problems of high blank to signal ratio caused by the memory effect in the sample introduction system and insufficient precision to discriminate the natural variability at the sub-pg g^{-1} level (Han *et al.*, 2011).

In this study, we report mercury concentrations in a snow pit

sampled every 2.5 cm to a depth of 2 m at Dome Fuji. A refined analytical technique (CV-ICP-SFMS) was applied in order to obtain more precise results and detect the seasonal variation in Hg sequestration, which would be helpful for improving our understanding of mercury dynamics on the Antarctic Plateau.

6.2. Sample description and experimental methods

6.2.1. Sample description

A 2 m deep snow pit was recovered from Dome Fuji (77.39°S, 39.62°E, 3790 m) in Queen Maud Land, East Antarctica in January 2010, during the 51st Japanese Antarctic Research Expedition (Fig. 6-1). The snow pit was successively sampled at 2.5 cm resolution down to 2 m (n = 80) using the sampling protocol previously reported (Hur *et al.*, 2007). The samples were contained in thoroughly pre-cleaned 125 mL PFA bottles double-sealed in acid-cleaned LDPE bags and kept frozen in the dark until further processing. All sampling items were prepared in Korea Polar Research Institute following the ultraclean procedure described in Hong *et al.* (2000).

6.2.2. Instrumentation

Mercury concentrations were determined by ICP-SFMS (Element2, Thermo) using a cold vapor (CV) generator (HGX-200, CETAC) as the sample introduction system at the National Center for Inter-university

Research Facilities at Seoul National University. In CV generator, mercury in the sample solution was reduced by 4% (m/v) SnCl₂ solution and Hg⁰ vapor was directly introduced into ICP-SFMS. The instrument parameters were adjusted as described in Han *et al.* (2011). The flow rate was ~1 ml min⁻¹ and ~ 3 ml of sample was consumed for a single analysis (triplicate of 5 runs × 9 passes).

The major advantage of using the CV generator rather than the conventional nebulizer as the sample introduction system lies in the better signal to blank ratio, which is especially important for the reliable determination at pg g⁻¹ level. The signal to blank ratio expressed by the ratio of instrumental sensitivity (counts per second/(pg g⁻¹)) to blank signal (cps) was ~0.25 (pg⁻¹ g) for the nebulizer system (Han *et al.*, 2011; Planchon *et al.*, 2004) but could be improved up to >2 (pg⁻¹ g) by the CV generation system. An additional merit was that isobaric interferences by polyatomic species (e.g., ¹⁸⁶W¹⁶O vs. ²⁰²Hg) could be neglected, because the vapor phase was selectively injected into the plasma from the CV generator.

Standards for external calibration were prepared by sequential dilution of a single elemental standard of Hg at 1000 mg L⁻¹ in a 10% HNO₃ matrix (ICP standard, Merck) to the range of 0 – 50 pg g⁻¹. The working standard solutions were preserved against Hg loss with 0.5% (v/v) BrCl. The instrument sensitivities indicated by the slopes of calibration curves were ~1800 cps pg⁻¹ g for ²⁰²Hg (r²>0.9999) and ~800 cps pg⁻¹ g for ²⁰¹Hg (r²>0.9999). The accuracy of the calibration curve was verified by analyzing a certified reference material ORMS-4 (elevated Hg in river water, 22.0 ± 1.6

pg g⁻¹ stabilized with 0.5% (v/v) BrCl, NRCC), which showed good recovery with 21.2 ± 1.0 pg g⁻¹ (standard deviation, n = 6). Detection limit estimated as three times the standard deviation of the blank signal (n = 9) were 0.03 pg g⁻¹ and 0.04 pg g⁻¹ for ²⁰²Hg and ²⁰¹Hg, respectively. External reproducibility was evaluated using 5 pg g⁻¹ standard solution in order to correct for instrument sensitivity drift, which was 5.4% (relative standard deviation, n=20) over the course of the analysis.

6.2.3. Reagents and blanks

BrCl and SnCl₂ solutions were prepared based on EPA method 245.7. BrCl solution was prepared just prior to use by mixing bromate/bromide solution and concentrated hydrochloric acid (HCl, Optima grade, Fisher) (1:1 v/v). To produce bromate/bromide solution, 2.78 g KBrO₃ (ACS reagent, ≥99.8%, Sigma-Aldrich) and 11.90 g KBr (ACS reagent, ≥99.0%, Sigma-Aldrich) were preheated at 250°C for >8 hours to volatilize mercury impurities and dissolved in 500 mL deionized water (DI water). Hg impurity in BrCl solution was 28.1 ± 7.5 pg g⁻¹ (n = 7), equivalent to 0.14 ± 0.3 pg g⁻¹ in sample solution when added to a final concentration of 0.5% (v/v). A 4% (w/v) SnCl₂ (reagent grade, 98%, Sigma-Aldrich) used as the reducing agent in the CV generator was prepared in 3% (v/v) HCl (HP-100H, Eco Research) and purged with pure N₂ gas (>99.9999%) for 30 minutes to eliminate trace Hg in the solution.

The Hg level in DI water was below the detection limit (0.03 pg g⁻¹) and indistinguishable from purged DI water with SnCl₂. The analytical blank

was determined by analyzing DI water between each sample and subtracted from the sample signal.

6.2.4. Sample preparation

The snow samples were melted at room temperature in a class 100 clean hood and divided into two 8-mL Teflon-lined glass vials (Wheaton) pre-cleaned following EPA method 245.7. One vial was immediately analyzed without pre-oxidation step to avoid potential volatilization of Hg^{2+} from the snowmelt. This method determines labile Hg species (mostly Hg^{2+}) reducible within the CV generator ($[\text{Hg}^{2+}]$, hereafter). Another vial was digested overnight with 0.5% (v/v) BrCl to recover total mercury in the snowmelt and then analyzed. The amount of sample solution and added BrCl were weighed in order to accurately correct for BrCl impurity. The procedural blank determined from artificial samples of DI water was below the detection limit. Sample reproducibility was examined by snowmelt samples ($n = 10$) aliquoted into three different vials. Hg_T and $[\text{Hg}^{2+}]$ results coincided within 8.6% and 16%, respectively.

6.2.5 Depth-to-age model

If the mean snow accumulation rate of $\sim 27 \text{ kg m}^{-2} \text{ yr}^{-1}$ at Dome Fuji is considered (Kameda *et al.*, 2008), our sampling interval of 2.5 cm corresponds to about 3 – 4 months and is adequate to examine sub-annual variation in Hg sequestration. To build depth-to-age relationship an outstanding sulfate (SO_4^{2-}) peak of Mt. Pinatubo eruption (1991) at 147.5 cm

was set as a reference point (Fig. 6-2g). The mercury profile was compared to Na^+ concentration, Cl/Na ratio, oxygen isotope data ($\delta^{18}\text{O}$) and total ozone contents, in order to look into the seasonal and interannual variability of Hg sequestration. The age model is adjusted by the seasonal layers retrieved from the Na^+ , Cl/Na and $\delta^{18}\text{O}$ profiles (Fig 6-2, between b and c). The ionic concentrations and oxygen isotope composition were determined every 2.5 cm at Korea Polar Research Institute using ion chromatography (ICS-2000, DIONEX) and liquid water isotope analysis (L1102-i, PICARRO), respectively. Total column ozone and surface UV-B irradiation at Syowa station were from the Japan Meteorological Agency web page (<http://www.data.kishou.go.jp>).

6.3. Results

The results of Hg_T and $[\text{Hg}^{2+}]$ were $0.12 - 5.19 \text{ pg g}^{-1}$ and $<0.04 - 1.83 \text{ pg g}^{-1}$, respectively (Fig. 6-2), which were all within the range previously reported for the Antarctic snow (Han *et al.*, 2011 and references therein). A good correlation ($r = 0.91$) was found between Hg_T and $[\text{Hg}^{2+}]$. This reflects that mercury is predominantly present in the inorganic forms in the samples and only a part of mercury is reduced by the CV system without the oxidation step. The Hg concentration was higher in the deeper layers than the upper layers, with a maximum peak at $\sim 180 \text{ cm}$, gradual decrease with large fluctuation between $180 - 140 \text{ cm}$, and relatively stable level from 140 cm to

the top except a sudden increase at ~75 cm. We applied an empirical snow depth (z)-density (ρ) equation for Dome Fuji, $\rho(z) = 0.408 - 0.118\exp(-z/172)$ (Takahashi and Kameda, 2007) to calculate the mean mercury sequestration rate, which was $3.3 \pm 0.1 \text{ pg cm}^{-2} \text{ yr}^{-1}$ during ~24 years. The concentrations and sequestration rates of Hg_T were slightly higher than our previous estimates of $1.3 \text{ cm}^{-2} \text{ yr}^{-1}$ (Han *et al.*, 2013). The underestimation in the previous study can be ascribed to potential Hg loss during sample preparation and low level of Hg_T in the sample varying around the detection limit ($\sim 0.4 \text{ pg g}^{-1}$). However, both results are consistent in that relatively high Hg_T are more frequent in the deeper layers.

6.4. Discussion

The precise determination of Hg_T from densely and successively sampled snow layers clearly exhibits the temporal change of mercury sequestration in the Antarctic Plateau snowpack during the period covered by the snow pit. Since most mercury is expected to be present as oxidized form in the snowpack, the temporal variation would stem from the photochemistry of mercury that could produce Hg^{II} . Specifically, the following questions will be addressed: (1) What controls the Hg concentrations in the snowpack? (2) Does it have seasonality and what season does it peak?

The most striking observation associated with (1) is that relatively high Hg_T occurred closely after the elevations of Na, except few layers below

100 cm in that they were concurrent (Fig. 6-2). In addition, both Hg_T and Na profiles broadly displayed upward-decreasing trends. Then, since sea-salt is the major source of Na in the Antarctic interior, sea-salt is expected to somehow play a role in the elevation of Hg_T in the snowpack, which will be further discussed.

With respect to (2), the Na profile additionally provides a clue to the seasonality of Hg_T . Because the transport of sea-salt is stronger during the winter than during the summer at the Dome Fuji (Hara *et al.*, 2004), the fluctuation of Na would reflect the seasonal variation of the sea-salt transport to this site. This can be evidenced by the oxygen isotope ratio ($\delta^{18}O$) of snow, which has a strong seasonality resulting from its positive relationship with the air temperature (Fujita and Abe, 2006). $\delta^{18}O$ in the snow pit varied within a narrower range (-64 – -50‰; Fig. 6-2) than freshly fallen snow (-82 – -33‰; (Fujita and Abe, 2006)), mainly due to post-depositional redistribution of surface snow (Motoyama *et al.*, 2005). However, the mirroring trend between $\delta^{18}O$ and Na claims that the snow pit had preserved the seasonal records. Then, it is evident that Hg sequestration has seasonality. Above 142.5 cm, the Hg_T peaks follow after the winter layers. Accordingly, we suggest that the Hg peaks correspond to the transitional period from the winter to the summer. Below 142.5 cm, the layer-by-layer fluctuations are common to Hg_T , Na and $\delta^{18}O$ and hence would reflect the seasonal variations of them. They might be caused by snowpack densification and comparatively low snow accumulation. As a consequence, the Hg peaks appear concurrently with the summer or the winter peaks of others by our sampling resolution. Interestingly, Hg_T in the

snowpack peaks earlier than atmospheric Hg^{II} that reaches its maximum during the late summer (Jan – Feb) in response to the active photochemistry (Brooks *et al.*, 2008). This would indicate that deposition of atmospheric Hg^{II} exceeds emission of Hg^0 during the early summer. On the contrary, in spite of active atmospheric oxidation, more intense reemission equivalent to or greater than the deposition would cause relative Hg depletion in snow during the summer. This means the snowpack undergoes conversion from the sink to the source of mercury in the sunlit period. From the observations with respect to (1) and (2), it can be induced that Hg sequestration is largely controlled by sea-salt and, as a consequence, has seasonality with its maximum during the transitional period from the winter to the summer.

Another characteristic with respect to the seasonality of Hg emerges from the comparison with Cl/Na ratio in snow. Sea-salt is the major source of Na^+ and Cl^- with the ratio of Cl/Na (w/w) = 1.8. However, Cl/Na ratio in snowpack is normally higher than the sea-salt ratio (Fig. 6-2), because Cl^- is comparatively volatile and subject to recycling whereas Na^+ is immobile within the snowpack (Hara *et al.*, 2004; Iizuka *et al.*, 2004). Then, abundant sea-salt transport to Dome Fuji elevates Na^+ concentration and lowers the Cl/Na ratio close to 1.8 in snow. The highest sea-salt contribution can be found at 70.0 – 82.5 cm and 160.0 – 177.5 cm, which coincide with the intervals of the conspicuous Hg peaks.

The role of sea-salt can be further highlighted by that all Hg, Na^+ and Cl/Na display gradual decrease from the bottom toward shallower layers. The actual and relative decrease in sea-salt content of the recently deposited layers

would indicate the reduction of the poleward atmospheric transport, which carries sea-salt from the lower latitudes to the Antarctic Plateau. There are two important mechanisms that can modulate the poleward atmospheric transport.

Fundamentally, the polar vortex can isolate Antarctic air mass from the exterior with the strong zonal circulation. Both field observations of aerosol concentration (e.g., Herber *et al.* 1996) and particle dispersion and air mass back trajectory models (Stohl and Sodemann, 2010; Suzuki *et al.*, 2008) well reveal the stagnancy of Antarctic air mass, showing that the poleward transport across the polar vortex is unfavorable and has a long travel time extending up to a few weeks. Then, intensity of the polar vortex can be a key factor influencing the poleward atmospheric transport to the Antarctic Plateau in where the upper air subsidence prevails (Stohl and Sodemann, 2010). In general, the polar vortex has an annual cycle of gradual development during the polar night until its maximum intensity in late winter, followed by a sudden breakdown in the spring and dissipation in the summer. The intensity of the polar vortex has largest interannual variance during the spring season in response to the substantial year-to-year variation in the timing of the polar vortex breakdown (Black and McDaniel, 2007; Thompson *et al.*, 2005). In addition, this positive/negative anomaly of the polar vortex intensity during the spring can extend to the summer season (Thompson *et al.*, 2005; Thompson *et al.*, 2011), spanning the photochemically active period.

To reconstruct the relative variation in the polar vortex intensity, we introduce Southern Annular Mode (SAM) index (Marshall, 2003) and total column ozone (Fig. 6-2). It is generally agreed that positive SAM stemming

from larger pressure gradient between lower and higher latitudes can derive stronger polar vortex. In our context, then, positive SAM can be translated to the reduction of the poleward atmospheric transport. Total column ozone provides more direct information on the timing of the polar vortex breakdown, because the earlier breakdown allows for earlier restoration of the ozone hole via ozone transfer from lower latitudes. Both SAM and total ozone column indicate gradual strengthening of the polar vortex during the period that our snow pit covers, which can explain the gradual reduction of sea-salt transport and Hg concentration. The variation in polar vortex intensity can also explain sudden peaks of Na⁺ and Hg at ~75 cm, consistent with the most extreme weakening of the polar vortex in the early spring in 2002.

The anomaly of the polar vortex intensity also has an influence on the surface meteorological conditions such as temperature, pressure, wind speed and precipitation (Thompson *et al.*, 2011; van den Broeke and van Lipzig, 2004). This earlier restoration would be expected to affect the UV flux and associated photochemistry over the Antarctic Plateau; however, the degree to which the mercury dynamics depend on surface meteorological conditions and UV flux has to be further investigated.

On the other hand, it is known that a blocking anticyclone could lead to the advection of warm and moist air masses at the synoptic scale, which would also bring abundant sea-salt from the lower latitudes to the Antarctic interior (Enomoto *et al.*, 1998; Massom *et al.*, 2004). It occurs intermittently throughout the year, but less frequently during the warm period (Schlosser *et al.*, 2010). Once formed it persists over a period of few days to several weeks

and promotes episodic snowfall over a wide expanse of Antarctica (Massom *et al.*, 2004; Schlosser *et al.*, 2010). This type of snowfall is relatively heavy, so it accounts for only ~5% of the days but about half the amount of the annual precipitation (Fujita and Abe, 2006; Schlosser *et al.*, 2010). The blocking anticyclone supports atmospheric transport and would in turn contribute to the related mercury dynamics. For instance, despite coincidence of Hg peak at ~75 cm with the extreme weakening of the polar vortex, seasonal indicators of $\delta^{18}\text{O}$, Na^+ and Cl/Na strongly suggest that there is a heavy snowfall event during the winter season rather than after the polar vortex breakdown during the spring. The heavy snowfall with abundant sea-salt component can result from the abrupt transport of moist air masses from the sea, which represent a possible case driven by a blocking anticyclone. However, the annual frequency of the blocking event is thought to largely vary widely year-to-year (Schlosser *et al.*, 2010) and observation is insufficient to address its long-term trends and impacts on the interannual Hg_T variation, for which further investigation is necessary.

6.5. Conclusion

We present Hg concentration data for a 2 m snow pit densely sampled every 2.5 cm to look into the seasonal and interannual variation in Hg sequestration in Antarctic Plateau snowpack. Hg concentration displays clear seasonal variation with the maximum during the transition period from

the winter to the summer. Although the increase of Hg concentration would be associated with photochemical processes, it appears that the strong sea-salt transport during the winter is prerequisite factor. We propose that the gradual decrease of sea-salt concentration and subsequent Hg sequestration results from reduced atmospheric poleward transport.

6.6. References

- Bartels-Rausch, T., Huthwelker, T., Jöri, M., Gäggeler, H., Ammann, M., 2008. Interaction of gaseous elemental mercury with snow surfaces: laboratory investigation. *Environmental Research Letters* 3(4).
- Black, R.X., McDaniel, B.A., 2007. Interannual variability in the Southern Hemisphere circulation organized by stratospheric final warming events. *Journal of the Atmospheric Sciences* 64(8), 2968-2974.
- Brooks, S., Arimoto, R., Lindberg, S., Southworth, G., 2008. Antarctic polar plateau snow surface conversion of deposited oxidized mercury to gaseous elemental mercury with fractional long-term burial. *Atmospheric Environment* 42(12), 2877-2884.
- Dommergue, A., Barret, M., Courteaud, J., Cristofanelli, P., Ferrari, C., Gallée, H., 2012. Dynamic recycling of gaseous elemental mercury in the boundary layer of the Antarctic Plateau. *Atmospheric Chemistry and Physics* 12(22), 11027-11036.
- Enomoto, H., Motoyama, H., Shiraiwa, T., Saito, T., Kameda, T., Furukawa,

- T., Takahashi, S., Kodama, Y., Watanabe, O., 1998. Winter warming over Dome Fuji, East Antarctica and semiannual oscillation in the atmospheric circulation. *Journal of Geophysical Research* 103(D18), 23,103-23,111.
- EPA, 245.7 Mercury in Water by Cold Vapor Atomic Fluorescence Spectrometry.
- Ferrari, C.P., Dommergue, A., Boutron, C.F., Jitaru, P., Adams, F.C., 2004. Profiles of Mercury in the snow pack at Station Nord, Greenland shortly after polar sunrise. *Geophysical Research Letters* 31(3), L03401.
- Fujita, K., Abe, O., 2006. Stable isotopes in daily precipitation at Dome Fuji, East Antarctica. *Geophysical Research Letters* 33(L18503).
- Han, Y., Huh, Y., Hong, S., Hur, S.D., Motoyama, H., Fujita, S., Nakazawa, F., Fukui, K., 2011. Quantification of total mercury in Antarctic surface snow using ICP-SF-MS: spatial variation from the coast to Dome Fuji. *Bulletin of the Korean Chemical Society* 32(12), 4258-4264.
- Han, Y., Huh, Y., Hur, S.D., Hong, S., Motoyama, H., 2013. Records of mercury sequestration in the shallow snow pits of Dome Fuji, Antarctica. in preparation.
- Hara, K., Osada, K., Kido, M., Hayashi, M., Matsunaga, K., Iwasaka, Y., Yamanouchi, T., Hashida, G., Fukatsu, T., 2004. Chemistry of sea-salt particles and inorganic halogen species in Antarctic regions: Compositional differences between coastal and inland stations. *Journal of Geophysical Research* 109(D20208).

- Herber, A., Thomason, L.W., Dethloff, K., Viterbo, P., Radionov, V.F., Leiterer, U., 1996. Volcanic perturbation of the atmosphere in both polar regions: 1991-1994. *Journal of Geophysical Research* 101(D2), 3921-8.
- Hong, S., Lluberas, A., Rodriguez, F., 2000. A clean protocol for determining ultralow heavy metal concentrations: Its application to the analysis of Pb, Cd, Cu, Zn and Mn in Antarctic snow. *Korean Journal of Polar Research* 11, 35-47.
- Hur, S.D., Cunde, X., Hong, S., Barbante, C., Gabrielli, P., Lee, K., Boutron, C.F., Ming, Y., 2007. Seasonal patterns of heavy metal deposition to the snow on Lambert Glacier basin, East Antarctica. *Atmospheric Environment* 41(38), 8567-8578.
- Iizuka, Y., Fujii, Y., Hirasawa, N., Suzuki, T., Motoyama, H., Furukawa, T., Hondoh, T., 2004. SO_4^{2-} minimum in summer snow layer at Dome Fuji, Antarctica, and the probable mechanism. *Journal of Geophysical Research* 109(D04307).
- Jitaru, P., Gabrielli, P., Marteel, A., Plane, J.M.C., Planchon, F.A.M., Gauchard, P.A., Ferrari, C.P., Boutron, C.F., Adams, F.C., Hong, S., Cescon, P., Barbante, C., 2009. Atmospheric depletion of mercury over Antarctica during glacial periods. *Nature Geoscience* 2(7), 505-508.
- Kameda, T., Motoyama, H., Fujita, S., Takahashi, S., 2008. Temporal and spatial variability of surface mass balance at Dome Fuji, East Antarctica, by the stake method from 1995 to 2006. *Journal of*

Glaciology 54, 107-116.

Marshall, G.J., 2003. Trends in the Southern Annular Mode from observations and reanalyses. *Journal of Climate* 16(24), 4134-4143.

Massom, R.A., Pook, M.J., Comiso, J.C., Adams, N., Turner, J., Lachlan-Cope, T., Gibson, T.T., 2004. Precipitation over the interior East Antarctic ice sheet related to midlatitude blocking-high activity. *Journal of Climate* 17(10), 1914-1928.

Motoyama, H., Hirasawa, N., Satow, K., Watanabe, O., 2005. Seasonal variations in oxygen isotope ratios of daily collected precipitation and wind drift samples and in the final snow cover at Dome Fuji Station, Antarctica *Journal of Geophysical Research* 110(D11), D11106.

Planchon, F.A.M., Gabrielli, P., Gauchard, P.A., Dommergue, A., Barbante, C., Cairns, W.R.L., Cozzi, G., Nagorski, S.A., Ferrari, C.P., Boutron, C.F., Capodaglio, G., Cescon, P., Varga, A., Wolff, E.W., 2004. Direct determination of mercury at the sub-picogram per gram level in polar snow and ice by ICP-SFMS. *Journal of Analytical Atomic Spectrometry* 19(7), 823-830.

Schlosser, E., Manning, K., Powers, J., Duda, M., Birnbaum, G., Fujita, K., 2010. Characteristics of high-precipitation events in Dronning Maud Land, Antarctica *Journal of Geophysical Research* 115, D14107.

Schroeder, W.H., Munthe, J., 1998. Atmospheric mercury – An overview. *Atmospheric Environment* 32(5), 809-822.

Stohl, A., Sodemann, H., 2010. Characteristics of atmospheric transport into the Antarctic troposphere. *Journal of Geophysical Research*

115(D02305).

- Suzuki, K., Yamanouchi, T., Motoyama, H., 2008. Moisture transport to Syowa and Dome Fuji stations in Antarctica. *Journal of Geophysical Research* 113(D24114).
- Takahashi, S., Kameda, T., 2007. Instruments and methods - snow density for measuring surface mass balance using the stake method. *Journal of Glaciology* 53(183), 677-680.
- Thompson, D.W.J., Baldwin, M.P., Solomon, S., 2005. Stratosphere-troposphere coupling in the Southern Hemisphere. *Journal of the Atmospheric Sciences* 62(3), 708-715.
- Thompson, D.W.J., Solomon, S., Kushner, P.J., England, M.H., Grise, K.M., Karoly, D.J., 2011. Signatures of the Antarctic ozone hole in Southern Hemisphere surface climate change. *Nature Geoscience* 4(11), 741-749.
- van den Broeke, M.R., van Lipzig, N.P.M., 2004. Changes in Antarctic temperature, wind and precipitation in response to the Antarctic Oscillation. *Annals of Glaciology* 39(1), 119-126.

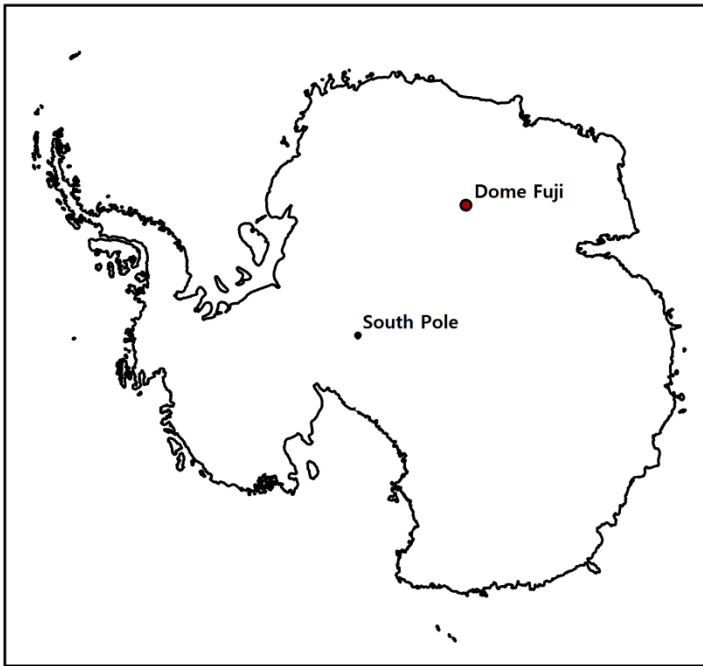


Figure 6-1. The sampling locations for the 2 m snow pit.

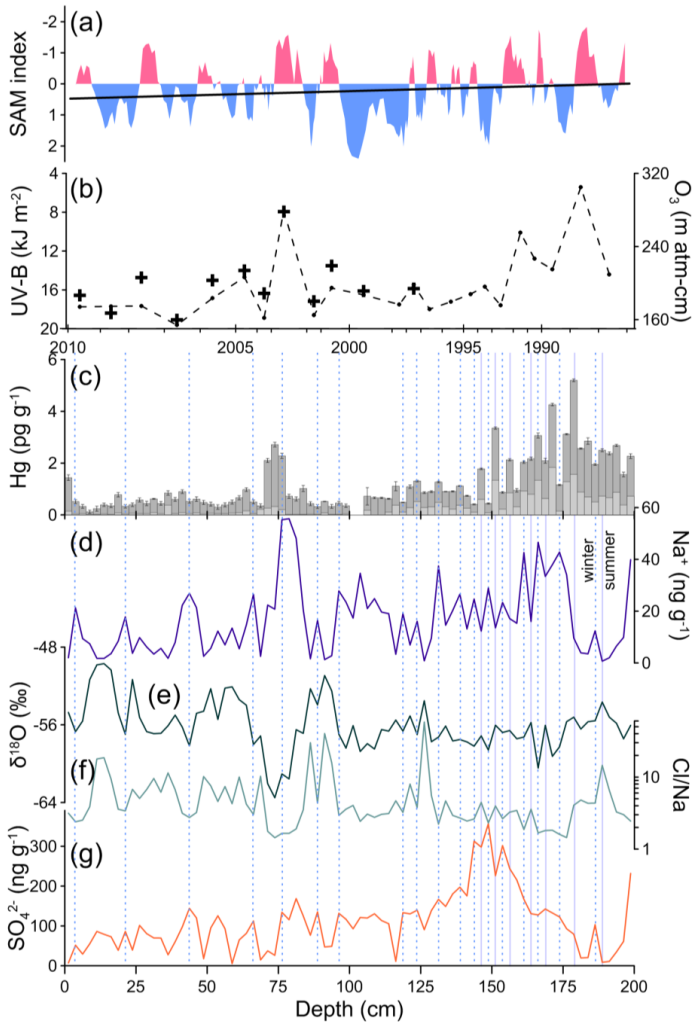


Figure 6-2. (a) 3-month running average (color area) and linear regression line of Southern Annular Mode index (b) Total ozone column (solid line) and surface UV-B flux (cross) at Syowa station, averaged for September – October. (c) Total (darker) and labile (Hg^{2+} , pale) mercury concentrations in each 2.5 cm layer. Two samples for 100 – 105 cm depths are missed. (d) – (g) compositions for Na^+ , $\delta^{18}\text{O}$, Cl/Na and SO_4^{2-} . The seasonal layers for the winter (dotted) and summer (solid) are indicated. Above 142.5 cm, only the winter layers are designated.

PART III

Chapter 7

High resolution authigenic $^{10}\text{Be}/^9\text{Be}$ and detrital
 $^{176}\text{Hf}/^{177}\text{Hf}$ records of marine sediment on the Bowers
Ridge during 32 – 40 ka

7.1. Introduction

Changes in seawater composition are considered to be recorded in the authigenic fraction of marine sediments as it directly precipitates from the seawater. The $^{10}\text{Be}/^9\text{Be}$ ratio of the seawater is controlled by different delivery mechanisms of each isotope. Stable ^9Be , present in continental crust at a few ppm levels, is supplied by riverine input as a weathering product. On the other hand, radioactive ^{10}Be ($t_{1/2} = 1.5 \text{ Ma}$) is mainly produced in the upper atmosphere by spallation reaction induced by cosmic ray. The atmospheric ^{10}Be is delivered to the ocean through the dry/wet deposition and hydrological cycle. Beryllium is particle reactive with a residence time of 500-1000 years in seawater and undergoes sorption and remineralization until deposition. This enables us to reconstruct millennial-scale variations in the $^{10}\text{Be}/^9\text{Be}$ ratio of seawater.

The $^{10}\text{Be}/^9\text{Be}$ ratio has been applied as a proxy for the change of the paleo-geomagnetic field. For example, during the Laschamp excursion ($40.7 \pm 1.0 \text{ ka}$; Singer *et al.*, 2009), the geomagnetic field intensity was greatly reduced for 1500 – 2000 years (Laj *et al.*, 2006) and production of cosmogenic isotopes including ^{10}Be accordingly increased, which were globally recorded in the marine sediment cores (Leduc *et al.*, 2006). This enables using a $^{10}\text{Be}/^9\text{Be}$ peak as an age tie point in the depth profile of a marine sediment core.

Hafnium-176 (^{176}Hf) is produced by a beta decay of ^{176}Lu . Since

hafnium (Hf) and lutetium (Lu) partition differently into rock-forming minerals, the $^{176}\text{Hf}/^{177}\text{Hf}$ ratios in those minerals evolve differently over time. This decoupling between Lu and Hf at the mineral scale provides a potential means for tracing provenance and transport of detrital particles in marine sediment.

In this chapter, by determining authigenic $^{10}\text{Be}/^9\text{Be}$ and detrital $^{176}\text{Hf}/^{177}\text{Hf}$ ratio from marine sediments on the Bowers Ridge in the Bering Sea, various factors that affect these ratios will be discussed. This would be helpful for understanding the sedimentation environment in this region.

7.2. Method

7.2.1. Sample description

The Bering Sea is the northern marginal sea of the Pacific Ocean. It is the third largest marginal sea in the world with an area of $2.29 \times 10^6 \text{ km}^2$. Marine sediment cores (~600 m) were obtained at Site U1341 ($54^\circ 24.00 \text{ N}$, $179^\circ 0.49 \text{ E}$, water depth 2139 m) on the Bowers Ridge during IODP (Integrated Ocean Drilling Program) Expedition 323 “Pliocene-Pleistocene paleoceanography and climate history of the Bering Sea” (Fig. 7-1). The average sedimentation rate was estimated to be $\sim 14 \text{ cm kyr}^{-1}$ at this site during the past 60 kyr (Takahashi 2005). The samples were selected within the interval of 4.87 – 6.80 m (CCSF-A).

Depth-age model is constructed based on $\delta^{18}\text{O}$ profiles of benthic

foraminifera and peak matching that constrained the age tie points (T. Sakamoto, personal communication). Linear interpolation was applied for the intervals between the age tie points. One of the age tie points at 37.8 ka is designated in Fig. 7-2. According to the age model, the sedimentation rate appeared to be much higher at $\sim 25.3 \text{ cm ky}^{-1}$ during about 32 – 40 ka covered by the sample interval than the mean rate during the past 60 ka.

7.2.2. Extraction of the authigenic fraction and determination of $^{10}\text{Be}/^9\text{Be}$ ratio

The extraction of the authigenic fraction was carried out based on Bourles *et al.* (1989). About 1 g of freeze-dried and crushed sediment was reacted with a mild leaching solution of 0.04 M hydroxylamine hydrochloride (99.9999%, Sigma-Aldrich) in 25% acetic acid (for trace analysis, Sigma-Aldrich) in a shaking bath at $\sim 95 \pm 2^\circ\text{C}$ for 6 hours. An aliquot (0.5 mL) from the leachate was set aside and used to determine the total beryllium concentration using ICP-SF-MS (Element 2, Thermo Scientific) at National Center for Inter-University Research Facilities (NCIRF) in the Seoul National University campus. The remaining leachate was spiked with 0.5 mg of ^9Be (Merck) as a carrier, and then beryllium was purified through solvent extraction. The dissolved beryllium in liquid was precipitated into beryllium hydroxide, which was converted to beryllium oxide in a furnace at 750°C . The $^{10}\text{Be}/^9\text{Be}$ ratio was determined using an accelerated mass spectrometer (AMS, 4110Bo-AMS, 3 MeV, High Voltage Engineering Europa) at the Korea Institute of Geology and Mineral Resources. The propagated 1σ uncertainty in the concentrations for ^{10}Be was on average 0.8% (0.5 – 2.1%) and for ^9Be was

4.6% (1.1 – 9.6%). The residual sediment was rinsed three times with deionized water and dried in an oven.

7.2.3. Dissolution of the detrital fraction and determination of $^{176}\text{Hf}/^{177}\text{Hf}$

Complete dissolution of the residual sediment was achieved by applying the alkaline fusion method based on Bayon *et al.* (2009a). Approximately 0.1 g of the sample was taken in a glassy carbon beaker (SIGRADUR G-beaker and G-lids type GAB 3, HTW Hochtemperatur-Werkstoffe GmbH) with 1.2 g Na_2O_2 (>95%, ACS grade, Sigma-Aldrich) and 0.6 g NaOH (>98.0%, pellet, ACS grade, Sigma-Aldrich). They were fused in a muffle furnace at 650°C for 15 minutes and cooled at room temperature for ~3 minutes. About 10 mL of deionized water (DI, Puris Esse, UP Academic, Marae Co with additional trace metal filter cartridge) was added, and the melt was transferred into a PFA beaker (50 mL, Savillex). The remaining melt and precipitates were rinsed with DI into the PFA beaker, which were heated on a hotplate at 130°C for two hours. After complete co-precipitation of Hf with Fe-(Ti) (oxy)hydroxides, the sample was centrifuged for 5 min at 5000 rpm. The supernatant was discarded, and the precipitates were cleaned with DI twice, dissolved in 3 mL of 4 M HF solution and centrifuged. Then the supernatant was prepared for the next step.

Hafnium is required to be separated from interfering elements before analysis. Two columns were employed for the purification of Hf – the anion exchange column and Ln column (Table 7-1), which were modified from Chu *et al.* (2002). The fluorinated sample (in 3 mL of 4 M HF) was loaded onto the

anion exchange column (10 mL Bio-Rad Poly-Prep columns) prepared with 0.8 mL anion exchange resin (Biorad AG1-x8 200-400 mesh). Elements that do not form fluoride complex were eluted by 10 mL of 4 M HF solution. Then, hafnium was recovered by 8 mL of 6 M HCl-1 M HF (Fig. 7-2a). Hf was further purified by the Ln column, which was prepared with a PFA column (15 mL Savillex microcolumn, 4 mm inner diameter) packed with 0.7 mL Ln resin (50 - 100 mesh, Eichrom). The sample collected from the first column was evaporated to a small drop and diluted in 0.1 mL of 2.2 M HCl-1%(v/v) H₂O₂. The addition of hydrogen peroxide forms the yellow-tinted peroxytitanyl compound (Ti(O-O)²⁺) and provide a satisfactory separation of Hf and Ti (Chu *et al.*, 2002). This compound and heavy rare earth elements (HREE) were eluted by 3.9 mL of 2.2 M HCl-1%(v/v) H₂O₂ and 12 mL of 6 M HCl. Then Hf was recovered by 8 mL of 1 M HF. The collected solution was evaporated to a drop, diluted in 2 mL of 1%(v/v) HNO₃-0.01%(v/v) HF and analyzed for ¹⁷⁶Hf/¹⁷⁷Hf using a multi collector inductively-coupled plasma mass spectrometer (MC-ICP-MS, Neptune, Thermo-scientific) at Korea Basic Science Institute. ¹⁷⁶Hf/¹⁷⁷Hf ratio of a 100 ppb JMC-475 solution and its external reproducibility was 0.282159 ± 6 (2 × standard deviation, n = 6). AMES standard solution and BHVO rock were treated as samples and their ¹⁷⁶Hf/¹⁷⁷Hf were determined to be 0.282160 ± 27 (n = 5) and 0.283102 ± 15 (n = 2), comparable to previously reported values of 0.282146 ± 30 and 0.283103 ± 27. The reference values were obtained from the GeoReM website (<http://georem.mpch-mainz.gwdg.de/>). The external reproducibility for triplicate analyses of a sample was typically between

0.000001 – 0.000027 (n = 4).

7.3. Results and discussion

The authigenic $^{10}\text{Be}/^9\text{Be}$ ratio with individual concentrations of ^{10}Be and ^9Be and detrital $^{176}\text{Hf}/^{177}\text{Hf}$ ratio are given in Fig 7.2, together with the shipboard paleomagnetic data.

The authigenic $^{10}\text{Be}/^9\text{Be}$ ratio ranged from 3.0 to 8.3×10^{-8} (n = 16) with an average of 5.6×10^{-8} . The ratios were highest in the upper part of the profile with a gradual increase in ^{10}Be concentration (Fig. 7-2a and b). The abrupt enhancements of ^9Be led to the negative anomalies of $^{10}\text{Be}/^9\text{Be}$ at around 37 and 38 ka (Fig. 7-2a – c).

The detrital $^{176}\text{Hf}/^{177}\text{Hf}$ ratio is expressed as ϵ notation, defined by $\epsilon_{\text{Hf}} = ((^{176}\text{Hf}/^{177}\text{Hf})_{\text{sample}} / (^{176}\text{Hf}/^{177}\text{Hf})_{\text{CHUR}} - 1) \times 10^4$, where CHUR stands for chondritic uniform reservoir and $(^{176}\text{Hf}/^{177}\text{Hf})_{\text{CHUR}} = 0.282772$ (Bayon *et al.*, 2009b). ϵ_{Hf} varied between 4.7 and 7.9 (Fig. 7-2d). All values lay among the rock compositions of surrounding continents and islands: Siberia ($\epsilon_{\text{Hf}} = -3 - +4$), Alaska ($\epsilon_{\text{Hf}} = +7 - +10$), Aleutian ($\epsilon_{\text{Hf}} = +13 - +17$) and Kamchatka ($\epsilon_{\text{Hf}} = +13 - +17$) (Fig. 7-3). This is consistent with a previous study, which explain the detrital material on the Bowers Ridge as a mixture of radiogenic sources from Aleutian/Kamchatka and relatively unradiogenic sources from Alaska/Siberia based on the neodymium and strontium isotopic ratios (Horikawa *et al.* 2010). Interestingly, the significant changes of detrital ϵ_{Hf}

accompanied those of authigenic ^9Be concentration at around 33, 37 and 38 ka (Fig. 7-2c – d), which could point to a common origin for authigenic and detrital fractions in the marine sediments.

7.3.1. Rate of authigenic beryllium burial

The rate of authigenic beryllium burial is calculated using the mean sedimentation rate of 25.3 cm ky^{-1} derived from the depth-age model (Fig. 7-2). Dry density is assumed to be 0.5 g cm^{-3} based on the shipboard moisture and density (MAD) data. Then, the sedimentation rates of ^9Be and ^{10}Be are calculated to be $7.0 - 15 \times 10^{13}$ and $4.1 - 10 \times 10^6 \text{ atoms cm}^2 \text{ y}^{-1}$, respectively. Although the riverine input of beryllium is unknown, the authigenic ^{10}Be burial was 4 – 9 times faster than the deposition of the atmospheric ^{10}Be to the sea surface estimated to be $\sim 350 \text{ atoms cm}^2 \text{ s}^{-1}$ ($\sim 1.1 \times 10^6 \text{ atoms cm}^2 \text{ y}^{-1}$; Fig. 7-4; Heikkilä and Beer, in preparation).

The burial of authigenic ^{10}Be could be advanced by its elevated production in the atmosphere in response to the increase in the cosmic ray influx. During 32 – 40 ka, the atmospheric production of ^{10}Be indeed seemed to be comparatively higher than the present (Carcaillet *et al.*, 2004).

Another mechanism that could enhance the ^{10}Be sedimentation is the active “boundary scavenging” (Anderson *et al.*, 1990), which refers to preferential scavenging of insoluble elements by particulate matters at ocean margins. Beryllium is a particle reactive element, and its efficient scavenging at the sampling site is evidenced by its nutrient-like vertical profile in the water columns (Fig. 7-5b) and the coupling between authigenic ^9Be and

detrital $^{176}\text{Hf}/^{177}\text{Hf}$ in Fig 7-2. The Bering Sea is a marginal sea surrounded by continents or islands and is characterized by high productivity, responsible for large deposition of both lithogenic and biogenic particulate materials (Horikawa *et al.*, 2010; Takahashi *et al.*, 2010) and for efficient scavenging of beryllium from the water column. The rapid scavenging at the high-accumulation site promotes lateral transport of beryllium to this site (Anderson *et al.*, 1990). This results in ^{10}Be deposition much greater than the atmospheric input, supported by a study using sediment traps at the sites of KH-86-3 in Fig. 7-5 (Kusakabe *et al.*, 1990).

7.3.2. Comparison with the present seawater beryllium

Few beryllium isotope data for the present deep seawater were previously reported from the North Pacific, Arctic Ocean and Bering Sea. The deep seawater $^{10}\text{Be}/^9\text{Be}$ ratios in the North Pacific were derived from the analyses of ferromanganese crust (von Blanckenburg *et al.*, 1996), which were $9.3 - 10 \times 10^{-8}$ and higher than the result in this study ($3.0 - 8.3 \times 10^{-8}$). The Arctic Ocean had relatively lower $^{10}\text{Be}/^9\text{Be}$ ratios of $5 - 7 \times 10^{-8}$ at depths of 3700 and 3900 m (Frank *et al.*, 2009). Xu (1994) presented the vertical profiles of the beryllium concentrations and isotopic ratios at three sites in the North Pacific including one site in the Bering Sea near Site U1341B (KH-86-3 C) (Fig. 7-5). In these profiles, the $^{10}\text{Be}/^9\text{Be}$ ratios of the deep seawater were shown to be spatially homogeneous at a value of 10×10^{-8} and higher than the results in this study.

The $^{10}\text{Be}/^9\text{Be}$ ratios lower than the current deep seawater ratio would

indicate either lower ^{10}Be or higher ^9Be concentration in the deep seawater during 32 – 40 ka. The Authigenic $^{10}\text{Be}/^9\text{Be}$ stack reconstructed at Portuguese margin (Carcaillet *et al.*, 2004) and the global $^{10}\text{Be}/^{230}\text{Th}$ stack (Frank *et al.*, 1997) show that atmospheric ^{10}Be production would not been reduced during the period. Then, the lower $^{10}\text{Be}/^9\text{Be}$ ratio may be related to relative enhancement of the ^9Be influx. It is unclear whether the ^9Be influx was higher during that period than at present, but the coupling found between authigenic ^9Be and detrital $^{176}\text{Hf}/^{177}\text{Hf}$ at 33, 37 and 38 ka may indicate that the ^9Be concentration in the deep seawater can be readily modified by the riverine flux from the surrounding continents and islands. This would be due to the rapid scavenging of beryllium that shorten the residence time of beryllium in the Bering Sea

7.3.3. $^{10}\text{Be}/^9\text{Be}$ vs. paleo-geomagnetism

Whichever the cause of the lower $^{10}\text{Be}/^9\text{Be}$ ratio than the present ratio is, it is obvious that the peak at ~32 ka is driven by raised ^{10}Be concentration in seawater (Fig. 7-2a – c). A feature related to the paleo-geomagnetic change is likely more pronounced between 40 – 41 ka than at ~32 ka (Fig. 7-2e – i), which might be the signal of the Laschamp excursion (40.7 ± 1.0 ky; Singer *et al.*, 2009). The peak at ~32 ka would be correlated with the Mono Lake excursion whose existence and accurate age are still controversial. A refined data set for the intensity and inclination of natural remanent magnetism (Fig. 7-6; Steve Lund, personal communication) shows a geomagnetic feature at 4.6 m comparable to that of the Laschamp excursion at

6.8 m. If it indicates the Mono Lake excursion, the increased $^{10}\text{Be}/^9\text{Be}$ ratio would be attributed to the enhanced production of cosmogenic ^{10}Be in the atmosphere as a consequence of more influx of cosmic ray. It is expected that the relationship between paleo-geomagnetic excursion and $^{10}\text{Be}/^9\text{Be}$ ratio could be clearly elucidated by expanding the $^{10}\text{Be}/^9\text{Be}$ profile in both directions to younger (Mono Lake excursion) and older (Laschamp excursion).

7.4. Conclusion

Authigenic $^{10}\text{Be}/^9\text{Be}$ and detrital $^{176}\text{Hf}/^{177}\text{Hf}$ ratios were determined from marine sediments on the Bowers Ridge in the Bering Sea spanning 32 – 40 ka. During the period, intense scavenging of beryllium from the water column was driven by lithogenic and biological particulates, which caused the coupling between authigenic ^9Be and detrital $^{176}\text{Hf}/^{177}\text{Hf}$ ratios. $^{10}\text{Be}/^9\text{Be}$ ratio in deep seawater was about half of the current value. This can be explained by increased riverine influx of ^9Be during that period. The peak of $^{10}\text{Be}/^9\text{Be}$ at ~32 ka might indicate the Mono Lake excursion, but additional data are required to prove their correlation.

7.5. Appendix – Hafnium contents in authigenic fraction of marine sediment in the Bering Sea

When determining the $^{176}\text{Hf}/^{177}\text{Hf}$ ratio from the detrital fraction of

marine sediment, authigenic hafnium can be recovered as a byproduct, whose isotope ratio can reflect the seawater composition at the time of deposition and be useful for investigating continental weathering intensity in the past (Albarède *et al.*, 1998; Van de Flierdt *et al.*, 2007; Bayon *et al.*, 2009). However, low hafnium contents in authigenic fraction can potentially matter. It is then necessary to begin with quantifying the amount of the authigenic hafnium in samples. For the extraction of authigenic fraction, the mixed solution of acetic acid and hydroxylamine hydrochloride (HH solution) has been widely used (Bayon *et al.*, 2009). However, it is observed that leached Hf is readily re-adsorbed onto particle when using HH solution, and HNO₃ is proposed as an alternative leaching agent (Bayon *et al.*, 2009). Nevertheless, the use of HH solution has advantage that the leaching step can be contemporarily applied to the extraction of other proxies, i.e., neodymium for which HH solution has been commonly used.

The two leaching solutions were tested with five “squeeze-cake” samples, residual sediments after shipboard pore water extraction. 1 g of finely ground sample was contained in 15 mL centrifuge tube (polyethylene, Falcon) and 10 mL of each leaching solution was added and shaken for three hours at room temperature. After centrifuging, the supernatant leachates were analyzed for various elements including Hf and rare earth elements using quadrupole inductively-coupled plasma mass spectrometry (Q-ICP-MS) at the National Center for Inter-University Research Facilities (NCIRF) in the Seoul National University campus (Table 7-2). The amount of recovered Hf from one gram of bulk samples was <10 ng with 0.2 M HNO₃. It was lowered with

HH solution, accounting for 64 – 76% of HNO₃ solution. However, it seemed that Hf concentration was even overestimated due to instrumental “memory effect” and 1-3 g of Hf could be commonly extracted from a gram of dried bulk sample by 0.2 M HNO₃ throughout further experiments.

To meet analytical requirement for the analysis of ¹⁷⁶Hf/¹⁷⁷Hf (>~50 ng), it was required to maximize the extraction of Hf. An experiment was designed as follows: 10 and 20 mL 0.2 M HNO₃ solution were added to 2 g of sediment. After the first extraction, additional leaching was carried out in the same condition with the first extraction (Table 7-3). By doubling the leaching solution volume, 2 – 4 ng of hafnium could be additionally acquired. Also, the second extraction offered ~3 ng Hf regardless of the volume of the leaching solution. Consequently, the maximum amount of authigenic hafnium that can be extracted from 2 g of Bering Sea sediment was approximately 20 ng (10 ng g⁻¹), insufficient for a precise analysis.

7.6. References

- Albarède, F., Simonetti, A., Vervoort, J.D., Blichert-Toft, J., Abouchami, W., 1998. A Hf-Nd isotopic correlation in ferromanganese nodules. *Geophysical Research Letters* 25(20), 3895-3898.
- Anderson, R.F., Lao, Y., Broecker, W.S., Trumbore, S.E., Hofmann, H.J., Wolfli, W., 1990. Boundary scavenging in the Pacific Ocean: a comparison of ¹⁰Be and ²³¹Pa. *Earth and Planetary Science Letters*

96(3–4), 287-304.

Bayon, G., Barrat, J.A., Etoubleau, J., Benoit, M., Bollinger, C., Révillon, S., 2009a. Determination of rare earth elements, Sc, Y, Zr, Ba, Hf and Th in geological samples by ICP-MS after Tm addition and alkaline fusion. *Geostandards and Geoanalytical Research* 33(1), 51-62.

Bayon, G., Burton, K., Soulet, G., Vigier, N., Dennielou, B., Etoubleau, J., Ponzevera, E., German, C., Nesbitt, R., 2009b. Hf and Nd isotopes in marine sediments: Constraints on global silicate weathering. *Earth and Planetary Science Letters* 277(3-4), 318-326.

Bourles, D., Raisbeck, G. M., and Yiou, F., 1989. ^{10}Be and ^9Be in marine sediments and their potential for dating. *Geochim. Cosmochim. Acta* 53, 443-452.

Carcaillet, J., Bourlès, D.L., Thouveny, N., Arnold, M., 2004. A high resolution authigenic $^{10}\text{Be}/^9\text{Be}$ record of geomagnetic moment variations over the last 300 ka from sedimentary cores of the Portuguese margin. *Earth and Planetary Science Letters* 219(3–4), 397-412.

Chu, N., Taylor, R., Chavagnac, V., Nesbitt, R., Boella, R., Milton, J., German, C., Bayon, G., Burton, K., 2002. Hf isotope ratio analysis using multi-collector inductively coupled plasma mass spectrometry: an evaluation of isobaric interference corrections. *Journal of Analytical Atomic Spectrometry* 17(12), 1567-1574.

Expedition 323 Scientists, 2011. Site U1341. In: Takahashi, K., Ravelo, A. C., Alvarez Zarikian, C. A., and the Expedition 323 Scientists Eds.) *Proc.*

IODP, 323. Integrated Ocean Drilling Program Management International, Inc., Tokyo.

Frank, M., Schwarz, B., Baumann, S., Kubik, P.W., Suter, M., Mangini, A., 1997. A 200 kyr record of cosmogenic radionuclide production rate and geomagnetic field intensity from ^{10}Be in globally stacked deep-sea sediments. *Earth and Planetary Science Letters* 149(1–4), 121–129.

Frank, M., Porcelli, D., Andersson, P., Baskaran, M., Bjork, G., Kubik, P. W., Hattendorf, B., and Guenther, D., 2009. The dissolved Beryllium isotope composition of the Arctic Ocean. *Geochimica et Cosmochimica Acta* 73, 6114–6133.

Heikkilä and Beer, in preparation, available at

<ftp://ftp.ncdc.noaa.gov/pub/data/paleo/gcmoutput/heikkila2010>

Horikawa, K., Asahara, Y., Yamamoto, K., Okazaki, Y., 2010. Intermediate water formation in the Bering Sea during glacial periods: Evidence from neodymium isotope ratios. *Geology* 38(5), 435–438.

Kusakabe, M., Ku, T.L., Southon, J.R., Measures, C.I., 1990. Beryllium isotopes in the ocean. *Geochemical Journal* 24(4), 263–272.

Leduc, G., Thouveny, N., Bourles, D. L., Blanchet, C. L., and Carcaillet, J. T., 2006. Authigenic $^{10}\text{Be}/^9\text{Be}$ signature of the Laschamp excursion: A tool for global synchronisation of paleoclimatic archives. *Earth and Planetary Science Letters* 245, 19–28.

Singer, B. S., Guillou, H., Jicha, B. R., Laj, C., Kissel, C., Beard, B. L., and Johnson, C. M., 2009. $^{40}\text{Ar}/^{39}\text{Ar}$, K-Ar and ^{230}Th - ^{238}U dating of the

- Laschamp excursion: A radioisotopic tie-point for ice core and climate chronologies. *Earth and Planetary Science Letters* 286, 80-88.
- Takahashi, K., 2005. The Bering Sea and paleoceanography. *Deep Sea Research Part II: Topical Studies in Oceanography* 52(16–18), 2080-2091.
- Takahashi, K., Ravelo, A., Zirikian, C.A.A., Expedition 323 Scientists, 2011. Bering Sea Paleoceanography. *Proc. Integr. Ocean Drill. Program* 323.
- Van de Flierdt, T., Goldstein, S.L., Hemming, S.R., Roy, M., Frank, M., Halliday, A.N., 2007. Global neodymium–hafnium isotope systematics—revisited. *Earth and Planetary Science Letters* 259(3), 432-441.
- Von Blanckenburg, F., Belshaw, N. S., and O'Nions, R. K., 1996. Separation of ^9Be and cosmogenic ^{10}Be from environmental materials and SIMS isotope dilution analysis. *Chemical Geology* 129, 93-99.
- Xu, X., 1994. Geochemical Studies of Beryllium Isotopes in Marine and Continental Natural Water Systems. Ph.D. thesis, University of Southern California, Los Angeles, 315 pp.

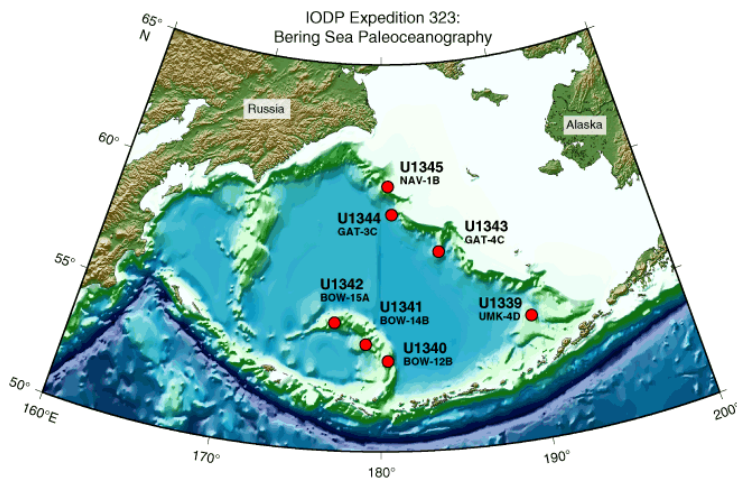


Figure 7-1. The sampling location Site U1341 with other coring sites during IODP expedition 323.

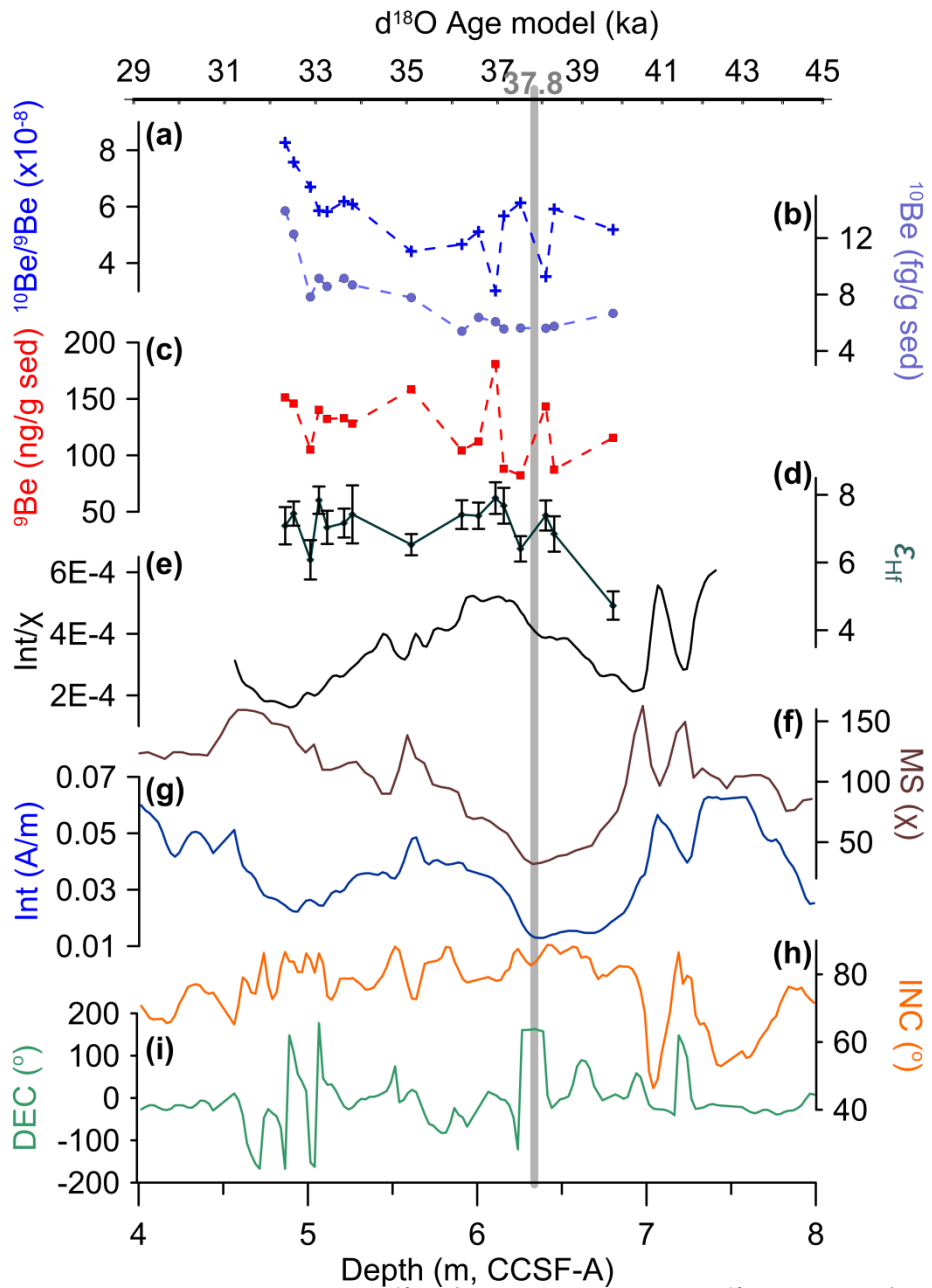


Figure 7-2. The profiles of (a) ¹⁰Be/⁹Be ratio (molar), (b) ¹⁰Be and (c) ⁹Be concentrations, (d) ε_{Hf} with ± 2SE, (e) NRM_{int}/χ as a paleointensity proxy, (f) magnetic susceptibility (χ), (g) intensity of natural remanent magnetism (NRM_{int}), (h) inclination of natural remanent magnetism, and (i) declination of natural remnant magnetism.

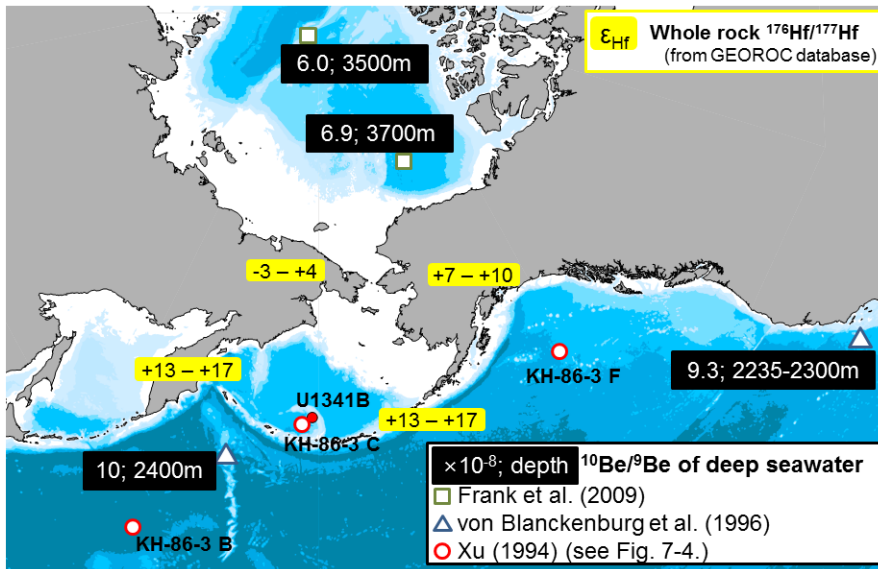


Figure 7-3. Compiled $^{10}\text{Be}/^9\text{Be}$ ratio of deep seawater in the North Pacific, Bering Sea and Arctic Ocean and whole rock $^{176}\text{Hf}/^{177}\text{Hf}$ ratio from GEOROC database (<http://georoc.mpch-mainz.gwdg.de/georoc/>). See Fig. 7-5 for the data from Xu (1994).

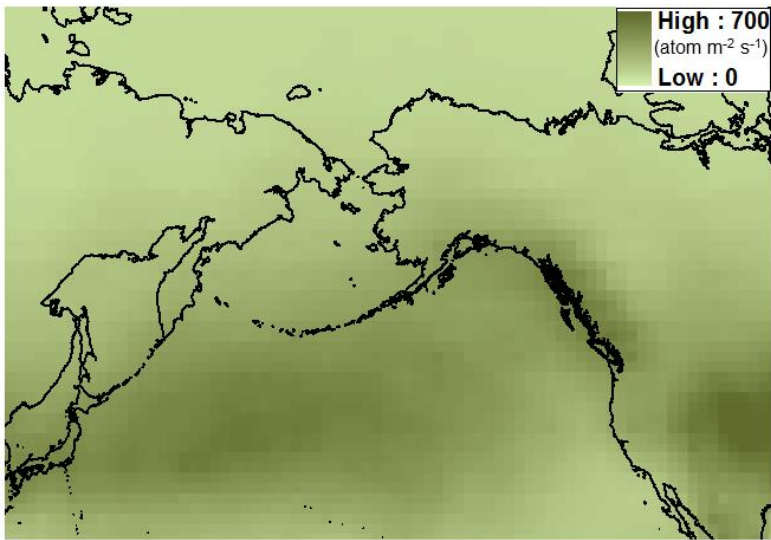


Figure 7-4. Simulated atmospheric deposition flux of ^{10}Be during 1998-2003 (Heikkilä and Beer, in preparation, drawn from the data available at <ftp://ftp.ncdc.noaa.gov/pub/data/paleo/gcmoutput/heikkila2010>)

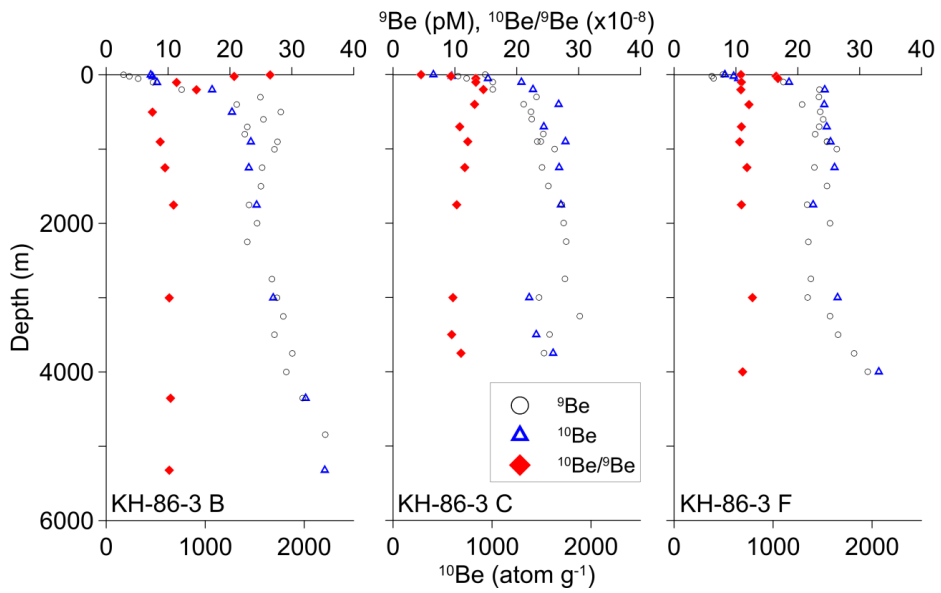


Figure 7-5. The vertical profiles of ${}^9\text{Be}$ and ${}^{10}\text{Be}$ concentrations and their ratios at three sites in the North Pacific including one site (KH-86-3 C) in the Bering Sea. The locations of the sites are shown in Fig. 7-3. Redrawn from Xu (1994).

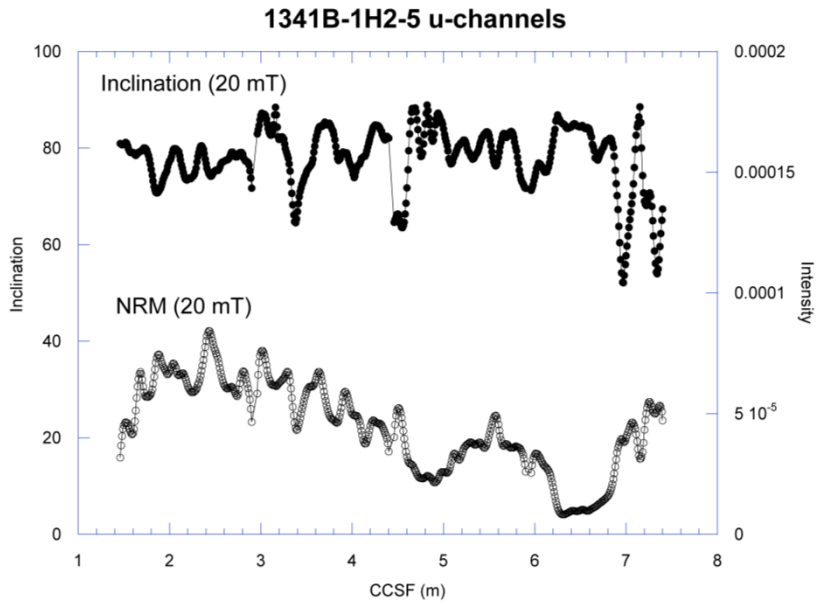


Figure 7-6. New u-channel data for the intensity of natural remanent magnetism (NRM 20mT) and inclination of NRM. Provided by Steven Lund (personal communication).

Table 7-1. The column procedure for Hf separation.

Step	Acid	Volume (ml)
Anion Exchange Column: AG1-x8 200-400 mesh (10ml Bio-Rad Poly-Prep column, 0.8 ml resin)		
Clean	6M HCl-1M HF	10
Condition	4M HF	5
Load sample	Sample in 4M HF	2~3
Elute matrix	4M HF	10
Collect Hf	6M HCl-1M HF	8
Ln Column: Eichrom Ln 50-100 mesh (15ml Savillex microcolumn, ID = 4 mm, 0.7 ml resin)		
Clean	6M HCl	6
Condition	2.2M HCl	6
Load sample	2.2M HCl-1% (v/v) H ₂ O ₂	0.1
Elute matrix (Ti)	2.2M HCl-1% (v/v) H ₂ O ₂	0.2
Elute matrix (Ti)	2.2M HCl-1% (v/v) H ₂ O ₂	3.7
Elute matrix (HREE)	6M HCl	12
Collect Hf	1M HF	8
Clean [reuse resin]	6M HCl-1M HF	6

Table 7-2. The contents (ng per g of bulk sediment) of Hf and various elements in authigenic fraction of Site U1345A core sediments, recovered by 0.2 M HNO₃ and mixed solution of acetic acid and hydroxylamine hydrochloride (HH).

U1345A (m, CSF-A) (ka, age)	1H1 (0 – 1.5 m) (~3 ka)			3H6 (21.4 – 22.9 m) (~80 ka)			6H2 (43.90 – 45.38 m) (~150 ka)			11H2 (90.8 – 92.3 m) (~300 ka)			15H2 (128.26 – 129.76 m) (~450 ka)		
	HNO ₃	HH	HH/ HNO ₃	HNO ₃	HH	HH/ HNO ₃	HNO ₃	HH	HH/ HNO ₃	HNO ₃	HH	HH/ HNO ₃	HNO ₃	HH	HH/ HNO ₃
Th	125	59	0.47	187	100	0.53	376	180	0.48	363	204	0.56	525	253	0.48
Sc	238	203	0.85	265	220	0.83	564	378	0.67	386	351	0.91	704	449	0.64
Y	3797	3289	0.87	4208	3334	0.79	5250	3681	0.70	4103	3210	0.78	5648	3592	0.64
La	2703	2435	0.90	2972	2561	0.86	3814	2910	0.76	3011	2761	0.92	3699	2904	0.78
Ce	6135	5660	0.92	7085	6219	0.88	8823	6895	0.78	7191	6732	0.94	8601	6932	0.81
Pr	799	745	0.93	936	820	0.88	1162	907	0.78	938	868	0.93	1088	901	0.83
Nd	3378	3130	0.93	4000	3505	0.88	4983	3845	0.77	4000	3669	0.92	4563	3776	0.83
Sm	1077	961	0.89	1245	1043	0.84	1538	1169	0.76	1239	1132	0.91	1365	1133	0.83
Eu	241	217	0.90	275	225	0.82	353	255	0.72	285	253	0.89	315	250	0.79
Gd	1157	958	0.83	1245	1025	0.82	1564	1160	0.74	1273	1122	0.88	1389	1122	0.81
Tb	170	144	0.84	187	152	0.81	234	171	0.73	188	163	0.86	212	165	0.78
Dy	862	711	0.83	914	730	0.80	1158	832	0.72	903	766	0.85	1072	809	0.75
Ho	158	128	0.81	163	128	0.78	208	146	0.70	157	131	0.83	201	143	0.71
Er	405	332	0.82	413	322	0.78	528	368	0.70	387	318	0.82	537	368	0.69
Tm	53	44	0.83	53	41	0.77	67	47	0.70	49	40	0.82	74	49	0.66
Yb	315	266	0.84	311	243	0.78	400	278	0.69	284	232	0.82	463	304	0.66
Lu	46	39	0.84	45	34	0.75	58	39	0.68	41	33	0.80	72	45	0.62
Hf	8.5	5.7	0.67	7.8	5.9	0.76	8.4	6.2	0.73	7.9	6.1	0.77	9.7	6.2	0.64
Ti	30000	21818	0.73	14717	11144	0.76	20213	14140	0.70	11441	9328	0.82	20539	10100	0.49
Zr	144	54	0.37	109	54	0.49	83	39	0.47	118	65	0.55	214	75	0.35
Ta	3	2	0.71	2	2	0.77	3	2	0.70	2	2	0.84	3	2	0.67
W	7	4	0.61	8	5	0.63	11	6	0.54	7	5	0.71	12	8	0.69

Table 7-3. The improvement of authigenic hafnium extraction from sediment (2 g) by doubling the volume of the leachnig solution (0.2 M HNO₃) and by additional leaching step.

Sample	0.2 M HNO ₃	Recovered Hf (ng) from 2 g sediment	
		1st leaching	2nd leaching
U1343B 2H6 (14.5 – 16.0 m, CSF-A) (~50 ka)	10mL	7.2	2.8
	20mL	10.8	2.9
U1345B 3H6 (25.2 – 26.7 m, CSF-A) (~ 100 ka)	10mL	7.3	3.0
	20mL	9.4	3.4

국문 초록

지구는 그 변화를 스스로 기록하는데, 그 방법 중 하나로 열역학적 상 전이를 통하여 상대적으로 안정한 물질을 생성한다. 이 물질들은 생성 당시의 환경을 반영하고 있어 당시의 지구 환경을 연구하는 데 중요한 자료가 된다. 본 학위 논문은 주로 대기와 해양에서 응결 및 침전을 통하여 기록된 지구의 변화를 다루고 있다.

제 2 장과 3 장에서는 빗물의 성분을 연구하는 과정에서 국지적인 영향을 어떻게 고려하여야 할 지를 다룬다. 연구는 국내에서 배경대기를 연구하기 위하여 세워진 백령도 대기종합측정소(2 장), 제주도 고산관측소(3 장) 두 지점에서 이루어졌다. 백령도 대기종합측정소에서는 강한 풍속 및 주변 지형·지물의 영향으로 수 십 미터의 국지적인 범위 내에서 위치에 따라 빗물 시료 채집량이 서로 다르게 나타났고, 그 결과 각각의 빗물 성분 역시 상이하였다. 이와 같은 국지적 영향을 보다 자세하게 연구하기 위하여 제주도 고산관측소에서 지난 14 년간 관찰된 강수 화학 자료를 획득하여 다양한 통계법을 적용하였다. 그 결과, 풍향·풍속에 따라 국지적으로 발생한 에어러솔이 빗물 성분에 상당한 영향을 주는 것으로 나타났다. 본 연구는 배경 대기 관측의 일환으로 빗물의 조성을 연구할 때 시료 채집 장소를

적절하게 선정하고, 장기 관측을 통하여 해당 지점에서의 국지적인 영향을 산정하는 것이 필요하다는 것을 보여준다.

제 4, 5, 6 장에서는 남극 눈에 포함된 수은 농도와 그 의미를 연구하였다. 4 장에서는 표층 눈 내 수은 농도, 5, 6 장에서는 깊이에 따른 수은 농도 변화를 통하여 남극 고원 지대에서의 수은 거동이 눈의 수은 농도에 어떤 영향을 주는지 연구하였다. 여름철에 발생하는 일련의 광화학 반응에 의하여 수은은 대기 중 안정한 Hg^0 에서 반응성이 큰 Hg^{2+} 로 산화된 후 지표로 침전되면서 표층 눈 내 수은 농도를 높이는 것으로 나타났다. 그러나 깊이에 따른 수은 농도 변화를 보면 상대적으로 낮은 농도 범위를 갖는데, 이는 침전된 수은이 또 다른 광화학 반응에 의하여 Hg^0 으로 환원되면서 대기 중으로 다시 방출되기 때문이다. 양 방향의 수은 교환의 결과로 눈 내에 남겨져 하부에 묻힌 수은은 전지구적인 수은 순환으로부터 반영구적으로 격리되는데, 그 양은 고원 지대로 수송되는 해염의 양이 가장 크게 영향을 주는 것으로 사료된다.

제 7 장에서는 베링해의 Bowers Ridge 에서 국제공동해양시추사업(Integrated Ocean Drilling Program)을 통하여 획득된 해저 퇴적물 중 32 - 40 ka 기간에 해당하는 퇴적물의 자생성분 내 $^{10}Be/^{9}Be$ 및 쇄설성분 내 $^{176}Hf/^{177}Hf$ 비를 측정하였다. 자생성분은 생성 당시의 해수 성분을 반영하고 쇄설성분은 입자의 기원에 대한 정보를 가지고 있다. $^{10}Be/^{9}Be$ 은

현재 해수의 절반 수준의 값을 가졌는데, 생물 활동 및 강을 통한 ^9Be 와 쇄설물의 유입이 증가하였기 때문으로 보인다. ~32 ka 에서 관찰되는 상대적으로 높은 $^{10}\text{Be}/^9\text{Be}$ 값은 지구 자기장 감소에 따른 대기 중 ^{10}Be 의 생성이 증가하였기 때문으로 추측된다.